Irradiation-Induced Solvated Electron Production for the Degradation of Perfluorooctanoic Acid in an Aqueous System

An Application of the Mixed Radiation Field Produced by the RMC SLOWPOKE-2 Nuclear Reactor

La production d'électrons solvatés induite par irradiation pour la dégradation de l'acide perfluorooctanoïque dans un système aqueux

Une application du champ de rayonnement mixte produit par le réacteur nucléaire SLOWPOKE-2 au CMR

A Thesis Submitted to the Division of Graduate Studies
of the Royal Military College of Canada
by

Tristan Marcellin Gauthier, rmc, B.Eng,
Captain

In Partial Fulfillment of the Requirements for the Degree of
Master of Applied Science in Chemical Engineering

March 2026

Acknowledgments

I sincerely thank my thesis advisors, Dr. Emily Corcoran, Dr. Lindsay Grandy, and Dr. Kela Weber for their expert advice, persistent guidance, and tailored support throughout my graduate studies.

I would like to express my appreciation to Dr. Pavel Samuleev, Mr. Bob Whitehead, and Dr. Adrian Pang for their assistance in sample irradiation, surveying, and analysis at every junction of this thesis. Your professionalism, flexibility, and generous efforts helped make this thesis possible. Your positivity and joy helped lift my spirits each day and enjoy the process that is a thesis.

From the research group, I would like to thank Dr. Andrés Lara-Contreras, Mr. Danny Huston, Ms. Heather McCallum, Lt(N) Ivan Skachkov, LCdr Donald Kannegiesser, Ms. Kiana Fong, Captain Alexander Ferch and LCdr Kevin Reyes. The mutual support and discussions in the bullpen were always appreciated.

Abstract

Per- and polyfluoroalkyl substances (PFAS) are synthetic chemicals of uniquely persistent and resistant properties. While PFAS have many industrial applications, they have seeped into soil and water bodies across Canada, prompting national guidelines regulating allowable concentrations in the environment. Effective PFAS remediation technologies are required to capture and destroy these molecules. Recent studies have shown reduction reactions to be effective in destroying certain PFAS. Previous studies have found that solvated electrons (e^-_{solv}) are the key reactive species for initiating PFAS degradation reactions. The mixed radiation field generated by the RMC SLOWPOKE-2 nuclear reactor, a source of e^-_{solv} in solution, was employed to investigate the degradation of perfluorooctanoic acid (PFOA), a widely encountered PFAS compound.

Monte Carlo N Particle (MCNP) nuclear transport modelling software was used to predict neutron, photon, and electron dose rates in the inner, outer and pool irradiation sites of the RMC SLOWPOKE-2 nuclear reactor. The radiation fields present in each site are unique in composition (neutron to photon dose ratio) and dose rate ($MeV \cdot s^{-1}$). These simulated dose rates were combined with *g*-values from literature (for both water and methanol solutions) to calculate the e^-_{solv} production rates in each irradiation site.

An experimental method of quantifying the e^-_{solv} yields within the different irradiation sites was investigated. 2,2-Diphenyl-1-picrylhydrazyl (DPPH·) was selected because it is a e^-_{solv} scavenger that has been applied towards similar goals in other reducing systems. The aim was to determine the viability of DPPH· in the SLOWPOKE-2 radiation fields before applying the scavenger to benchmarking experiments. Results from ultraviolet and visible light spectroscopy (UV-Vis) and ultra-high performance liquid chromatography-quadrupole mass spectrometer (UHPLC-MS/MS) found that, even in short periods of SLOWPOKE-2 irradiation, DPPH· degrades to picric acid. Thus, DPPH· was deemed nonviable to quantify e^-_{solv} concentrations for the RMC SLOWPOKE-2 irradiation experiments when operating at nominal half power (10 kW_t).

PFOA samples were irradiated to assess its degradation relative to the concentration of e^-_{solv} in the samples. Removing dissolved oxygen (DO) from samples (< 0.4 % DO) resulted in 40 ± 10 % more PFOA degradation than samples with 100 % DO, as DO scavenges e^-_{solv} . Experiments in the different irradiation sites (*i.e.,* the inner, outer, and pool) reduced PFOA concentrations by approximately 15 % despite the differences in radiation field composition and rates. These results point to PFOA degradation depending predominantly on e^-_{solv} concentration rather than the radiation dose rate, type of radiation, and/or duration of irradiation. However, further irradiation/ e^-_{solv} production (within operational limits of reactor usage) found a degradation plateau. UHPLC-MS/MS analysis determined that PFOA degraded, in part, to shorter carbon-chain PFAS species, which accounted for the plateau (as e^-_{solv} are known to preferentially attack these shorter carbon-chain PFAS species compared to PFOA when in mixed solutions).

The results of PFOA irradiation provide valuable insights into several aspects of remediation, namely: i) substantiating the degradation mechanism, ii) demonstrating that degradation rates are primarily governed by e^-_{solv} concentration rather than the electron source, and iii) confirming that reducing DO content in samples enhances degradation during irradiation at the RMC SLOWPOKE-2 nuclear reactor.

Résumé

Les substances per- et polyfluoroalkylées (PFAS) sont des produits chimiques synthétiques dotés de propriétés de persistance et de résistance exceptionnelles. Bien que les PFAS aient de nombreuses applications industrielles, elles se sont infiltrées dans les sols et les masses d'eau à travers le Canada, ce qui a incité le gouvernement à établir des directives nationales sur les concentrations acceptables dans l'environnement. Des technologies efficaces de remédiation des PFAS sont nécessaires pour capturer et détruire ces molécules. Des études récentes démontrent l'efficacité des réactions de réduction pour détruire certains PFAS. Des travaux antérieurs ont montré que les électrons solvatés (e^-_{solv}) constituent les espèces réactives clés pour déclencher les réactions de dégradation des PFAS. Dans cette thèse, le champ de rayonnement mixte généré par le réacteur nucléaire SLOWPOKE-2, responsable de la production d'e^-_{solv} en solution, a été utilisé pour étudier la dégradation de l'acide perfluorooctanoïque (PFOA), un composé PFAS très répandu.

Le logiciel de modélisation du transport nucléaire Monte Carlo N Particle (MCNP) a été utilisé pour prédire les débits de dose de neutrons, de photons et d'électrons dans les sites d'irradiation interne, externe et dans le bassin du réacteur nucléaire SLOWPOKE-2 au CMR. Les champs de rayonnement présents dans chaque site sont uniques en termes de composition (rapport dose de neutrons/dose de photons) et de taux de dose ($MeV \cdot s^{-1}$). Ces taux de dose simulés ont été combinés avec les valeurs g publiées dans la littérature (pour les solutions d'eau et de méthanol) afin de calculer les rendements de production d'e^-_{solv} dans chaque site d'irradiation.

Cette thèse a également tenté de quantifier expérimentalement les rendements en e^-_{solv} au sein des différents sites d'irradiation. Le 2,2-diphényl-1-picrylhydrazyle (DPPH·) a été sélectionné car il s'agit d'un piégeur d'e^-_{solv} utilisé auparavant pour la quantification des électrons solvatés dans d'autres systèmes en conditions réductrices. Cette thèse visait à déterminer la viabilité du DPPH· dans les champs de rayonnement de SLOWPOKE 2 avant d'appliquer le piégeur à des expériences de référence. Les résultats de la spectroscopie dans l'ultraviolet et le visible (UV-Vis) et de la chromatographie liquide ultra-haute performance couplée à un spectromètre de masse quadripolaire (UHPLC-MS/MS) ont montré que, même après des périodes courtes d'irradiation par SLOWPOKE 2, le DPPH· se dégrade en acide picrique. Le DPPH· a donc été jugé inapproprié pour quantifier les concentrations d'e^-_{solv} dans les expériences d'irradiation du réacteur SLOWPOKE-2 au CMR lorsqu'il fonctionne à la moitié de sa puissance nominale (10 kWt).

Parallèlement aux irradiations du DPPH·, le PFOA a également été irradié afin d'évaluer sa dégradation en fonction de la concentration en e^-_{solv} dans les échantillons. L'élimination de l'oxygène dissous (OD) des échantillons (< 0,4 % d'OD) a entraîné une dégradation du PFOA supérieure de 40 ± 10 % à celle observée dans les échantillons contenant 100 % d'OD, car l'OD piège les e^-_{solv}. Les expériences menées sur chaque site d'irradiation (c'est-à-dire l'intérieur, l'extérieur et le bassin) ont permis de réduire les concentrations de PFOA d'environ 15 %, malgré les différences de composition et de débits du champ de rayonnement. Ces résultats indiquent que la dégradation du PFOA dépend principalement de la concentration en e^-_{solv} plutôt que du taux de dose de rayonnement, du type de rayonnement et/ou de la durée de l'irradiation. Cependant, une irradiation supplémentaire et une production supérieure d'e^-_{solv} (dans les limites opérationnelles d'utilisation du réacteur) ont révélé un plateau de dégradation. L'analyse UHPLC-MS/MS a déterminé que le PFOA se dégradait, en partie, en espèces de PFAS à chaîne carbonée plus courte, ce qui expliquait ce plateau (car on sait que les e^-_{solv} attaquent préférentiellement ces espèces de PFAS à chaîne carbonée plus courte par rapport au PFOA lorsqu'ils se trouvent dans des solutions mixtes).

Les résultats de l'irradiation au PFOA apportent des informations précieuses sur plusieurs aspects de la remédiation, notamment : i) la justification du mécanisme de dégradation, ii) la démonstration que les taux

de dégradation dépendent principalement de la concentration d'e^-_{solv} plutôt que de la source d'électrons, et iii) la confirmation que la réduction d'oxygène dissous dans les échantillons favorise la dégradation lors de l'irradiation au réacteur nucléaire SLOWPOKE-2 au CMR.

Table of Contents

List of Tables

List of Figures

List of Symbols

C6	Perfluoroheptanoic acid
C7	Perfluorohexanoic acid
C8	Perfluorooctanoic acid
C_o	Initial concentration
C_f	Final measured concentration
C_f/C_o	Concentration ratio
C-C	Carbon to Carbon bond
C-F	Carbon to Fluorine bond
^{60}Co	Cobalt-60
e^-	Electron
e^-_{solv}	Solvated electron
k_{eff}	Effective criticality
kW_t	Thermal reactor power in kilowatts
T_c	Control sample measured *x* time after preparation
T_{irr}	Time irradiated
^{235}U	Uranium-235

List of Acronyms and Abbreviations

AECL	Atomic Energy Canada Limited
CANDU	Canada Deuterium Uranium
CMR	Collège militaire royal du Canada
CNL	Canadian Nuclear Laboratories
DO	Dissolved Oxygen content
DPPH:H	1,1-Diphenyl-2-picrylhydrazine
DPPH·	2,2-Diphenyl-1-picrylhydrazyl
ESG	Environmental Sciences Group
LANL	Los Alamos National Laboratories
LEU	Low Enriched Uranium
MCNP	Monte Carlo N-Particle Code
MS/MS	Quadrupole Mass Spectrometer
NAA	Neutron Activation Analysis
NRU	National Research Universal Reactor
PFAS	Per- and polyfluoroalkyl substance
PFCA	Perfluorocarboxylic Acid
PFHpA	Perfluoroheptanoic acid
PFHxA	Perfluorohexanoic acid
PFOA	Perfluorooctanoic acid
PFOS	Perfluorooctanesulfonic acid
RMC	Royal Military College of Canada
SLOWPOKE-2	Safe Low Powered C(K)ritical Experiment 2
TLD	Thermoluminescent Dosimeter
UHP	Ultra High Purity
UHPLC	Ultra-High Performance Liquid Chromatography
UHPLC-MS/MS	Ultra-High Performance Liquid Chromatography coupled to a Quadrupole Mass Spectrometer
UV	Ultraviolet
UV-Vis	Ultraviolet Visible Spectrophotometry

Chapter 1. Introduction and Goals

PFAS designate a class of synthetic chemicals used in a wide variety of industries. PFAS are resistant to chemical and temperature attacks due to their molecular structures, and this persistence has led to PFAS used as surfactants, repellants, and lubricants in various products. PFAS applications now include textiles, cosmetics, drugs and medical devices, food packaging materials, vehicles, electronics, and aqueous film-forming-foam [1–5]. Several studies have confirmed PFAS leaches into wetland environments and water sources, especially near airports and military bases, plants, and aquatic food webs [6-11]. Due to observed effects linked to PFAS found in the environment, Canada has set guidelines for suggested maximum concentrations of PFAS in both soil and water [12,13].

Many studies have concentrated on PFAS remediation, resulting in several efficient techniques for eliminating PFAS contaminants from environmental settings [14]. The subsequent phase involves appropriately disposing of these pollutants. Modern PFAS disposal research focusses primarily on reductive and oxidative systems, leveraging the radical species produced to attack and degrade PFAS molecules [15,16]. Methods researched include: Ultraviolet (UV) activated salt reactors, photocatalysis, sonochemical oxidation, electrochemical oxidation, ozonation, low temperature plasma treatment, mechanochemical degradation, phytoremediation, electron beam irradiation and nuclear irradiation [16–22]. While these methods have led to varying degrees of success, these incur varying resource and energy costs, even in small research scale operations. Optimization of any method towards large scale remediation requires further insight into the degradation mechanisms of PFAS in reduction and/or oxidation systems. Nuclear reduction systems investigate many radical species produced, and recent studies identify e^-_{solv} as a key reactive species responsible for PFAS degradation during nuclear irradiation [20–23]. In this thesis, perfluorooctanoic acid (PFOA), a common and difficult to degrade PFAS [20], is the focus of further irradiation research.

A e^-_{solv} is an electron that is dissolved into a solution, and acts as an anion within the solution [24]. These e^-_{solv} are of interest to this research due to their potent reducing capability [25] and their role in PFAS degradation found in previous literature [21–23]. Having identified e^-_{solv} as a key reactive species in PFAS degradation, recent research focusses on maximizing the production of e^-_{solv} in PFAS remediation techniques. Maximizing e^-_{solv} production led to increases in reagent and power costs [26]. Proper optimization requires greater knowledge and quantification of e^-_{solv} yields during PFAS degradation experiments.

This thesis applies the Royal Military College of Canada (RMC) Safe Low Power (K) Critical Experiment 2 (SLOWPOKE-2), a source of e^-_{solv} production, to further research PFOA degradation by e^-_{solv}. Simulation and experimental methods of e^-_{solv} quantification are investigated and applied in this thesis to compare e^-_{solv} yield to PFOA degradation during irradiation.

The RMC SLOWPOKE-2 nuclear research reactor was completed in 1985 and has been applied to research in various topics for forty years [27]. Characterization of the neutron flux and gamma dose rate have been the focus of research since 1989, with most recent research published in 2024 [20,28–33]. RMC SLOWPOKE-2 irradiation experiments are significantly more sustainable than other PFAS degradation methods as the irradiation can be conducted concurrently to other research experiments. Past studies within the RMC Nuclear Group to quantify the SLOWPOKE-2 neutron flux through simulation and experimentation have produced validated nuclear prediction models, using the Monte Carlo N Particle (MCNP) transport computer software [20,30–33]. Validated radiation simulation models are a critically

valuable research asset to sustainable research practices. For this thesis, MCNP6.3* [34] is applied to predict the RMC SLOWPOKE-2 radiation field characteristics that are used to quantify e^-_{solv} production and yields for PFAS irradiation experiments. Until now, there have been no reports in the literature of the MCNP software being used to predict e^-_{solv} production during irradiation in the RMC SLOWPOKE-2 reactor, thus, this thesis will investigate the capability to quantify e^-_{solv} and develop a theoretical yield in irradiated samples.

To confirm the accuracy of these simulated e^-_{solv} yields, this thesis carried out experiments to measure the concentration of e^-_{solv} using 2,2-Diphenyl-1-picrylhydrazyl (DPPH·). DPPH· is commonly used in e^-_{solv} quantification studies [35]. A DPPH† assay involves exposing DPPH· solutions to reducing systems. The concentration of DPPH· that reacts can be quantified through UV and visible light spectroscopy (UV-Vis). However, the radiation field is the RMC SLOWPOKE-2 irradiation sites is more intense than those from previous applications of the molecule. Thus, the molecular survival of DPPH, and the viability of applying a DPPH assay of [e^-_{solv}] to the RMC SLOWPOKE-2 irradiation sites is investigated.

Previous PFAS degradation studies involving nuclear experiments commonly apply gamma or electron radiation sources [21-23,35]. The RMC SLOWPOKE-2 is chosen to apply to PFOA irradiation research due to the unique mixed neutron and photon radiation fields present in the different irradiation sites of the reactor. The effects of neutron radiation on PFAS degradation require more study, as do the differences in radiation dose rate and neutron to photon dose ratio; all of which alter the production rates of e^-_{solv}. Experimental results from this study compare PFOA degradation to several factors affecting the amount of e^-_{solv} exposed to samples. These experiments investigate PFOA degradation reliance on rate of e^-_{solv} production versus total [e^-_{solv}] exposure.

1.1 Thesis Goals

The primary objective of this thesis is to investigate PFOA degradation during irradiation experiments in the RMC SLOWPOKE-2 research reactor. This objective is accomplished through the developments in three distinct areas of research that form individual goals:.

i. Apply MCNP6.3 software to predict the yield of e^-_{solv} in samples irradiated in the RMC SLOWPOKE-2.
ii. Investigate the viability of quantifying e^-_{solv} yields with DPPH· in the mixed field radiation environments of the RMC SLOWPOKE-2 irradiation sites.
iii. Investigate the effects of varying e^-_{solv} yields from RMC SLOWPOKE-2 irradiation on PFOA degradation.

Chapter 2 discusses literature and background concepts relevant to this thesis. Chapters 3, 4, and 5 present methods and results of research completed herein. *Chapter 3* details the MCNP6.3 model development and simulation results. *Chapter 4* investigates the viability of a DPPH assay within the RMC SLOWPOKE-2. *Chapter 5* describes PFOA experiments completed and analyzes the results.

---

* *Newest version of MCNP software, released in August 2023* [34].

† *N.B., This thesis uses the term DPPH· to refer to the molecule as a stable free radical. The term DPPH:H is used for the reduced form of the molecule. Finally, the term DPPH is used to refer to any combination of the two previous terms. This includes the DPPH assay, as the method quantifies both DPPH· and DPPH:H in solution to determine the [e^-_{solv}] that interacted with the solution.*

Chapter 2. Background

This chapter provides the theoretical background and contextual information relevant to topics applied in this thesis, broken up into different research domains.

2.1 Per and Polyfluoroalkyl Substances

Industrial use of many common PFAS molecules is prohibited by the Canadian Environmental Protections Act 1999 and there are national guidelines suggesting maximum concentrations for several PFAS in water and soil [13,37,38]. These guidelines prompt remediation research and projects aiming to remove and destroy the contaminants across the country.

The key characteristic of PFAS are their fluorinated carbon chain tails. These fluorinated carbon tails are henceforth referred to as the per/polyfluorinated tail, or simply the tail. At the head of these molecules are varying functional groups, often used to further subdivide PFAS, such as Perfluorocarboxylic acids (PFCA), which are perfluorinated tails ending in a carboxylic acid [39,40]. The perfluorinated tails produce strong hydrophobic and lipophobic properties, while imbuing the molecules with temperature and chemical resistances [39].

Perfluorooctanoic acid (PFOA) is a PFCA that has an eight-carbon chain (C8). PFOA is the target of study in this thesis due to its historically widespread use in Canada, its prevalence among Canadian waters, and previous difficulties in its destruction [13,20]. Figure 1 shows the molecular structure and the Van der Waals model of PFOA, demonstrating the intermolecular forces formed by the perfluorinated tail. The electrostatic force from the electrons orbiting the fluorine atoms cause both the chemical resistance and the helical shape of the molecule. This helicity further contributes to the durability of the molecule by minimizing the gaps between the electron clouds of each atom. Any degradation mechanism must focus on either attacking these fluorine atoms or attack the carbon chain *via* the functional group. Literature confirms that both mechanisms can occur concurrently in solution [22].

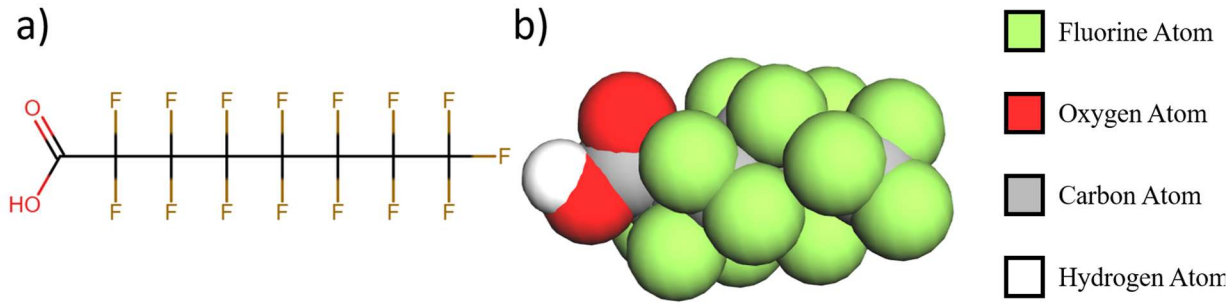

Figure 1: Perfluorooctanoic Acid (PFOA) is depicted in a) a 2D model and b) a Van der Waals model. Figure a) generated with Chemical Sketch Tool from the Research Collaboratory for Structural Bioinformatics and Marvin JS by Chemaxon[41,42]. Figure b) generated with Molview.org [43].

2.1.1 PFAS Degradation

International efforts to degrade and destroy various PFAS (including PFOA) primarily involve redox reactions [15,17,18,44]. Common methods include: planetary ball mills, UV-activated salt reactors, persulfate activation, supercritical water oxidation, photocatalysis, electrochemical oxidation, ozonation, thermal degradation, and sonochemical activation [16,17,26,44,45]. While these methods offer degrees of

PFAS degradation (chemical changes to the molecule that typically make it easier to destroy) or destruction (complete defluorination of the molecule, with no type of PFAS remaining in solution), the material and/or energy costs are significant, prompting researchers to develop more sustainable practices. Nuclear technologies have been increasingly applied to the research of PFAS remediation in the last decade [20,15,22,23]. The introduction of electron beam technology and gamma radiation sources to PFAS degradation experiments have led to substantial developments to the degradation pathways and mechanisms of several PFAS [20–23].

The redox environments produced in the studies listed above apply different methods to achieve the same goal: *produce highly reactive radical species capable of attacking PFAS molecules at the fluorine atoms and functional groups*. Key among these reactive species is the electron. In many redox environments, electrons can become temporarily dissolved into the solution, undergoing solvation to become e^-_{solv}. Solvation is the stabilization of the electron between solvent molecules [46], sometimes requiring the electron to polarize molecules within the solvent. In solution, e^-_{solv} act as anions and may initiate complex chemical reactions or undergo germinate recombination (bond with solvent cations)[24,47,48].

The potent reducing capabilities of e^-_{solv} [25] and their role in PFAS degradation found in PFAS degradation in previous literature make these radicals a special interest of this research [21–23,49]. Note that e^-_{solv} are sometimes called hydrated or aqueous electrons when dissolved in water. The experimental portion of this thesis useswater in PFOA solutions and methanol in DPPH· solutions, and thus the more generic term, e^-_{solv}, is used herein.

In aqueous or methanol solutions, the highly electronegative atoms of molecular oxygen can have significant impacts on the [e^-_{solv}] during redox reactions. Atmospheric O_2 dissolved into the solution (DO content) has a high affinity for e^-_{solv}, acting as a scavenger as seen in Equation a [49,50]. Thus, limiting DO in PFAS solutions may increase potential degradation. The saturation of the solution with atmospheric oxygen is considered to a 100% DO content (10.92 mg $O_2 \cdot L^{-1}$ H_2O at 21 °C [51]), and the complete removal of DO (0 mg $O_2 \cdot L^{-1}$ H_2O) from solution represents 0% DO content.

$$e^-_{solv} + O_2 \rightarrow O_2^- \cdot \qquad \textit{Equation a}$$

In Trojanowicz *et al.* (2018) and Trojanowicz *et al.* (2019) an electron beam and ^{60}Co radiation sources are applied to PFOA and perfluorooctanesulfonic acid (PFOS) degradation experiments to create reduction environments in irradiated solutions. These experiments achieved up to 80 % PFOA and 90 % PFOS degradation [21,23]. These results helped determine that reductive conditions, more than oxidative conditions, support PFOA and PFOS degradation.

In 2022, Patch *et al.* analyzed the PFAS degradation products formed during gamma irradiation experiments, applying a ^{60}Co source [22]. Patch *et al.* (2022) proposed degradation mechanisms for various PFAS, including PFOA, based on the degradation products found in irradiated samples. Results indicated that e^-_{solv} are key for initiating degradation. The remainder of this section will focus on the degradation of PFCAs, including PFOA.

Figure 2 depicts the pathways of PFCA degradation as published in Patch *et al.* [22], starting with an attack by e^-_{solv} on the functional group head of the molecule (intermediate species 1). Subsequent steps see further e^-_{solv} attack and fluorine ejection (intermediates 2 and 3). Next, three mechanisms continue to degrade PFCAs concurrently. Pathway A (orange) sees the molecule react with either e^-_{solv} or $H^\cdot$ to remove fluorine atoms from the fluorinated tail of the PFCA. This pathway can cycle on itself, leading to defluorination of the PFCA, and eventually full destruction.

Pathway B (green) is a carbon chain shortening mechanism, which result in a PFCA one carbon shorter than the original molecule. From intermediate 3, a hydroxyl radical reacts with the molecule, leaving intermediate 7. From species 7, three different sequences can occur concurrently during irradiation, all of which cleave the head carbon atom from the PFCA, then removing the fluorine atoms from the second carbon, then end with the carboxylation of that carbon. The presented paths between intermediates 7 and 11 in the figure are:

i. 7→8→9→10→11,
ii. 7→12→13→11; or
iii. 7→13→11.

All three pathways change species 7 into species 11 and consume e^-_{solv} and other radical/ionized species. The resulting molecule is still a PFCA, but the perfluorinated tail is now one carbon shorter than the original PFCA. These chain-shortening degradations can occur iteratively, shortening the PFCA by one carbon with each cycle. PFOA (C8) can degrade sequentially through Pathway B to perfluoroheptanoic acid (PFHpA), a seven-carbon length (C7) PFCA, then to perfluorohexanoic acid (PFHxA), a six-carbon length (C6).

Pathway C (yellow) begins with an intermediate product of Pathway B and eventually cycles into Pathway A. Pathway C degradation removes the carboxylic acid, then performs an F•/OH• swap reaction. The result is the re-carboxylation to a shorter PFCA. After this carbon-chain shortening, the molecule enters the defluorination cycle in Pathway A.

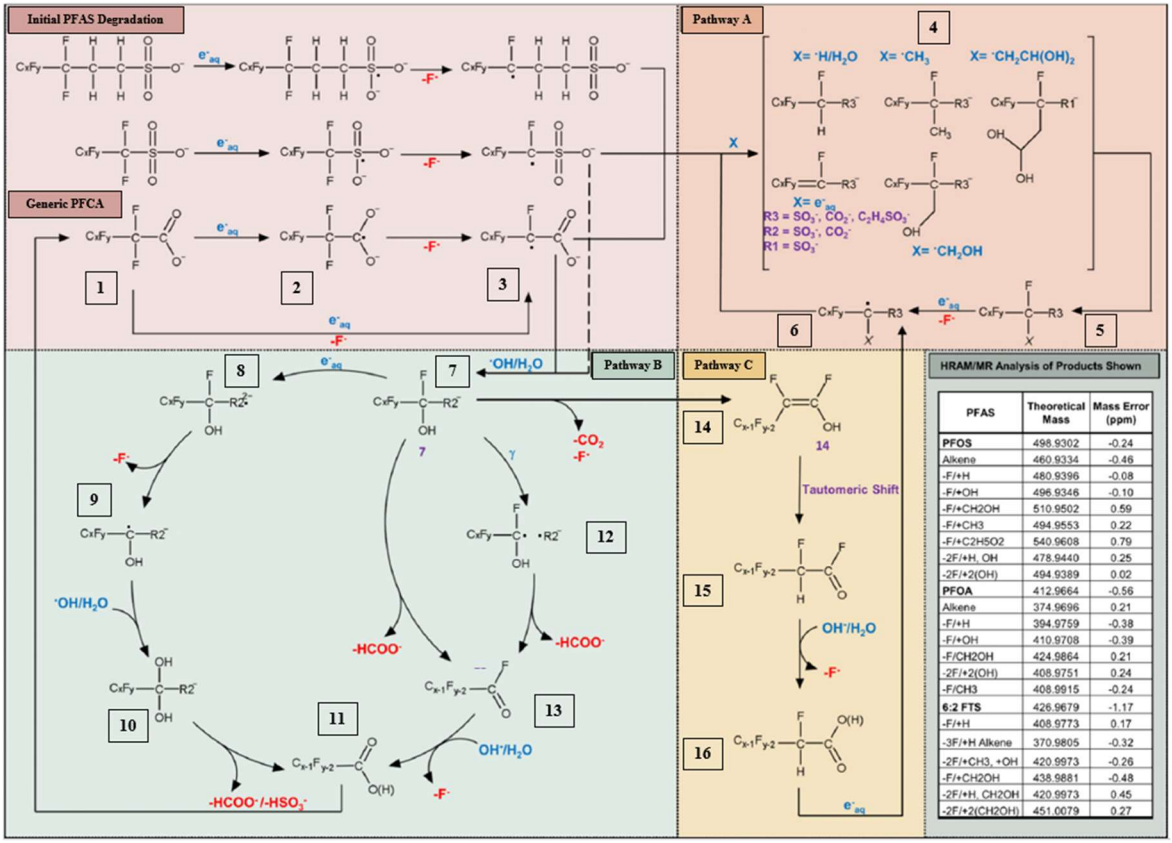

PFAS	Theoretical Mass	Mass Error (ppm)
PFOS	498.9302	-0.24
Alkene	460.9334	-0.46
-F/+H	480.9396	-0.08
-F/+OH	496.9346	-0.10
-F/+CH2OH	510.9502	0.59
-F/+CH3	494.9553	0.22
-F/+C2H5O2	540.9608	0.79
-2F/+H, OH	478.9440	0.25
-2F/+2(OH)	494.9389	0.02
PFOA	412.9664	-0.56
Alkene	374.9696	0.21
-F/+H	394.9759	-0.38
-F/+OH	410.9708	-0.39
-F/CH2OH	424.9864	0.21
-2F/+2(OH)	408.9751	0.24
-F/CH3	408.9915	-0.24
6:2 FTS	426.9679	-1.17
-F/+H	408.9773	0.17
-3F/+H Alkene	370.9805	-0.32
-2F/+CH3, +OH	420.9973	-0.26
-F/+CH2OH	438.9881	-0.48
-2F/+H, CH2OH	420.9973	0.45
-2F/+2(CH2OH)	451.0079	0.27

Figure 2: PFAS degradation mechanism proposed in Patch et al. (2022). Figure adapted from Scheme 1 in Patch et al (2022), with permission [22]. Intermediary species are labelled 1 through 16.

PFCA degradation is also possible *via* e^-_{solv} attack directly on the fluorinated carbon atoms in the tail chain, as evidenced by findings of partially defluorinated PFAS in ^{60}Co irradiated samples [22]. The attack leads to the ejection of a fluorine atom along the tail, leaving a radical carbon. In redox environments, hydrogen can bond to the radical carbon. Such an F^-/H^+ substitution leaves neighboring parts of the fluorinated chain exposed to further radical attack. PFAS F^-/H^+ substitution has been shown in simulations to extend the fluorinated tail from its initial helicity (see *Section 2.1*) to a linear frame shown in Figure 3 [52]. Now partially defluorinated and linear, both the structure and electron density of the PFCA are altered, leaving the molecule susceptible to further defluorination and full destruction should it remain in the redox environment.

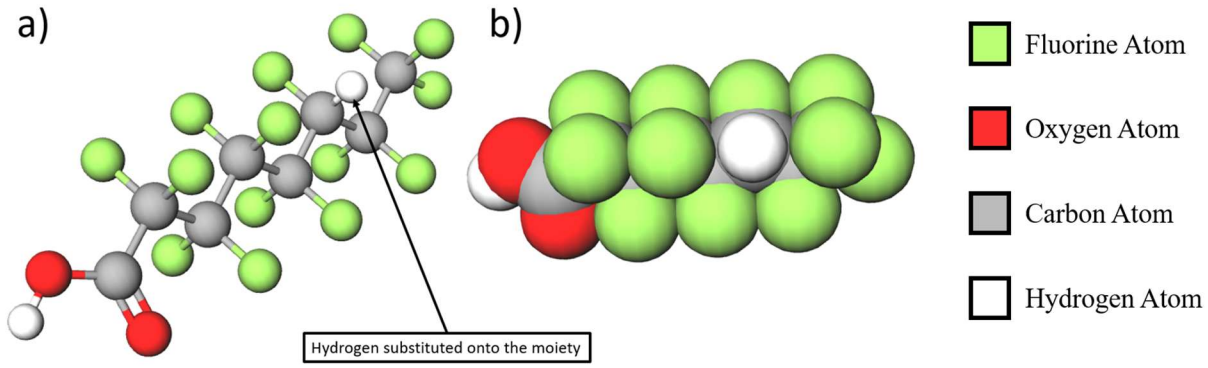

Figure 3: A PFOA molecule after a –F / +H substitution has occurred on the C6 atom in the (a) stick and ball and (b) Van der Waals models. Model a) shows the fluorinated moiety straightened out due to the addition of a hydrogen atom. Model b) demonstrates the smaller electron density of the hydrogen atom and the gaps in the electron shell surrounding the polyfluorinated tail. figure generated with Molview.org [43].

The systems that create continuous redox environments typically have high reagent costs. Fortunately, nuclear reactors produce sufficient ionizing radiation to create constant redox environments in irradiated solutions without costly reagents. In small-scale experiments such as those herein, the cost of the nuclear fuel spent on such irradiations is minimal. The ionizing radiation emitted from nuclear reactors creates redox conditions through the process of radiolysis.

2.3 Radiolysis

Radiolysis describes the ionization, excitation, and subsequent reactions of solvent molecules when energy from radiation is absorbed by a solution. The products of radiolysis reactions are radicals and/or ions, which are specific to the medium. Due to the reactive nature of these species, the concentrations are difficult to measure post-irradiation. Additionally, due to the complexities of neutron radiation and the setup of the radiation source used in this thesis, the concentrations are difficult to measure during irradiation. Thus, to quantify radiolysis products, it is common to determine the production rate, or *g*-value for the species of interest. The *g*-value of a radiolysis product quantifies the number of a species produced per 100 eV of radiation energy absorbed into the solution. This relationship is very useful for experiments where radical/ion measurement tools cannot be used during irradiation, due to either physical constraints or radioactive activation (by neutron radiation) concerns. Literature *g*-values describe the primary radiolysis yields. This requires an understanding of the nuances of radiolysis. A nuclear reactor is used to initiate radiolysis reactions in irradiated samples.

In pure water (pH 7), the radiation energy is absorbed by water molecules, which are excited and/or ionized. In the following 10 ns, these species react with others that are proximate and establish local homogeneous concentrations of radicals (including e^-_{solv}, *etc.*), referred to as the primary radiolysis yields. These production yields are only dependent on absorbed dose and are described by the *g*-values.

On longer timescales, the primary radiolysis products diffuse into the bulk solution where they can react with other species dissolved in the solution. Such reactions are dependent on the solution conditions and deviate from the *g*-values. In irradiations longer than the 10 ns, many reactions compete for the radiolysis products, some of which consume e^-_{solv}. Only the e^-_{solv} not consumed in these reactions are available to react with dissolved PFOA. In the comparatively long irradiation used in this thesis (> 1 minute *vs.* < 100 ns), any *g*-value-derived [e^-_{solv}] is an overestimation as it only accounts for production yields, not the consumption.

This thesis involves irradiation experiments in both water and methanol. Radiolysis reactions are similar in mechanism but differ in target molecules and outcomes. Therefore, the reactions, produced species, and *g*-values are discussed separately.

2.3.1 Water Radiolysis

Radiolysis includes the following reactions in pure water (pH 7) solutions [53,54] :

$$H_2O + Ionizing\ Radiation \rightarrow H_2O^+ + e^- \qquad \textit{Reaction 1}$$

$$H_2O + Ionizing\ Radiation \rightarrow H_2O^* \qquad \textit{Reaction 2}$$

$$H_2O^+ + H_2O \rightarrow H_3O^+ + \cdot OH \qquad \textit{Reaction 3}$$

The electrons produced through the reaction in Reaction 1 are highly reactive, and further ionize water molecules within short distances [54]. As electrons dissipate energy into the medium, interactions transition from ionization and excitation to the polarization (unless solvent is already polar) and reorientation interactions characteristic of e^-_{solv}. Once formed, e^-_{solv} are consumed in Reaction 4-Reaction 8 [50,53,54].

$$e^-_{solv} + H_3O^+ + H_2O \rightarrow H\cdot + 2H_2O \qquad \textit{Reaction 4}$$

$$e^-_{solv} + \cdot OH + H_2O \rightarrow OH^- + H_2O \qquad \textit{Reaction 5}$$

$$e^-_{solv} + e^-_{solv} + 2H_2O \rightarrow H_2 + 2OH^- \qquad \textit{Reaction 6}$$

$$e^-_{solv} + H\cdot + H_2O \rightarrow H_2 + OH^- \qquad \textit{Reaction 7}$$

$$e^-_{solv} + H_2O \rightarrow (H_2O^{\bullet -})^* \rightarrow H^- + OH^{\bullet} \qquad \textit{Reaction 8}$$

An Atomic Energy Canada Limited (AECL) report from 2008 [55], considers experiments in the National Research Universal (NRU) reactor. The report publishes equations Equation b Equation c for calculating the *g*-value in species per 100 eV absorbed of e^-_{solv} produced from nuclear reactor induced radiolysis, based on the temperatures (in °C) of the water in the reactor during operation. The equation used to calculate *g*-values for radiolysis in water are in Table 1.

There are different equations for e^-_{solv} produced by neutron radiation versus photon and electron radiation because of the ways in which directly and indirectly ionizing radiation impart dose into the solvent. While photon and electron radiation deposit energy into small batches of solvent spread across the solution,

forming spurs of radiolysis products, neutron radiation deposits energy through inelastic collisions homogeneously throughout the solution. These different modes of dose absorption necessitate separate *g*-values.

Table 1: Solvated electron g-value equations for nuclear reactor irradiation, by the type of radiation dose absorbed.

Radiation Type	*g*-Value Equation (molecules·100 eV^{-1})	Equation Reference
Photon and Electron Radiation	$g(e^-_{solv}) = 2.641 + (4.162 * 10^{-3}T) + (9.093 * 10^{-6}T^2) - (4.717 * 10^{-8}T^3)$	*Equation b*
Neutron Radiation	$g(e^-_{solv}) = 0.96 + (1.09 * 10^{-3}T)$	*Equation c*

2.3.2 Methanol Radiolysis

In methanol, radiolysis splits the molecule (Reaction 9) to produce e^-_{solv} which is consumed *via* Reaction 10 [56]:

$$CH_3OH + Ionizing\ Radiation \rightarrow CH_3OH^+ + e^-_{solv} \qquad \textit{Reaction 9}$$

$$CH_3OH_2^+ + e^-_{solv} \rightarrow CH_3OH + H \qquad \textit{Reaction 10}$$

The *g*-values in Table 2 are from sources that measure the e^-_{solv} in methanol in the presence of gamma irradiation using various scavenging substances and measurement techniques.

Table 2: Literature g-values for gamma radiolysis in methanol samples [57].

Experimental e^-_{solv} Quantification Method	Literature e^-_{solv} *g*-values (e^-_{solv} · 100 eV^{-1})
Scavenged with $NiCl_2$ and $CoSO_4$	1.05
Scavenged with Nitrous Oxide	2
Scavenged with Nitrous Oxide and Sulfuric Acid	2
Scavenged with CH_3Br and SF_6	1.05
Scavenged with H_2SO_4	1.1

No literature was found reporting e^-_{solv} *g*-values in methanol from neutron radiation. This research will not be able to calculate a complete theoretical yield of e^-_{solv} in methanol samples. This thesis accepts this source of error, highlighting that neutron radiation is a minor contributor to e^-_{solv} production in water (see Table 1), and a similar assumption is made for methanol. Furthermore, all PFAS experiments are done in water solutions, where the *g*-values reported consider all types of relevant radiation.

2.4 Nuclear Reactions and Reactors

Nuclear reactors operate by controlling the rate of nuclear fission reactions therein and managing the energy released. The fission reaction of ^{235}U is depicted in Figure 4. Absorption of a thermal neutron by ^{235}U causes the compound nucleus to split into two fission products, one heavy and the other light. This reaction also releases two to three fast neutrons and is accompanied by a large amount of kinetic energy [58]. Specifically, for the thermal fission of ^{235}U, 2.434 neutrons (on average) and 180.88 MeV are released per fission [34]. The rate at which the uranium atoms fission from one generation to the next is related to the criticality of the reactor, often referred to as the k_{eff} value. Operation of a nuclear reactor revolves around maintaining a criticality of $k_{eff} \approx 1$ [58].

A fissioning fuel core emits various types of radiation, including neutrons, alpha, beta, and photon radiation. This thesis will primarily concentrate on the transport and dose associated with neutrons and photons, as these constitute the predominant forms of radiation observed at the irradiated sites selected for experimentation.

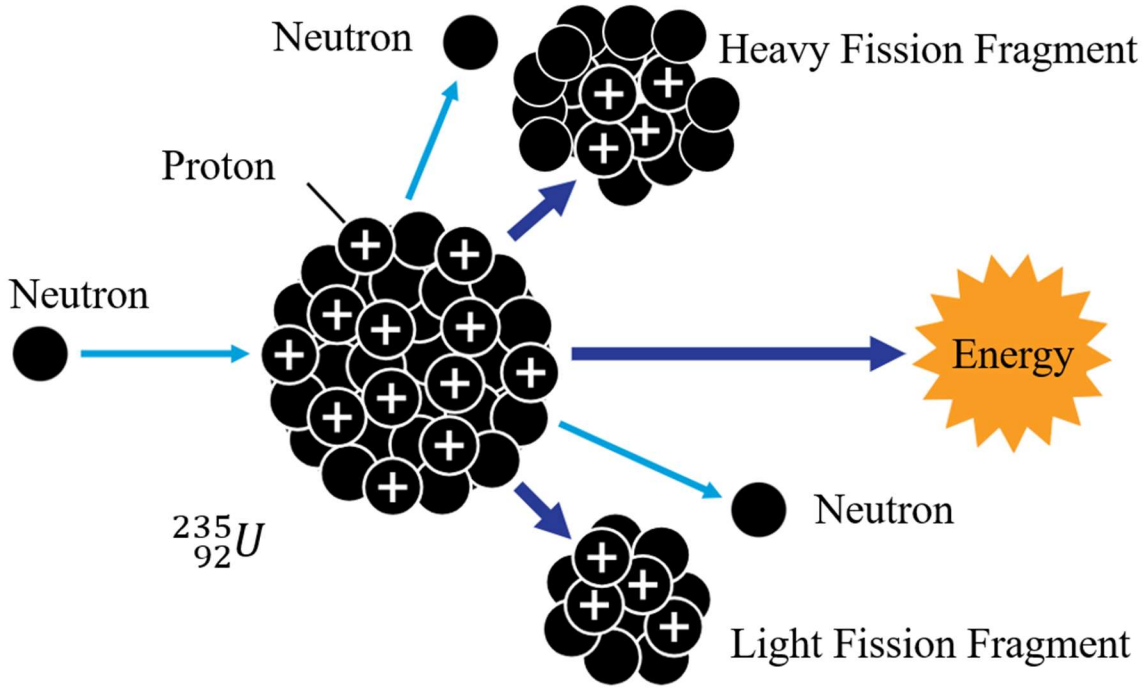

Figure 4: The ^{235}U fission reaction. Image adapted with permission from [59].

Neutron flux or photon flux describes the number of neutrons or photons travelling through a flat plane per a unit time. Common units are (neutrons or photons) per cm^2 per second, or ($n \cdot cm^{-2} \cdot s^{-1}$) and ($photons \cdot cm^{-2} \cdot s^{-1}$). These values describe the amount and density of the radiation passing through space and are necessary to understand the reaction kinetics inside the reactor.

The radiation dose describes the amount of energy absorbed into a medium from incoming radiation. As the radiation (*i.e.*, neutrons or photons) travels through a medium, several interactions can take place that impart energy from the radiation into the particles of the medium. The amount of energy imparted per unit mass of the medium is known as the dose and is measured in joules absorbed per kilogram of absorbing medium, or ($J \cdot kg^{-1}$). Another unit for dose absorbed, $MeV \cdot kg^{-1}$, is used herein. The rate at which the radiation dose is absorbed into the medium is also important, thus the dose rate is quantified and measured in units of $kJ \cdot kg^{-1} \cdot s^{-1}$ or $MeV \cdot kg^{-1} \cdot s^{-1}$ (1 MeV = $1.6022 \cdot 10^{-13}$) [58].

The dose absorbed by samples in this thesis is used to calculate the concentration of radiolysis products in irradiated samples.

2.4.2 RMC SLOWPOKE-2

The RMC SLOWPOKE-2 is a 20 kW_t thermal research reactor designed by AECL in the late 1960's [27]. It was commissioned at the RMC in 1985 and is fuelled with Low Enriched Uranium (LEU) [27]. The

reactor uses light water as both coolant and moderator. The RMC SLOWPOKE-2 fuel core is a source of mixed field radiation, with significant doses of both neutron and gamma radiation within the reactor's irradiation sites. The RMC SLOWPOKE-2 reactor is depicted in Figure 5.

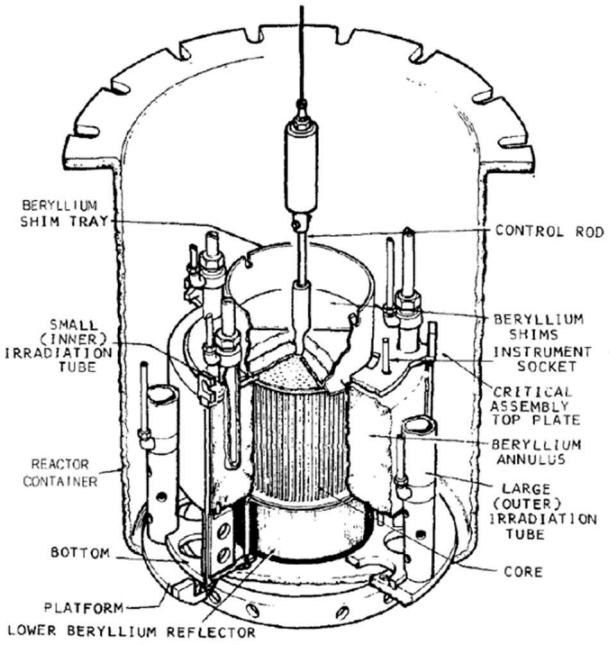

Figure 5: Design schematic of the SLOWPOKE-2 Nuclear Research Reactor at the RMC. Image used with permission from [32]

The reactor container includes several key research features. The first of these is the nuclear fuel core at the centre of the reactor. Surrounding it is the beryllium annulus. Importantly, there are inner and outer irradiation sites. The inner sites are placed within the beryllium annulus, and the outer sites are between the beryllium annulus and the reactor container. These allow small sample vials to be sent directly adjacent to the fuel core for irradiation. There are nine sites in total, labelled one through ten (shown in Figure 6). Outside of the reactor container is the pool irradiation site.

Multiple studies have made strides towards characterizing the mixed radiation field emitted by the RMC SLOWPOKE-2 reactor, with the results detailed and leveraged in *Chapter 3* of this thesis [40–43].

i. Andrews (1989) characterized the neutron flux through both computer models and neutron activation analysis (NAA) of samples irradiated at the inner and outer sites [28]. Andrews also used WIMS-CITATION [28] software to model neutron fluxes. NAA experiments involve exposing a sample of know isotope composition to a neutron field and measuring the resultant radiation from the sample. The results determine the flux of the neutron field exposed to the sample.
ii. Parent (2023) [32], Casper (2023) [31], and Huston (2024) [33] all completed similar neutron flux experiments to characterize the flux rates and/or dose rates at a larger number of irradiation sites within the RMC SLOWPOKE-2. Parent, Casper, and Huston each utilised the Monte Carlo N Particle (MCNP) software for their respective reactor models (*Section 2.5.1*) and corresponding data comparisons.
iii. Lamarre (1999) began the characterization of the photon dose rates within the inner, outer, and pool sites [29]. Again, dose rates were modelled with an updated WIMS-CITATION software and compared to experimental dose rates measured using thermoluminescent dosimeters (TLD), which were calibrated against a ^{60}Co source.

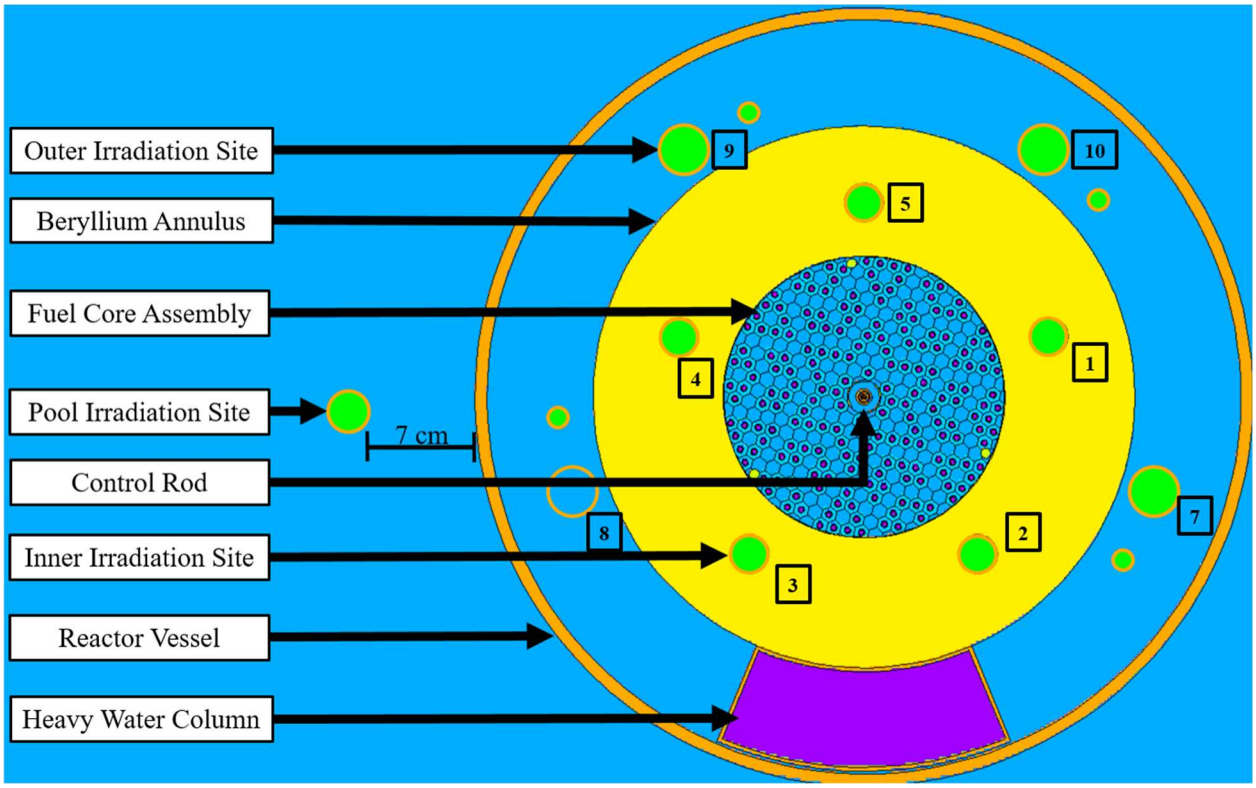

Figure 6: A horizontal cross section of the SLOWPOKE-2 reactor as modelled in this thesis. The reactor components are labelled. Site 8 is flooded and thus coloured as water.

2.4.3 PFAS Research in the RMC SLOWPOKE-2 Reactor

In 2018, Rook investigated the feasibility of degrading PFASs by exposing them to the mixed neutron and gamma radiation of the RMC SLOWPOKE-2 inner irradiation sites [20]. Rook found that PFAS defluorination and destruction were sensitive to both pH and DO content of the samples solution [20]. Rook recommended that further studies be completed to investigate the effects of anoxic and acidic conditions on the results [20].

In other experiments, Rook irradiated suites of different PFCAs and compared the degradation by the length of the molecule. Results demonstrated that the short chain PFCAs ($C < 8$) were more readily degraded than PFOA (the C8 PFCA) when mixed, as nearly no change in PFOA concentration was measured. However, results of isolated PFOA irradiation demonstrated up to 9.7 ± 0.7 % degradation. The preferential degradation of shorter PFCAs can be explained by their molecular structure. The perfluorinated carbon tails of all PFCAs create highly dense clouds of electrons. These dense electron clouds create unfavourable conditions for e^-_{solv} attack due to like-charge repulsion. Longer PFCAs have longer tails, increasing the size of the electron cloud and the magnitude of the repulsion experienced by e^-_{solv} when attempting to attack the molecule. Thus, e^-_{solv} preferentially attack shorter PFCAs in a mixed solution [20].

All irradiations in Rook (2018) were completed in the inner irradiation site #4. PFOA irradiation in any other site has not been tested prior to this thesis work. Simulations of the neutron and photon dose rates in each site are required to ensure samples irradiated in different sites absorb similar total doses. This allows the comparison of PFOA degradation to be considered as a function of irradiation time, dose rates, and neutron to photon ratios.

2.5 Monte Carlo N-Particle (MCNP) Simulation

Monte Carlo N-Particle (MCNP) is a radiation transport software designed to simulate various particles as they travel through modelled geometries [34]. The software was developed by Los Alamos National Laboratories (LANL). The latest version, MCNP6.3, released in August 2023, is used for this thesis.

For this thesis, the MCNP software was used to simulate the transport paths of neutrons, photons, and electrons through defined mediums using a Monte Carlo mathematical method. This method begins by determining a domain of possible paths for each particle, and probabilistically determines the outcome of every interaction between particles and the materials of the system [34]. The repetition of these probability-based computations can estimate expected results.

Simulations in MCNP are coded as a series of input decks, which defines geometry, materials, and the initial particle conditions. Additionally, the input deck defines which types of particles to track, referred to as the *mode*, and which values to count and report to the user, called *tallies* [34]. In the *NPE* mode, where neutrons, photons and electrons are simulated, MCNP calculates potential interactions between each particle and the modelled geometries/materials.

Also, MCNP enables the repetition of these calculations until results are confirmed to be significant statistically. The user designates the number repetitions through two inputs: *the number of histories* and *the number of cycles*. *Histories* is the number of times the software will repeat the transport and interaction calculations for the starting particle. *Cycles* is the number of times the software will repeat the total histories to determine the criticality of the modelled reactor.

MCNP software does not output results as a function of time; instead, results are normalized to a one-neutron event in the reactor. It transports the fractions of nuclear particles through space individually, and tallies how many land in the target cell. Tally results are reported as the fraction of the initial neutron that travelled through (flux) or interacted with (dose) the target space/geometry in the model. To analyze the results normalized to time in seconds, a scaling factor is required (Equation d). This factor considers the thermal power level of the reactor, the efficiency of energy released per fission, the criticality of the reactor, and the average number of neutrons released per fission event [30].

$$Scaling\ Factor = \frac{P_W\ (W) \cdot \nu\ (\frac{neutron}{fission})}{\left(1.6022 \cdot 10^{-13}\ \frac{J}{MeV}\right) \cdot k_{eff} \cdot w_f(\frac{MeV}{fission})} \qquad \textit{Equation d}$$

Where:

i. P_w – the power setting of the nuclear reactor being modelled,
ii. w_f – the efficiency of the energy released per fission,
iii. ν – The average number of neutrons released per fission; and
iv. k_{eff} – the effective criticality of the reactor during operation.

In the RMC SLOWPOKE-2 reactor model, the water moderator effectively thermalizes neutrons in the fuel bundle, thus it is assumed that ^{235}U in the fuel mainly undergoes fission. This assumption allows w_f to equal the energy released per ^{235}U fission; 180.88 MeV $\cdot$ fission^{-1} and a ν of 2.434 neutrons released per fission.

Unlike neutron and photon interactions, electron transport is modelled in MCNP6.3 as an average set of interactions [34]. This is an oversimplification required due to the highly complex nature of electron

transport (*N.B.,* the charge of an electron and small mass makes its interactions more chaotic). To save computational capacity, MCNP only simulates the average transport of sets of electron interactions.

A major update in the software version applied in this thesis, MCNP6.3, is the ability to simulate secondary reactions and the nuclear particles emitted. Thus, the impact of photons emitted from these secondary reactions is modelled. Unfortunately, due to the complexity of electron transport in MCNP, this feature is only feasible when operating in N and NP mode, and not in NPE mode [34].

2.5.1 MCNP Simulations of the RMC SLOWPOKE-2

The RMC SLOWPOKE-2 simulation has been under development and used by the RMC Nuclear Research Group since 2018 [20,31–33]. The works of Rook, Casper, Parent, and Huston have each progressed the RMC SLOWPOKE-2 reactor core simulation, which includes all nine irradiation sites, the reactor pool, and the fuel core in its post-refuelled (2021) configuration.

Originally, the simulation was based on a generic SLOWPOKE type reactor from Chalk River Laboratories (CNL) in MCNP5 [20]. This simulation code was modified by Rook in MCNP6.1 [20] to align it with the state of the RMC SLOWPOKE-2 in 2018. Rook conducted MCNP simulations to supplement the characterization of the SLOWPOKE-2. All MCNP simulations by Rook discussed herein were conducted with the reactor core modelled to simulate operation at nominal half power (10 kW_t). These reactor conditions simulated a thermal neutron flux of $5 \cdot 10^{11}$ neutrons$\cdot cm^2 \cdot s^{-1}$ within the inner irradiation sites [20]. The neutron flux simulations were benchmarked to NAA experiments. Further simulations analyzed the neutron and gamma dose rates within the nine irradiation sites. The results demonstrated that the inner sites experienced up to 45 % more gamma dose than the outer site, but only up to 20 % of the thermal neutron dose. These differences in radiation field composition will be important throughout this thesis.

In 2023, Casper and Parent [31,32] completed research using MCNP6.2 models of the RMC SLOWPOKE-2, further improving the model from Rook [20]. These include: a material library update, alignment of the fuel core orientation, modifying the fuel rod layout, density, and composition to a post-refuelled state as of in 2021 [32].

In 2024, Huston [33] extended the modelled geometry of the reactor to include the pool of water external to the reactor container. This extension allowed for simulations of the neutron flux in samples held in the pool instead of in the irradiation sites within the reactor container [33].

These works culminated in the MCNP6.2 model of the RMC SLOWPOKE-2 nuclear reactor used as a starting point for the simulation work completed in this thesis.

Chapter 3. MCNP Simulation Activities

3.1 Introduction

Investigating the viability of DPPH and the degradation of PFOA during irradiation experiments requires quantification of the dose absorbed by samples. Nuclear transport modelling software is used to predict the magnitudes of certain irradiation characteristics of the RMC SLOWPOKE-2 nuclear research reactor. While neutron flux can be reliably measured in isolation, other characteristics cannot be practically measured in the RMC SLOWPOKE-2. For example, neutron and photon dose rates are difficult to measure within a mixed, full-energy spectrum radiation field. Thus, MCNP6.3 can be applied to simulate the mixed radiation fields produced in the RMC SLOWPOKE-2 nuclear reactor and tally the desired characteristics.

An updated and modified model of the RMC SLOWPOKE-2 reactor from Parent, (2023) [32] is applied in this thesis. The simulated outputs of this model are confirmed by comparing to relevant literature for neutron flux and photon dose rate values.

Novel MCNP modelling in this thesis involves the simulation of nuclear particles produced from both fission and non-fission reactions in the RMC SLOWPOKE-2 nuclear reactor. Non-fission reactions simulated include nuclear decay reactions (*e.g.*, α, β, γ, and neutron decay reactions). Nuclear particles (*i.e.*, neutrons, photons, electrons) from non-fission reactions are referred to as secondary particles for the remainder of this thesis.

The ability of MCNP6.3 to model the e^-_{solv} population is assessed in this chapter. Results indicate that the MCNP6.3 software is limited in its ability to model specific electron populations (*i.e.,* e^-_{solv}. As direct simulation of the e^-_{solv} population in MCNP is not possible, dose rate simulations (*i.e.,* of neutrons, photons, and electrons) can be combined with *g*-values (*Section 2.3*) to calculate the yield of e^-_{solv} during irradiations.

This chapter achieves *Thesis Goal #1*, namely, to *apply MCNP6.3 software to predict the yield of* e^-_{solv} *in samples irradiated in the RMC SLOWPOKE 2*.

This goal is achieved in the following steps:

i. Earn confidence in the RMC SLOWPOKE-2 model developed for this thesis,
ii. Simulate the dose rates of the mixed radiation field across reactor irradiation sites of interest; and
iii. Combine simulation dose rates and literature *g*-values to calculate a theoretical yield of e^-_{solv} during irradiation within the RMC SLOWPOKE-2.

3.2 Methodology

The MCNP6.3 model developed in this work reflects the RMC SLOWPOKE-2 nuclear reactor state from 2021, immediately after the new fuel core was installed. Simulations in this chapter applied N P mode in simulations of neutrons and/or photon tallies, whereas the N P E mode is used in electron tally simulations (see *Section 2.5*). Models simulate 115 cycles of particle histories and discard the first 15 cycles to calculate the k_{eff} of the simulated reactor. The reactor control rod height is corrected to reflect the reactor at a nominal half power (10 kW_{th}) after the 2021 refuelling. The fuel cage in the reactor core was updated to enable the transport of electrons during simulation. The water pool outside the reactor container includes pool site samples. Ten sample vials are simultaneously modelled in the inner, outer, and pool sites.

Between one and twenty million source particle histories are run per simulation, varying with the complexity of the particles simulated[‡]. Recall literature models apply between 250,000 to one million histories [20,31–33]. The increase in particle histories is enabled by concurrently reporting flux and dose rate tallies in samples at each of the ten irradiation sites.

Samples irradiated in this work are in either water or methanol solvents. Water is available in the MCNP6.3 material library; however, methanol is not. For this thesis, methanol samples are modelled as a generic material at 25.5 °C, with a density 0.7866 $g \cdot cm^{-3}$, comprised of hydrogen, carbon and oxygen at ratios of 4-1-1, respectively. All elements are in their natural isotopic abundances. The atoms are considered homogenous across the volume of sample cells. Other properties of methanol (*e.g.,* interaction information specific to the molecular structure) is not available in MCNP6.3, and thus, are not simulated in this thesis.

Appendix A Samples MCNP6.3 Input Code includes the major changes made in this thesis to the MCNP6.3 input code of the RMC SLOWPOKE-2 reactor, the tallies requested from the software, and the run parameters. Appendix B Sample MCNP6.3 Output Code presents the sections of the output code relevant to the results in this thesis.

3.3 Results and Discussion

3.3.1 MCNP6.3 Model and Literature Comparison

The MCNP6.3 model developed in this thesis for the RMC SLOWPOKE-2 nuclear research reactor builds on models from previous research [20,30–33], which used older versions of MCNP. This thesis used the latest version of MCNP (MCNP6.3). Baseline simulations were performed to ensure the Rook, Parent, and Huston models could be replicated in MCNP6.3. After benchmarking, neutron and photon dose rates were simulated at inner, outer, and pool irradiation sites, and the ability of MCNP6.3 to predict e^-_{solve} concentrations was evaluated.

The simulated neutron fluxes in water samples irradiated at the inner and pool sites in this model are compared to reported simulated and experimental measurements from the following publications:

i. Andrews, 1989 [28],
ii. Rook, 2019 [20],
iii. Casper, 2023 [31],
iv. Parent, 2023 [32]; and
v. Huston *et al.*, 2024 [33].

The simulated photon dose rates in water samples in the irradiation sites from the model in this thesis are compared to reported experimental values from Lamarre, 1999 [29].

Comparing the neutron flux simulated in this thesis to reported literature necessitates that this work applies the same energy definitions for thermal, epithermal, and fast neutrons used in the past. Table 3 presents these different neutron energy definitions.

Most of the publications listed above (i to iv) apply a general energy definitions that can be found in standard references (*e.g.,* in Lamarsh [58]). However, Huston *et al.* [33] applies different neutron energy

[‡] Increasing the number of histories simulated decreases the uncertainties of the results, but increases the computational time required to complete the simulation. A balance of these factors is found within this range based on the specific simulation parameters.

definitions, based on the neutron activation characteristics of gold and cobalt [60]. The model developed in this thesis simulates both energy definitions and compares neutron flux results to literature accordingly.

Table 3: Neutron energy range definitions for neutron flux simulations used in this thesis.

Energy Definition	Thermal Neutrons (eV)	Epithermal Neutrons (eV)	Fast Neutrons (eV)
Lamarsh [58]	0 – 0.625	0.625 – 4	4 – 10000000
Huston *et al.* [33]	0 – 0.5	0.5 – 1000	1000 – 10000000

Figure 7 compares the neutron flux values at inner site # 4 from simulation results for this work (rightmost columns) to simulation and experimental results from literature (for i to iv listed above). All neutron fluxes in Figure 7 are based on the Lamarsh [58] neutron energy definition from Table 3. Simulation considers only fission particles.

Considering the neutron flux results from literature in Figure 7 (the leftmost bars in each energy group), the neutron flux simulated in this thesis agrees with the results from Andrews (1989) and Rook (2019) (the solid blue and hollow red columns). *N.B.*, Andrews, (1989) applies a WIMS-CITATION simulation software, not MCNP, and does not report values for epithermal nor fast neutron flux [28].

The reported fluxes from Casper (2023) and Parent (2023), the black and yellow columns with diagonal fills, are lower than Andrews, (1989), Rook, (2019), and this work, across all neutron flux energies. This is because Casper, (2023) and Parent, (2023) simulated the nominal reactor power at 9.6 kW_{th}, whereas Andrews, (1989), Rook, (2019), and this work, simulate the reactor thermal power to be the nominal half power of 10 kW_{th} [20,28,31,32]. Accounting for these differences, the model from this work reports neutron fluxes in agreement with the literature.

With respect to the uncertainty ranges cited in Figure 7, Andrews, (1989) assumes uncertainty of 5% due to the transport simplifications made in the WIMS software. MCNP simulated results from Rook, (2019), Casper, (2023), Parent, (2023), and this work, report uncertainties calculated in the software. The magnitude of calculated MCNP uncertainties is related to the number of particle histories simulated.

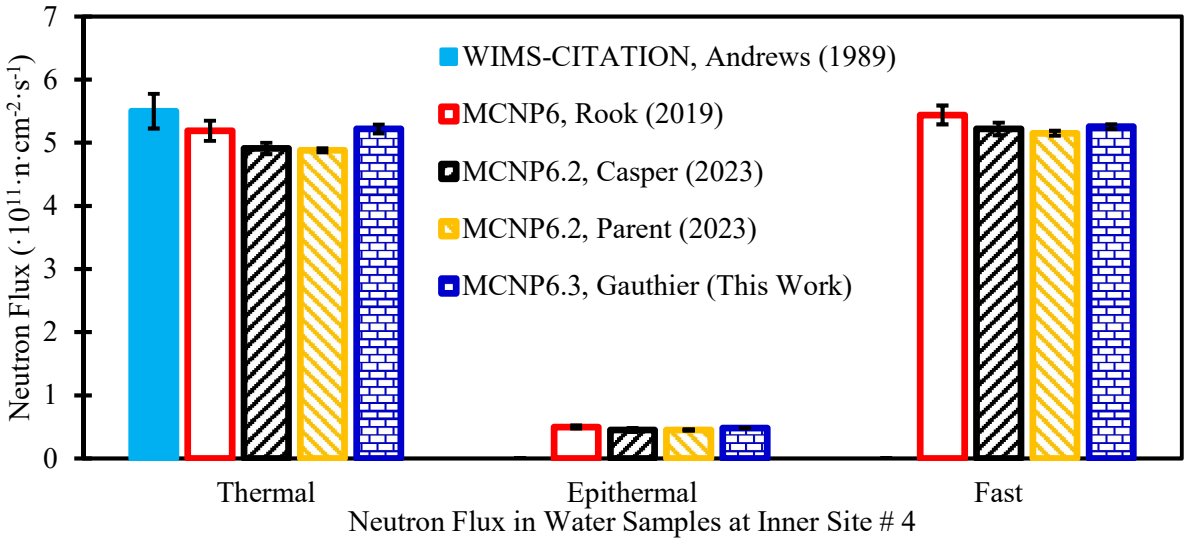

Figure 7: Neutron flux results simulated in this thesis and in literature [20,28,31,32]. Flux is simulated in water samples irradiated at inner site # 4. Error bars from Andrews (1989) represent a 5% uncertainty based on the reliability of the WIMS-CITATION software. The remaining error bars are the uncertainty results calculated by MCNP. Uncertainty of results from this thesis range from ± 0.0014 to ± 0.0026 $\cdot 10^{11} \cdot n \cdot cm^2 \cdot s^{-1}$.

Figure 8 shows a comparison between simulated and experimental neutron flux values at the pool irradiation site between Huston *et al.*[33] and the results simulated in this work. All simulation results apply the Huston *et al.* [33] neutron energy definitions. *N.B.,* Huston *et al.* does not report experimental values for epithermal or fast neutron flux. All simulation results only consider fission particles. Again, the uncertainty values for all MCNP results are calculated in the software. For experimental results from Huston *et al.*, uncertainty is based on the standard deviation of replicate measurements.

Simulation results from this work and Huston *et al.* regarding the thermal neutron flux (the first and last columns in the leftmost group of Figure 8) under-predict the reported experimental results (the middle two columns). The discrepancy is likely caused by the reactor power being set to a higher nominal power (*i.e.,* slightly greater than 10 kW_{th}) during experiments of Huston *et al.*, whereas the scaling factor applied to both simulations assumes the reactor is operating at 10 kW_{th}, the nominal half power.

Ongoing research, concurrent to this thesis, studies the nominal thermal power of the RMC SLOWPOKE-2 reactor. Simulating a higher nominal thermal power would report neutron fluxes in agreement with the experimental results in Huston *et al.* [33]. Rather than choose a new value solely to agree with the experimental measurements from literature, future work is entrusted to apply a nominal power once confirmed by ongoing studies to the values presented in this thesis.

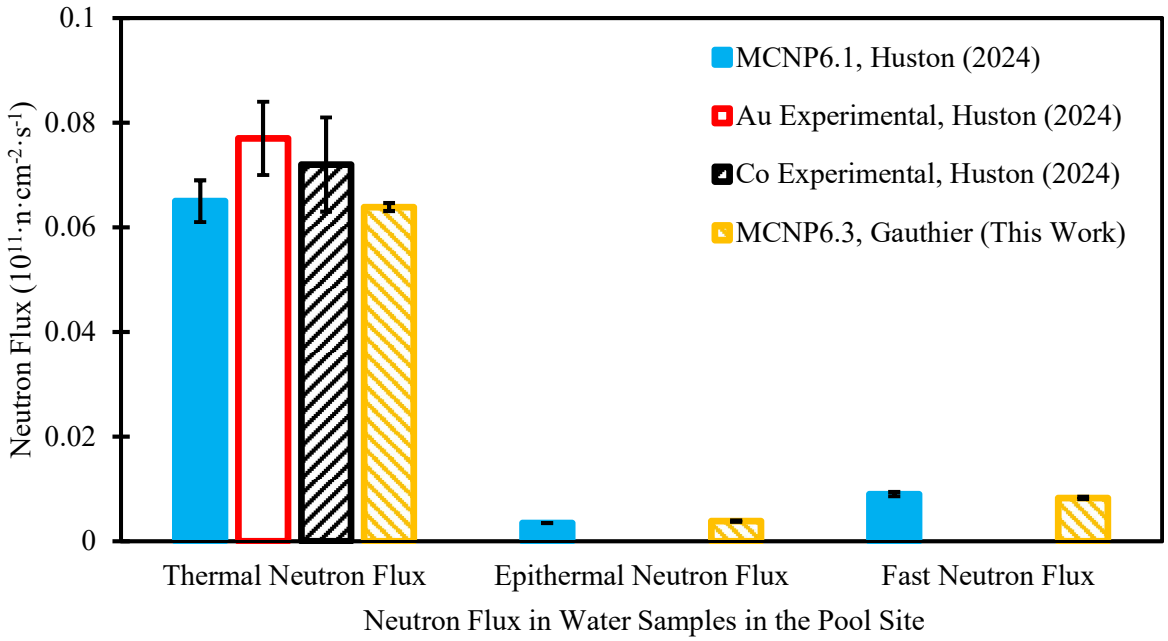

Figure 8:Neutron flux results simulated in this thesis and in literature[33]. Flux is simulated in water samples irradiated at the pool site. The error bars represent the uncertainty of results calculated in MCNP and the standard deviation of experimental results. Uncertainty for epithermal and fast neutron fluxes for this work range from ± 0.00002 ·10^{11}n·cm^{-2}·s^{-1} to ± 0.0004 ·10^{11}n·cm^{-2}·s^{-1}.

Analysis of Figure 7 and Figure 8 confirm the developed model produces neutron fluxes in agreement with literature [20,28,31–33]. Such comparisons to literature earn confidence in the model developed for this thesis and its application to subsequent simulations. This thesis model is now applied to *Thesis Goal #1: Predicting e^-_{solv} yield during irradiation through dose rate simulations.*

3.3.2 RMC SLOWPOKE-2 Dose Rates Simulation

There are several electron transport capabilities within MCNP6.3, and their application to *Thesis Goal #1* was uncertain. Such features require investigation to determine which (if any) are applicable to the goal of this chapter.

The following MCNP6.3 electron transport capabilities were investigated:

i. Electron tagging operations;
ii. Charge deposition; and
iii. Electron flux tallies.

The results of simulations complete in this work found the features listed above cannot be applied to *Thesis Goal #1* to simulate e^-_{solv} populations directly. The various inhibiting factors are discussed below.

i. *Electron tagging operations* is limited to predicting secondary electrons from select reactions, including Auger electrons and knock-on electrons, but omit others.
ii. The *charge deposition tally* is not applicable to the three-dimensional situation this thesis investigates and fails to count electrons produced and consumed within the same cell.
iii. *Electron flux tallies* are limited to tallying the total electron flux or dose rate and cannot distinguish between high-energy electrons emitted from nuclear reactions and the radiolytically-produced e^-_{solv}.

If any of these options were sufficiently developed in the MCNP6.3 software to quantify the electron concentration in a cell volume during irradiation, the values would be for total electrons. MCNP6.3 would also require software capable of transporting the tallied electrons through solvation mechanics to determine how many would become solvated rather than undergo germinate recombination.

Whilst MCNP6.3 is not equipped to simulate e^-_{solv} yield directly, combining simulated dose rates (for neutrons, photon, and electrons) with *g*-values can be used to estimate the production rates of radiolysis products. This method is used in literature, and is recommended for complex radiation fields [61].

Such simulations and calculations are completed and discussed below for samples of water and methanol. This section describes the simulation of neutron, photon, and electron dose rates in the RMC SLOWPOKE-2 inner, outer, and pool irradiation sites. The subsequent section applies such dose rates to calculate theoretical yields of e^-_{solv}. Results in methanol samples are referred to in *Chapter 4* and results in water samples will be referred to in *Chapter 5*.

Previous models of the RMC SLOWPOKE-2 reactor did not include secondary particles [20,30–33], thus the impacts and necessity of including such particles is investigated herein.

Figure 9 compares the experimental photon dose rates from Lamarre [29] (see *Section 2.4.2*) to simulated photon dose rates from two models developed for this thesis:

i. A model that considers *only fission particles*; and
ii. A model that considers *fission and secondary particles*.

Examining the dose rates in Figure 9 from left to right (*i.e.*, from the inner sites to the pool sites), both experimental and simulated results decrease as their radial distance from the core increases. *N.B.*, at the inner site (leftmost group of columns), the simulation of secondary particles (hollow red column) increases the photon dose rate to agree with the TLD measurements (solid blue column). Whilst the inclusion of secondary particles increases simulated dose rates in all three irradiation sites, the TLD results remain higher than the simulated dose rates in the outer and pool sites (the centre and right groups of columns). An over-counting of low-energy photons by the TLD (caused by the high energy photon calibrations) is likely

responsible for the discrepancy of dose rates in the outer and pool sites [29]. It is assumed that the experimental results at the outer and pool sites are overestimations of the photon flux. It is believed that the photon dose rate is lower than measured in Lamarre (1999), and more in line with the results simulated in this thesis. Future experimental work is required to confirm this assumption.

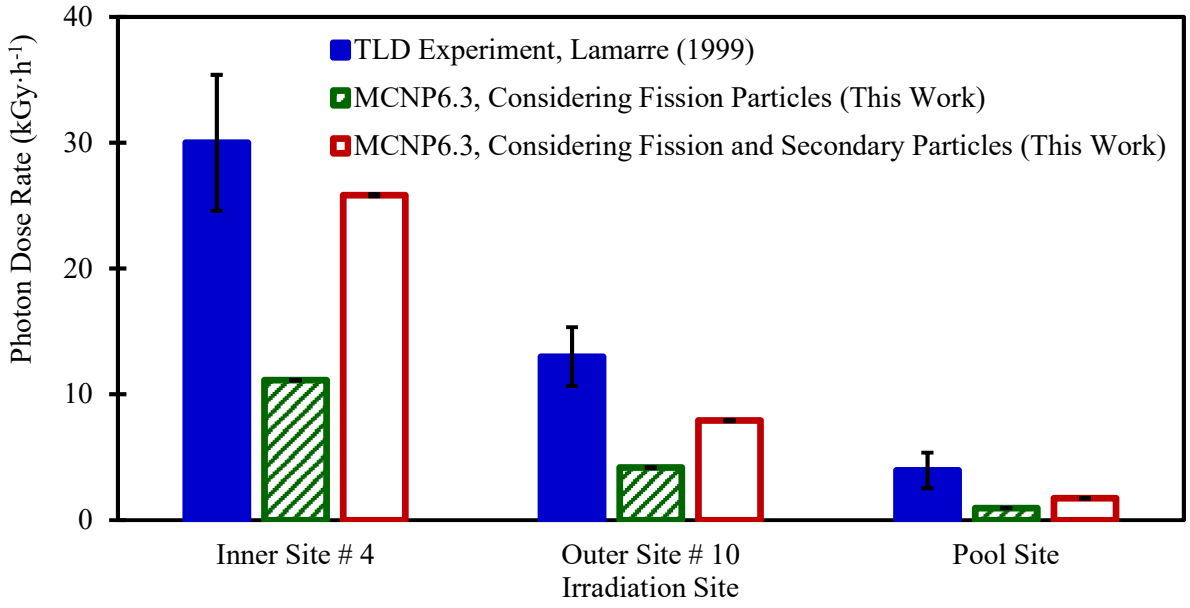

Figure 9: RMC SLOWPOKE-2 photon dose rates; experimentally determined using TLDs [29] and simulated results from this thesis in key irradiation sites. All values represent water samples. Uncertainty of results from this work are too small to see and range from ± 0.01 to ± 0.08 kGy·h^{-1}.

Further analysis, along with detailed results of the thesis models compared in Figure 9, is found in Appendix C Additional Fission and Secondary Particle Flux and Dose Rate Comparison Data. A key finding from the analysis is that no change in neutron fluxes or neutron dose rates is observed in any irradiation site or sample solvent when secondary particles are considered. Thus, the confidence in the developed model earned in *Section 3.3.1* is unaffected by the inclusion of secondary particles.

Figure 10 compares the neutron to photon dose ratios from simulations in this thesis that *consider* and *do not consider* secondary particles (the striped and non-striped columns, respectively). The inclusion of secondary particles has a significant effect on the neutron to photon ratio. The decrease in neutron to photon ratio observed with the addition of secondary particles is expected and proportional to the increase in photon dose rate. Neutron dose predominates inner site # 4 (leftmost columns) when secondary particles are not considered, where there are neutron to photon ratios of 1.7 and 1.8 for water and methanol, respectively.

By including secondary particles, the neutron to photon ratio at the inner site drops to slightly below unity. This is expected given contribution of neutrons to the production of secondary particles and the significant neutron population close to the reactor core.

Considering simulations further from the reactor core (*i.e.,* outer and pool sites, the centre and rightmost groups respectively), secondary particle contributions reduce the simulated neutron to photon dose ratio, albeit to a lesser degree than at the inner site. Again, this is expected due to the neutron contribution to secondary particle production and the reduced neutron populations at sites further from the reactor core [30].

Focussing now on the inclusion of secondary particles, it can be seen in Figure 10 that the photon dose predominates the radiation field within the inner, outer, and pool sites (*i.e.*, the striped columns are all in the photon dose dominant region of the figure). The dose ratios decrease from 0.8 to 0.1 as the distance from the reactor core increases. Access to three distinct mixed radiation fields offers the unique opportunity to investigate the impact such fields have on radiolysis produced e^-_{solv} populations.

Moving forward, secondary particles are included in the model due to the results from Figure 9 and Figure 10. Considering the limitations of Lamarre, (1999) [29], ongoing concurrent research includes experimental measurements of the radiation dose rates, and when building on this thesis, future work should consider such results to validate simulated values.

Thesis Goal #1 requires simulated neutron, photon, and electron dose rates to predict the e^-_{solv} yields in irradiated samples. Further, dose rate information provides important insights when considering and comparing radiation effects in *Chapter 4* and *Chapter 5*. The following section provides this dose rate information.

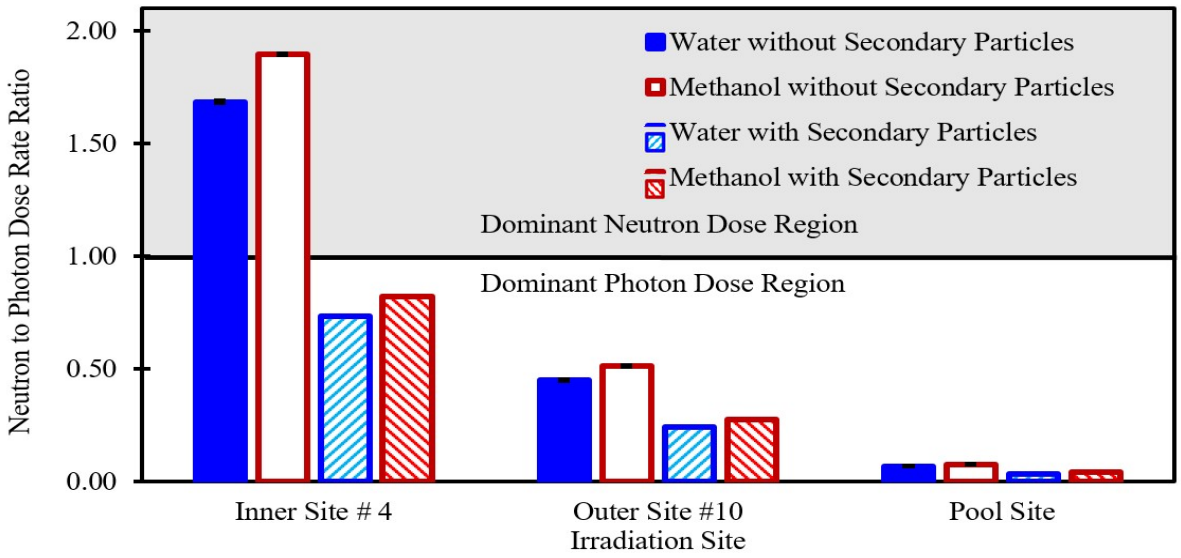

Figure 10: Neutron to photon dose rate ratios at the three key irradiation sites, in simulations that did and did not consider secondary particles. The black line at 1 represents the division between neutron (top half, grey area) and photon (bottom half, white area) dose rate dominated regions of the RMC SLOWPOKE-2. Error bars are too small to see in this figure, and represent the calculated uncertainty from the MCNP6.3 software. Uncertainty ranges from ± 0.002 and ± 0.005.

Figure 11 compares the simulated dose rates at various key irradiation sites in the RMC SLOWPOKE-2 reactor for neutrons, photons, and electrons. Both water and methanol samples are simulated. Comparing the two media across the various sites, (the solid *vs.* hollow columns) the dose rates are very similar. Additionally, all dose rates (*i.e.*, neutron, photon, and electron) decrease in as radial distance from core increases. Examining the neutron dose rates at the inner site in isolation, a slight difference between the dose rates absorbed in water versus in methanol becomes clear. The observed difference likely originates from the lack of molecular interaction information for methanol samples (see *Section 3.2)*. The four hydrogen atoms in the methanol as modelled (compared to the two in water) are un-bonded to the heavier carbon and oxygen, and thus likely responsible for absorbing an unrealistically high amount of energy from inbound neutrons through scattering reactions. Again, minor neutron impacts observable only at the inner site are inevitable, as the neutron population decreases rapidly as radial distance from the reactor core increases [28,30–33].

When considering the electron dose rates in Figure 11, note that MCNP6.3 applies an oversimplification to electron transport, and that secondary particles cannot be practically applied to electron tallies (see *Section 2.5*). Considering these factors requires the electron dose rates presented in this thesis be taken as a conservative estimate. Future work should validate the electron dose rates simulation results experimentally.

Whilst photon dose rates are compared to the experimental results from Lamarre, (1999) in Figure 9, the neutron and electron dose rates presented in Figure 11 are not independently confirmed. As improved dose rate measuring capabilities become available, future work should aim to confirm the true values for neutron and electron dose rates across the RMC SLOWPOKE-2 irradiation sites and apply them to increase the accuracy of modelled results beyond current capabilities.

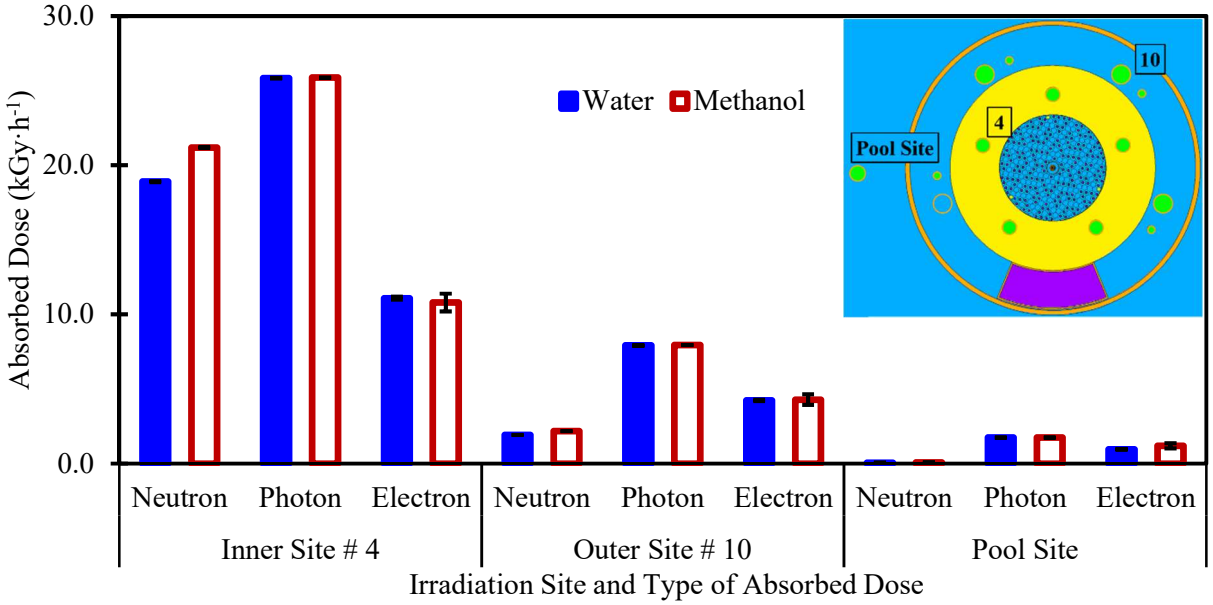

Figure 11: Simulated neutron, photon, and electron dose rates across RMC SLOWPOKE-2 irradiation sites for samples in water and methanol. Uncertainty ranges from ± 0.0015 kGy·h^{-1} to ± 0.6 kGy·h^{-1}.

Further progress towards calculating e^-_{solv} populations within the RMC SLOWPOKE-2 is made in the following section, where the simulated dose rates from Figure 11 are combined with *g*-values (see *Section 2.3*) to calculate the yield of e^-_{solv} in samples irradiated at the inner, outer, and pool sites.

3.4.3 Solvated Electron Yield Calculation

In this chapter, the *g*-values for e^-_{solv} in water are calculated using Equation b Equation c (Table 1 in *Section 2.3.1*) in combination with the water temperature inside the RMC SLOWPOKE-2 during irradiation, 30 ± 15 °C [62]. The calculated *g*-value for e^-_{solv} production in water by photon and electron radiation[§] is consistent with experimental results from literature [50,63]. The *g*-values for e^-_{solv} production in methanol are an average of literature values (see *Section 2.3.2*).

[§]The AECL report [55] is the only literature found by this work that discussed neutron radiation in relation to e^-_{solv} *g*-values.

Table 4 lists the *g*-values used to calculate a theoretical yield of e^-_{solv} in the RMC SLOWPOKE-2 irradiated samples of both water and methanol. The *g*-value selection criteria are discussed in *Section 2.3*. Considering the dose rates from Figure 11, the *g*-values in Table 4 demonstrate the varying degrees to which neutron, photon, and electron radiation, impact the calculated e^-_{solv} yields. In water, electron and photon radiation have significantly higher *g*-values than neutron radiation. In methanol samples, electron radiation contributes more than photon radiation as demonstrated by the higher *g*-value.

Table 4: Literature G-values for solvated electron yields during irradiation applied in this thesis.

Sample Solvent	Type of Radiation Measured	Literature *g*-Values for e^-_{solv} (molecules · 100 eV^{-1})
Methanol[57,64]	Photon Radiation	1.5 ± 0.5*
	Electron Radiation	4.1
Water [55]	Photon Radiation	2.77 ± 0.08**
	Electron Radiation	2.77 ± 0.08**
	Neutron Radiation	0.99 ± 0.02**

** Value is an average of the values in Table 2*

*** Values differ by temperature. The uncertainty on these values include the entire range of temperatures in the RMC SLOWPOKE-2 during irradiation experiments[62].*

The *g*-values from Table 4 and the dose rate values from Figure 11 are combined, as per Equation e. Figure 12 presents the calculated e^-_{solv} yield at the inner, outer, and pool sites during irradiation in the RMC SLOWPOKE-2 operating at nominal half power (10 kW_{th}). Detailed e^-_{solv} yield results are in Table 5.

$$Radiation\ Dose\ Rate * \text{g-}value * Time\ Irradiated = Solvated\ Electron\ Yield \qquad \textit{Equation e}$$

Observe the varying uncertainties between water and methanol samples (Table 5). Unlike water, the methanol in the model is an estimate that does not consider any molecular bonding, leading to greater dose rate uncertainty. Also, electron dose rates are a conservative estimate, as electron transport follows a simplified transport method in MCNP6.3, and the electron dose rates are from models that do not consider secondary particles.

Examining the results in Figure 12 from left to right (*i.e.*, as radial distance from the reactor core increases), the e^-_{solv} yield from all radiation sources decrease. This is expected, as per Figure 11, the dose rates responsible for radiolytically producing e^-_{solv} decrease in the same manner.

Focusing now on the inner and outer site results (see the dose rate results from Figure 11), the inner site (leftmost group of columns) experiences a total dose rate four times greater than at the outer site (centre group), yet the e^-_{solv} yield at the inner site is only about three times greater than at the outer site. This discrepancy is expected, as the inner site dose rate has a larger contribution from neutron radiation, which yields the fewest e^-_{solv} per dose absorbed (see Table 4). Considering the outer and pool site results (the centre and rightmost groups), a similar relationship between e^-_{solv} yield and dose ratios is present. The ratio of neutron to photon radiation unique to each site have a complex interaction with e^-_{solv} yields. Such differences demonstrate the value of the mixed radiation field and unique irradiation sites within the RMC SLOWPOKE-2, as applied to e^-_{solv} yield research.

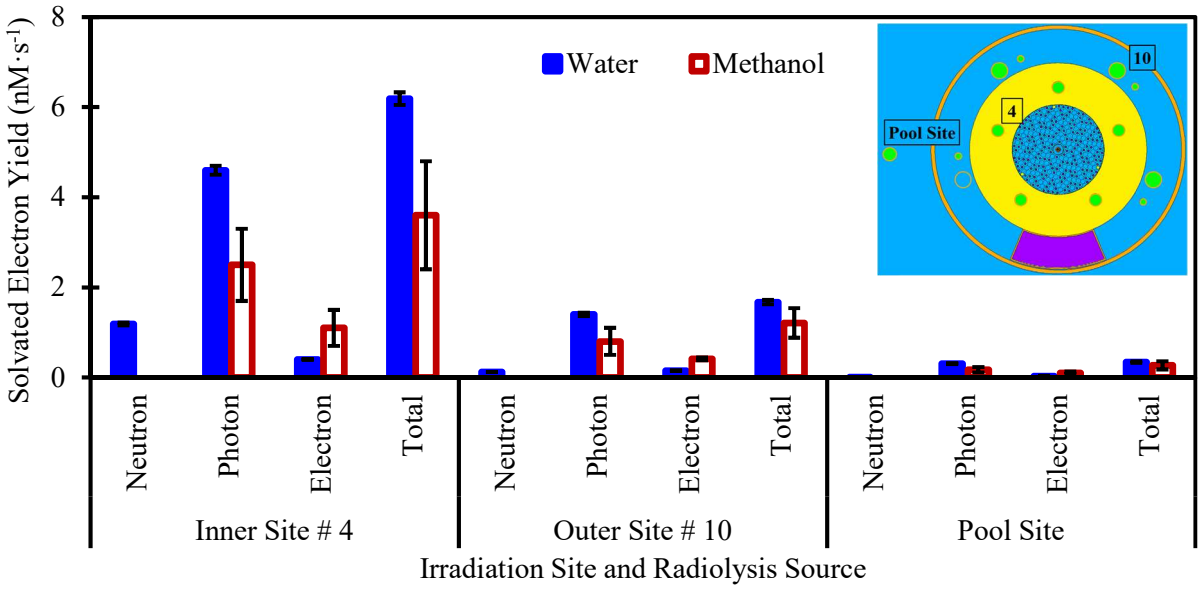

Figure 12: Calculated solvated electron yields from neutron, photon, and electron radiolysis across the RMC SLOWPOKE-2 irradiation sites for samples in water and methanol. Some error bars are too small to see, with uncertainty ranges from ± 0.00008 nM·s^{-1} to ± 1.2 nM·s^{-1}.

Table 5: Calculated solvated electron yields at the RMC SLOWPOKE-2 irradiation sites. Simulated fission and secondary dose rates in water samples from Figure 11 and literature g-values from Table 4 are combined using Equation e.

Sample Solvent	Radiation Dose	RMC SLOWPOKE-2 Irradiation Site	Solvated Electron Yield (nM·s^{-1})
Water	**Photon**	Site # 4	4.6 ± 0.1
		Site # 10	1.40 ± 0.04
		Pool Site	0.308 ± 0.009
	Electrons	Site # 4	0.40 ± 0.01*
		Site # 10	0.152 ± 0.005*
		Pool Site	0.03 ± 0.01*
	Neutrons	Site # 4	1.19 ± 0.03
		Site # 10	0.121 ± 0.003
		Pool Site	0.00364 ± 0.00008
	Total	Site # 4	6.20 ± 0.2
		Site # 10	1.673 ± 0.05
		Pool Site	0.34 ± 0.02
Methanol	**Photon**	Site # 4	2.5 ± 0.8
		Site # 10	0.8 ± 0.3
		Pool Site	0.17 ± 0.06
	Electrons	Site # 4	1.1 ± 0.4*
		Site # 10	0.41 ± 0.03*
		Pool Site	0.10 ± 0.03*
	Total	Site # 4	4 ± 1
		Site # 10	1.2 ± 0.6
		Pool Site	0.27 ± 0.09

**Using a dose rate considering only fission particles.*

Additionally, several of the simulation dose rates presented in this chapter have not been previously reported in literature [20,28–33] and further the understanding of the radiation effects present in the RMC SLOWPOKE-2. Again, while confidence in the model applied is earned through literature comparisons, neutron, photon, and electron dose rate measuring techniques effective in the RMC SLOWPOKE-2 reactor conditions are required to validate the simulated/calculated results presented in this chapter.

3.4 MCNP Conclusions

Calculated e^-_{solv} yields presented in this chapter accomplish *Thesis Goal #1: Apply MCNP6.3 software to predict the yield of e^-_{solv} in samples irradiated in the RMC SLOWPOKE-2.* Calculating the yields of e^-_{solv} at the inner, outer, and pool irradiation sites was made possible by combining each step taken in this chapter. First, the model applied was confirmed through literature comparisons. Next, the dose rates of the neutron, photon, and electron radiation were simulated. Newly introduced features in the software, such as the simulation of secondary particles, increased the simulated photon dose rates to agreement with experimental results from literature. Finally, the simulation work of this thesis was completed by combined *g*-values with the simulated dose rates, calculating the yield of e^-_{solv}.

As discussed throughout this chapter, the following findings were key to accomplishing *Thesis Goal #1*:

i. The RMC SLOWPOKE-2 model developed in this work agrees with simulation and experimental results from literature, establishing confidence in the model and enabling its application to Thesis Goal *#1*,
ii. The electron tallying features of MCNP6.3 are insufficient to directly predict radiolytically produced e^-_{solv} populations, and therefore achieves *Thesis Goal* #1 by simulating dose rates and combining them with literature g-values; and
iii. The effect of simulating secondary particles contributes to predicting the photon dose rates in the RMC SLOWPOKE-2.

The following two chapters will detail and discuss irradiation experiments in the RMC SLOWPOKE-2 and will regularly consider both the dose rates and the e^-_{solv} yields presented in this chapter to analyze results of irradiation experiments.

Chapter 4. DPPH Viability Assessment Activities

4.1 Introduction

DPPH· is a stable free radical, frequently applied in studies to measure the reducing capacity of a given solution [35,65–67]. Measurement is completed by comparing the concentration of DPPH· that is reduced to DPPH:H during exposure, *via* Reaction 11. This reduction reaction takes place when DPPH· is exposed to a reducing environment: DPPH· reacts with an electron (e^-) and a proton, forming diphenyl-picrylhydrazine (DPPH:H). The concentration of e^-_{solv} that reduce DPPH· is proportional to the Δ [DPPH·]. The Δ [DPPH·] is measured *via* UV and visible light spectroscopy (UV-Vis) and the analysis of characteristic absorbance peaks. Quantifying the e^-_{solv} that react with DPPH· during irradiation provides insight into the concentration of e^-_{solv} related to the fluxes and dose rates of the nuclear reactor. This process of e^-_{solv} quantification with DPPH· is known as a DPPH assay.

$$DPPH\cdot + e^-_{solv} + H^+ \rightarrow DPPH{:}H \qquad \textit{Reaction 11}$$

A weakness of the DPPH assay is that DPPH· is sensitive to reduction during exposure to light [66]. However, by measuring the reduction in control samples, the reduction caused by radiolysis products during irradiation can be isolated and this weakness is mitigated.

The stabilities of both DPPH· and DPPH:H allow the UV-Vis measurements to be taken several days after irradiation. This is required as samples require time to decay from the neutron activation that occurs inside the RMC SLOWPOKE-2 during irradiation, before they can be safely removed from the reactor lab. The DPPH assay was selected for this thesis because it has been used previously in both neutron and photon radiation environments [68–70]. However, the fluxes and dose rates emitted by the RMC SLOWPOKE-2 are higher than those from the literature. Thus, it is necessary to confirm the viability of the method in the mixed radiation field of a nuclear reactor.

To determine if a DPPH assay is viable in samples irradiated in this thesis, DPPH must survive irradiation experiments without experiencing observable molecular degradation.

This chapter is focused on *Thesis Goal #2*, namely, to *investigate the viability of quantifying e^-_{solv} yields with DPPH· in the mixed field radiation environments of the RMC SLOWPOKE 2 irradiation sites*.

This goal is achieved in the following steps:

i. Confirm the UV-Vis spectroscopy capability to distinguish between DPPH· and DPPH:H in solutions, and measure the DPPH· reduction to DPPH:H in samples exposed to light, and
ii. Irradiate DPPH· samples in sites across the RMC SLOWPOKE-2 reactor and investigate the [DPPH·] and [DPPH:H] results with UV-Vis spectroscopy.

4.2 Methodology

4.2.1 The DPPH Assay

Both DPPH· and DPPH:H absorb characteristic wavelengths of UV and visible light, allowing for the quantification of DPPH· reduced to DPPH:H during irradiation. Additionally, both are also stable in solution and can thus be measured after radioactive isotopes in the irradiated solution have decayed to safe levels.

The UV-Vis absorbance spectrum of DPPH· (Figure 13) contains peaks at 256 nm, 324 nm, and 515 nm. The 256 nm and 324 nm light wavelengths are absorbed by the picryl group in DPPH. Both the radical and reduced forms of DPPH absorb light at these wavelengths, thus are used to identify DPPH· and/or DPPH:H

in solution [35,66]. However, the 515 nm peak is caused by the radical electron unique to DPPH·. The 515 nm peak is key to quantifying [DPPH·], differentiating [DPPH·] from [DPPH:H] [35,66]. Thus, measuring the Δ [DPPH·] acts as an indirect method of quantifying the [e^-_{solv}] available for chemical reactions in solutions irradiated in the RMC SLOWPOKE-2 reactor.

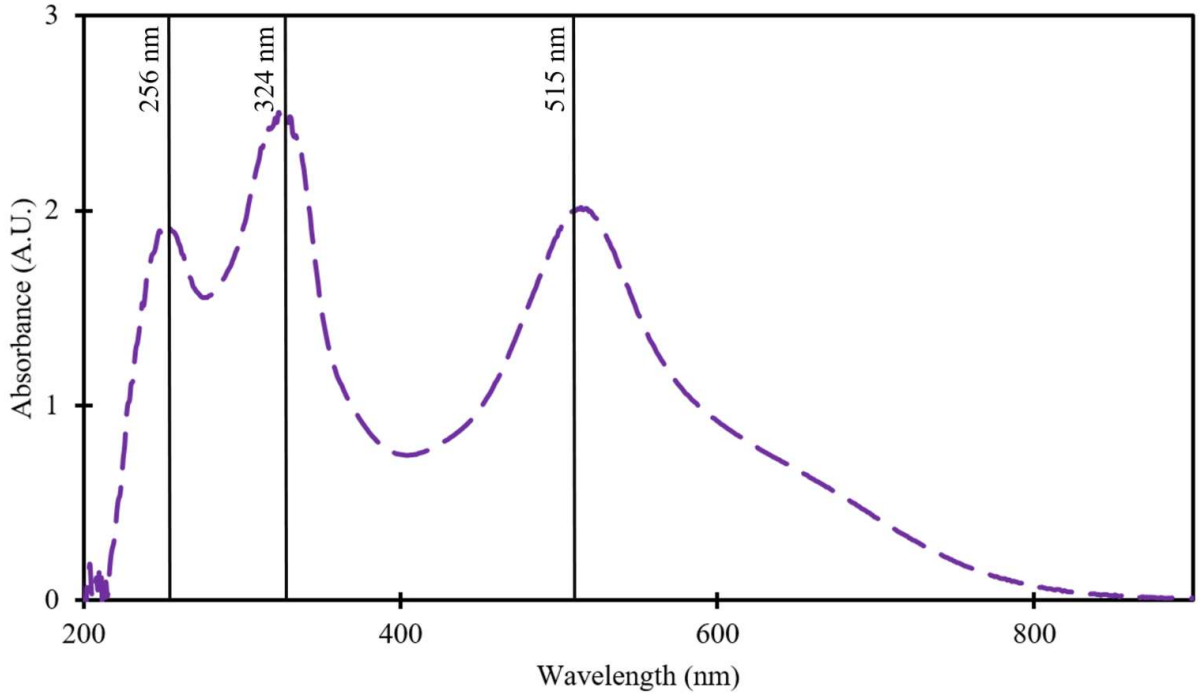

Figure 13: The UV-Vis spectrum of a 0.2 mM samples of DPPH· in methanol. The spectrum is measured in a Cary 60 UV-Vis spectrophotometer, between light wavelengths of 200 nm to 900 nm.

4.2.1 DPPH· Sample Preparation

A stock solution of 1.015 ± 0.003 mM DPPH· was prepared by dissolving 0.2003 ± 0.0005 g of 95 % purity DPPH· powder (Alfa Aesar, Canada) into 500.00 ± 0.20 mL HPLC grade methanol of 99.9 % purity (Biosolve Chimie SARL, The Netherlands). The solution was mixed using a stir bar for 30 minutes then stored between 0 °C and 8 °C. During mixing, storage, and transportation, light exposure to the DPPH· solution was limited by covering the containers in aluminium foil.

The DPPH· stock solution was degassed with N_2 (UHP, Air Liquide, Canada) for ≥ 4 hours. The solution was then transferred and stored in a glovebox cycled with UHP N_2 with O_2 and H_2O each maintained below 0.01 ppm. Preparation of experimental sample sets was completed in the glovebox. The preparation of these sample sets included the following:

i. Dilute the stock solution to a 50.00 ± 0.05 mL solution of 0.200 ± 0.001 mM DPPH·;
ii. Fill 2 mL polyethylene vials with the 0.200 ± 0.001 mM solution; and
iii. Seal each vial for irradiation.

Sample set preparation was repeated prior each experiment. Three separate sample sets were prepared:

i. Ten *Sample 1* vials were prepared 12 September 2024. These vials were irradiated for 10 minutes at inner site # 4.

ii. Ten *Sample 2* vials were prepared 26 September 2024. These vials were irradiated for 1-5 minutes at inner site # 4.
iii. Twelve *Sample 3* vials were prepared 01 October 2024. These vials were irradiated in either inner site # 4 for 1 minute or in the pool site for 31.4 minutes. This sample set had more replicates as the pool site sample holder had space for up to six vials simultaneously.

Prior to sample measurements, samples were mixed using a vortex mixer (Fisher Scientific, USA).

4.2.2 UV-Vis Calibration of DPPH

A Cary 60 UV-Vis spectrophotometer (Agilent, USA), with a light range of 190 nm to 1100 nm wavelengths, was used in this work. Figure 14 presents the absorbance of 515 nm light in DPPH· samples ranging from 0.030 ± 0.0001 mM to 0.230 ± 0.0006 mM. As expected, the measured 515 nm absorbance results were linear to the [DPPH·] in solution.

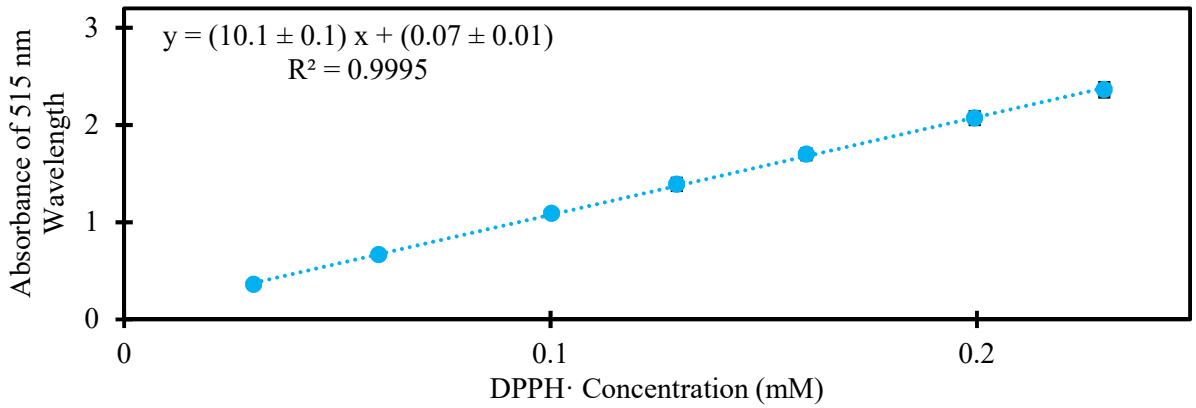

Figure 14: UV-Vis absorbance of 515 nm light by DPPH· in solutions of varying concentrations. The standard deviation between replicates is presented as the absorbance uncertainty, and ranges between ± 0.011 and ± 0.074. The concentration uncertainty ranges between ± 0.0001 mM and ± 0.0006 mM.

The coefficient of molar extinction was found to be 10,100 ± 100 $M^{-1} \cdot cm^{-1}$ (Figure 14). The Beer-Lambert Law (Equation f) describes the relationship between [DPPH·] and the absorbance of 515 nm light.

$$\varepsilon_{DPPH\cdot\ at\ 515\ nm} = \frac{Absorbance_{515\ nm}}{[DPPH\cdot] * 1\ cm} = (10100 \pm 100) M^{-1} \cdot cm^{-1} \qquad \textit{Equation f}$$

UV-Vis measurements are applied in concert with Equation f to calculate the [DPPH·] in experimental samples.

4.2.3 HPLC-MS/MS Analysis

An Agilent 1260 ultra-high performance liquid chromatograph (UHPLC) coupled to an Agilent 6460 Triple Quadrupole mass spectrometer (MS/MS) was used, and operated:

i. In negative electrospray ionization mode;
ii. Using a 50 mm x 2.1 mm x 3.0 µm ACME™ C18 analytical column paired with a guard column;
iii. Elution in an isocratic mode (80 % methanol in water mobile phase). Flow rate of 0.25 $\mu L \cdot min^{-1}$;
iv. With a sample run time exceeding the DPPH peak elution time by a factor of five, residuals are flushed from the analytical column; and

v. Using an external calibration curve ranging from 0.01 $\mu g \cdot L^{-1}$ to 2.00 $\mu g \cdot L^{-1}$. Samples of higher concentrations were diluted to within this range as necessary.

Additional conditions related to the MS detector are described in Table 6.

Table 6: HPLC-MS/MS conditions applied to DPPH measurements.

Parameter	Value*
Gas Temperature (°C)	325 ± 1
Gas Flow ($L \cdot m^{-1}$)	9.0 ± 0.1
Nebulizer (kPa)	276 ± 7
Sheath Gas (Nitrogen) (°C)	250 ± 1
Sheath Gas Flow ($L \cdot m^{-1}$)	8.0 ± 0.1
Nozzle Voltage (V)	3000 ± 10

**Uncertainties based institutional/operational experience [71].*

4.2.4 DPPH· Sample Irradiation

DPPH· samples were irradiated at inner site # 4 and the pool site within the RMC SLOWPOKE-2 reactor. These sites were chosen to investigate the impact of different radiation dose rates on DPPH molecular stability (*Section 3.3.2*). These different radiation dose rates are accounted for in the sample irradiation times chosen. Table 7 lists the DPPH sample irradiation times by site and absorbed dose.

Table 7: Experimental matrix for DPPH sample irradiation in the RMC SLOWPOKE-2 reactor irradiation sites

Irradiation Site	Irradiation Time (minutes)	Dose Absorbed (kGy)
Inner Site # 4	1.00 ± 0.02	0.78 ± 0.01
	2.00 ± 0.02	1.57 ± 0.01
	3.00 ± 0.02	2.35 ± 0.01
	4.00 ± 0.02	3.14 ± 0.01
	5.00 ± 0.02	3.92 ± 0.01
	10.00 ± 0.02	7.84 ± 0.01
Pool Site	31.4 ± 0.5	0.94 ± 0.02

When the RMC SLOWPOKE-2 reactor is operating at the nominal half power, the surrounding lab has radiation levels that are slightly above background. To limit the radiation received by control vials while experimental vials were within the reactor, control vials were kept in a lead container on the lab bench. The control vials therein were shielded from light and radiation by the lead.

The [DPPH·] in control samples was measured by UV-Vis immediately prior to irradiation. After irradiation, the control vials and irradiated vials were stored in separate lead containers until the radiation in all samples had decayed to safe levels. These lead containers protected the samples from light as well as protecting the lab from the radiation. Once samples could be safely manipulated and removed from the reactor laboratory (usually between three to four days, depending on the dose absorbed), they were analyzed by UV-Vis.

All vials (control and irradiated) are exposed to some light when handled prior to, during, and after experiments. Efforts are made to limit this exposure, but it was not realistic to eliminate it completely in the facilities available.

4.3 Results and Discussion

4.3.1 DPPH· Reduction in Control Samples

Measuring the DPPH· reduction observed in control vials establishes a reference/baseline amount of reduction in samples caused by any source other than irradiation. The UV-Vis spectra of control samples were measured at the beginning and end of each irradiation experiment. This section quantifies the DPPH· reduction in non-irradiated samples (*i.e.,* controls) caused primarily by light exposure. Results in this section are used in the subsequent sections to isolate the effects of radiation in irradiated DPPH· samples.

Figure 15 presents the UV-Vis spectra of DPPH· control samples (*i.e., t = 0*) versus various durations of lab light exposure (*i.e.,* $t_c = X$). The three absorbance peaks of DPPH· (*i.e.,* 256 nm, 324 nm, and 515 nm) are labeled. Considering the absorbance peaks from left to right, the 256 nm and 324 nm absorbance peaks do not change in intensity between the six spectra in Figure 15. This indicates that no changes to the DPPH molecular structure are observed in any samples, regardless of lab light exposure.

Continuing to the 515 nm peak, note the variation in absorbance between the three samples at *t = 0*. The samples prepared earlier have a slightly higher 515 nm peak than samples prepared later (preparation dates in *Section 4.2.1*), which suggests the stock solution is reduced slightly during storage.

Finally, observing the 515 nm absorbance peaks in the $t_c = X$ spectra. These peaks decrease (relative to the associated *t = 0* spectrum) as the duration of the lab light exposure increases; and highlight the requirement to limit lab light exposure while handling/storing samples during/between experiment and analysis.

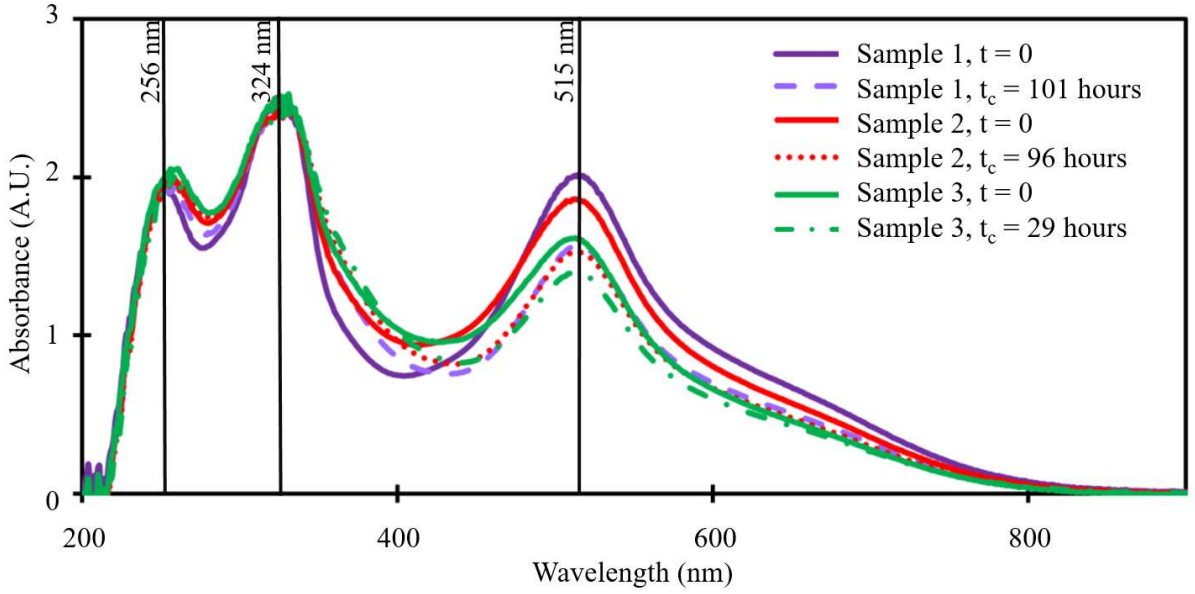

Figure 15: UV-Vis spectra of 0.200 mM ± 0.001 mM DPPH· control samples before and after experiments. Each control sample set is measured before and after experiments. These control samples were not irradiated, thus the observed spectra changes after t = X minutes are from light exposure during handling. Samples 1-3 ware all taken from the same DPPH· stock solution prepared on 11 September 2024. Sample 1 was prepared 12 September 2024, Sample 2 was prepared 26 September 2024, and Sample 3 was prepared 01 October 2024.

The concentration of DPPH· in the Figure 15 samples is done with Equation f. The results of these calculations are presented in Table 8. As the 256 nm and 324 nm absorbance peaks do not change across the six spectra, the change in the 515 nm peaks (and thus, the Δ [DPPH·]) indicates that the samples have been partially reduced to DPPH:H.

The decrease in the 515 nm absorbance intensity shows [DPPH·] decreases by 13 %, 18 %, and 22 % after 29, 96, and 101 hours of lab light exposure, respectively (Table 8).

Table 8: DPPH· concentration as a function of time exposed to lab light, calculated from UV-Vis results presented in Figure 15.

UV-Vis Measurement at $t = 0$			**UV-Vis Measurement at $t_c = X$**			**Δ [DPPH·] (mM)**
Sample Name	**515 nm Absorbance**	**[DPPH·] (mM)**	**Sample Name**	**515 nm Absorbance**	**[DPPH·] (mM)**	
Sample 1, $t = 0$	2.00±0.005	0.192±0.004	Sample 1, $t_c = 101$ *h*	1.57±0.005	0.149±0.004	0.043±0.008
Sample 2, $t = 0$	1.86±0.005	0.178±0.003	Sample 2, $t_c = 96$ *h*	1.52±0.005	0.144±0.004	0.033±0.007
Sample 3, $t = 0$	1.61±0.005	0.153±0.004	Sample 3, $t_c = 29$ *h*	1.40±0.005	0.132±0.003	0.021±0.007

To investigate the long-term effects of light exposure on DPPH· samples, additional DPPH· sample sets were prepared. Two identical sample sets were prepared from the stock solution and diluted to concentrations ranging from 0.05 to 50 ppb (± 10%). One sample set was shielded from light by wrapping the vials in aluminium foil and placing in a fridge. The second sample set was exposed to sunlight in a lab windowsill.

Each set[**] underwent HPLC-MS/MS analysis prior to the experiment, and again after 33 days of sun/darkness exposure. The results of HPLC-MS/MS analysis are listed in Table 9, and compare the samples kept in darkness to those exposed to sunlight. These results indicate that the samples kept in darkness experienced 0.01 ± 0.02 ppb of molecular degradation. Meanwhile, between to 0.02 ± 0.01 and 0.3 ± 0.2 ppb of molecular degradation is measured in samples exposed to sunlight for 33 days experience.

[**] Only the samples of 1 ppb of lower concentrations were analyzed by UHPLC-MS/MS, as higher concentrations could not be properly calibrated in the machine.

Table 9: Concentration of DPPH (DPPH· + DPPH:H) in samples exposed to darkness or light for 33 days. The concentration is measured in an HPLC-MS/MS, as per Section 4.2.3. The HPLC-MS/MS has a detection limit of 0.1 ppb. A conservative estimate of ± 10 % uncertainty is applied.

Original Concentration (ppb)	Samples Kept in Darkness		Samples Exposed to Light	
	Final Concentration (ppb)	Delta (ppb)	Final Concentration (ppb)	Delta (ppb)
0.050 ± 0.005	0.041 ± 0.005	0.01 ± 0.01	0.04 ± 0.005	0.02 ± 0.01
0.10 ± 0.01	0.087 ± 0.009	0.01 ± 0.02	0.07 ± 0.007	0.03 ± 0.02
0.50 ± 0.05	0.41 ± 0.04	0.09 ± 0.09	0.34 ± 0.03	0.16 ± 0.08
1.0 ± 0.1	1.0 ± 0.1	0.0 ± 0.2	0.73 ± 0.07	0.3 ± 0.2

Figure 16 shows the 50 ppb DPPH solutions kept in light to those in darkness for 33 days. The DPPH vial kept in darkness (on the left) is purple, characteristic of DPPH·. The DPPH vial exposed to sunlight in the windowsill (right), is yellow. The retention of the yellow colour suggests the picryl group from the DPPH molecule is still intact. As samples needed to be diluted to ≤ 50 ppb for HPLC-MS/MS operation, they were not concentrated enough to be analyzed by UV-Vis, as per the calibration curve in *Section 4.2.2*.

Figure 16: Picture of the 50 ppb ± 5 DPPH samples after being kept in darkness (left, purple) and light (right, yellow) for 33 days. These samples were too high in concentration to be analyzed by UHPLC-MS/MS, but were chosen for this image as the colours are most prominent due to the high concentration.

The HPLC-MS/MS analysis report in Figure 17 indicates the presence of a degradation product with a mass-to-charge ratio of 228 m/z, which suggests the presence of picric acid. The 228 $m \cdot z^{-1}$ peak is seen at approx. 0.5 minutes in the elution. This indicates that in the presence of UV radiation (sunlight) some DPPH is degrading to picric acid.

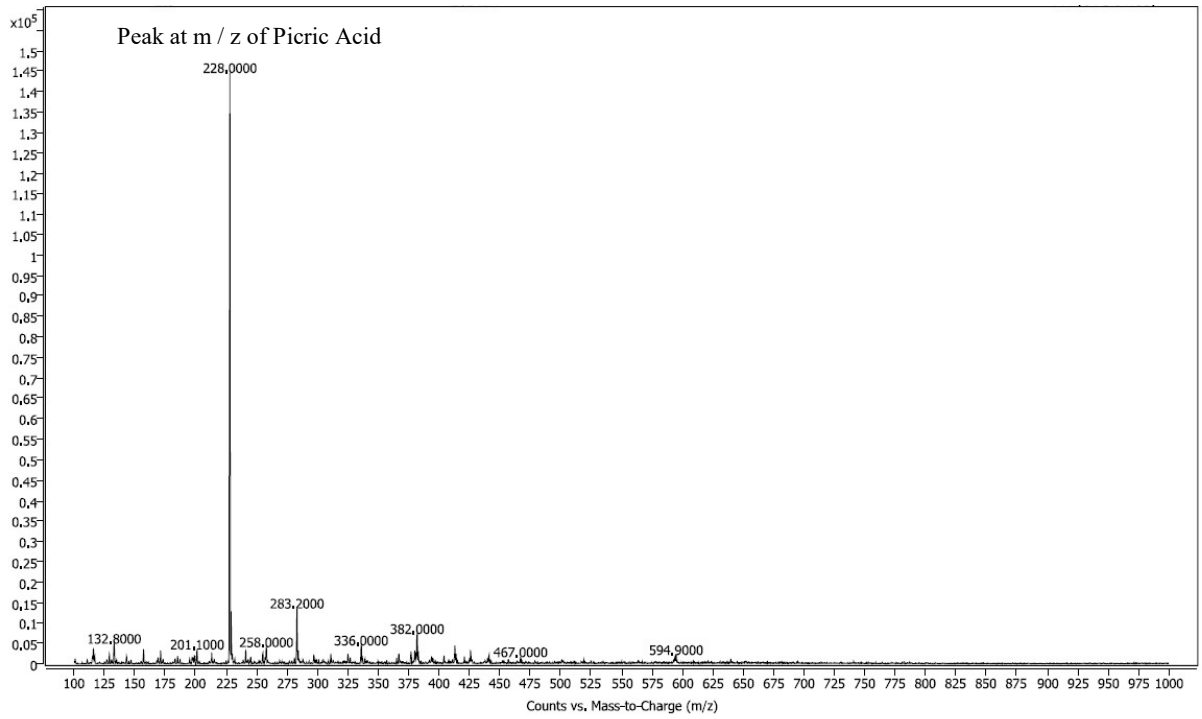

Figure 17: The HPLC-MS/MS report of the DPPH sample exposed to light for 33 days, representing the species identified at the 0.5 minutes elution time. The X-axis represents the mass to charge ratio of identified molecules, and the Y-axis represent the intensity of the identified molecules in the sample. A peak is discovered at a mass to charge ratio of 228, however it cannot be quantified as the intrument was only calibrated to quantify DPPH.

The DPPH molecule is susceptible to degradation from photons (UV irradiation), and thus the applicability of a DPPH assay in the RMC SLOWPOKE-2 reactor is uncertain. The survivability of the DPPH molecule in the photon and neutron radiation field of the reactor is investigated next via a series of short irradiations at the inner and pool sites.

4.3.2 DPPH· Irradiation Results

DPPH· samples were introduced to the irradiation sites of the reactor to assess the stability of the molecule after exposure to the radiation field. The survival of DPPH will determine whether a DPPH assay of the radiation field can be used to quantify the e^-_{solv} concentration in the irradiated solution.

[DPPH·] was measured by UV-Vis analysis before and after irradiation. The reduction of DPPH· to the hydrogenated form, DPPH:H, is stoichiometrically proportional to the concentration of electrons that bond to the molecule, as described in Reaction 11.

Irradiated and control samples were prepared and analyzed as outlined in *Section 4.2.1* and *Section 4.3.1*, respectively. The initial [DPPH] was measured at 0.175 ± 0.025 mM, as shown in the leftmost columns in Table 8. Irradiation conditions followed the experimental matrix presented in Table 7 (*Section 4.2.4*).

The UV-Vis spectra of irradiated DPPH· samples are shown in Figure 18. For comparison, the spectra of *Sample 1, t = 0* and *Sample 1, t_c = 101 hours*, originally presented in Figure 15 (*Section 4.3.*1) are included. These control spectra highlight the absorbance peaks characteristic of DPPH· at 256 nm, 324 nm, and 515 nm, with the *Sample 1, t_c = 101 hours* spectrum providing a reference for the reduction caused by light. Comparing these spectra to irradiated spectra enables differentiation between light and radiation induced changes.

In the spectra of irradiated samples (t_{irr} = *1 minute* to t_{irr} = *31 minutes, Pool Site* in Figure 18) the 515 nm absorbance peak characteristic of the radical DPPH· is absent, suggesting the radical has been either reduced or degraded. Additionally, no distinct absorbance features are observed at the 256 nm or 324 nm, indicating that neither DPPH· nor DPPH:H are present in the irradiated solution.

The UV-Vis spectrum of the *t=1 minute* sample (a maroon curve in Figure 18) does not exhibit discrete peaks in the UV-Vis range, and appears intermediate between the initial spectrum of DPPH· and that of picric acid. This suggests a transitional composition is present after one minute of irradiation.

Samples irradiated for between 2 and 31 minutes (the remaining curves in Figure 18) display absorbance peaks at 245 nm, 290 nm, 364 nm, and 420 nm. Such features are not present in the control spectra, but are characteristic of picric acid [72]. These results support the hypothesis that DPPH· degrades to picric acid under the mixed irradiation from the RMC SLOWPOKE-2, as illustrated in Figure 19.

The intensity of these absorbance peaks vary with dose absorbed (see Table 7). The 245 nm and 290 nm peaks increase with dose, whereas the 364 nm and 420 nm peaks decrease. Notably, the spectrum of the sample irradiated for 10 minutes (7.84 ± 0.01 kGy, the dark blue curve in Figure 18) is most consistent with that of picric acid [72]. This suggests that the spectra of samples that absorbed lower doses represent intermediate stages of DPPH· degradation to picric acid.

Notably, the t_{irr} = *1 minute* and t_{irr} = *31 minutes, Pool site* samples absorbed comparable doses (0.78 ± 0.01 kGy and 0.94 ± 0.02 kGy, respectively), despite a substantial difference in irradiation durations (1.00 ± 0.02 minutes vs. 31.4 ± 0.5 minutes; see Table 7). As discussed in *Chapter 3.* MCNP Simulation Activities, the disparity between doses and durations is caused by the different radiation fields at inner site # 4 and the pool site. Compared to the pool site, inner site # 4 has:

i. A total dose rate > 20x higher;
ii. A neutron dose rate > 300x higher; and
iii. A neutron to photon dose rate ratio ~8x higher.

The observed differences between the UV-Vis spectra of the t_{irr} = *1 minute* and t_{irr} = *31 minutes, Pool site* samples may be attributed to either of these site related differences or to dose/time-dependant degradation factors. Further investigation is required to confirm the contributing factors.

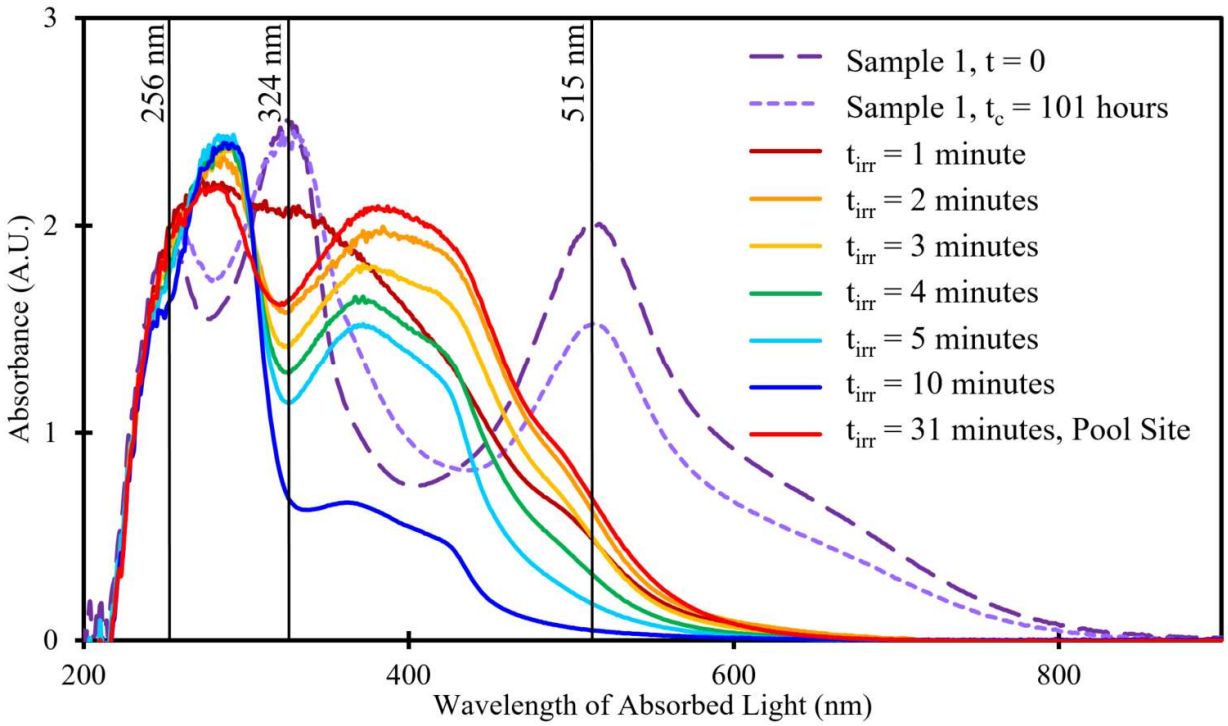

Figure 18: UV-Vis spectra of irradiated (solid traces) and control (dotted traces) DPPH samples. Samples were irradiated at inner site # 4 for between 1 and 10 minutes and the pool site for 31.4 minutes.

The molecular structures of DPPH· and picric acid are presented in Figure 19. DPPH· has a picryl group bonded to the radical nitrogen of the molecule, while picric acid has a hydroxide bonded to the ipso carbon of a picryl group. During irradiation, radiolytically produced hydroxyl radicals may attack DPPH· at the ipso carbon of the picryl group, leading to cleavage of the picryl group from DPPH· and the subsequent formation of picric acid. While this serves to demonstrate a possible reaction from DPPH· to picric acid, further research is required to confirm the reaction that occurs during such experiments.

The remaining two benzene rings from the original DPPH· molecule, or the nitrogen atoms, cannot be observed using the Cary 60 UV-Vis spectrophotometer [73,74]. Therefore, no comments can be made regarding the state of degradation products (other than picric acid) in this thesis. Future research is required to investigate the degradation reaction observed in this thesis.

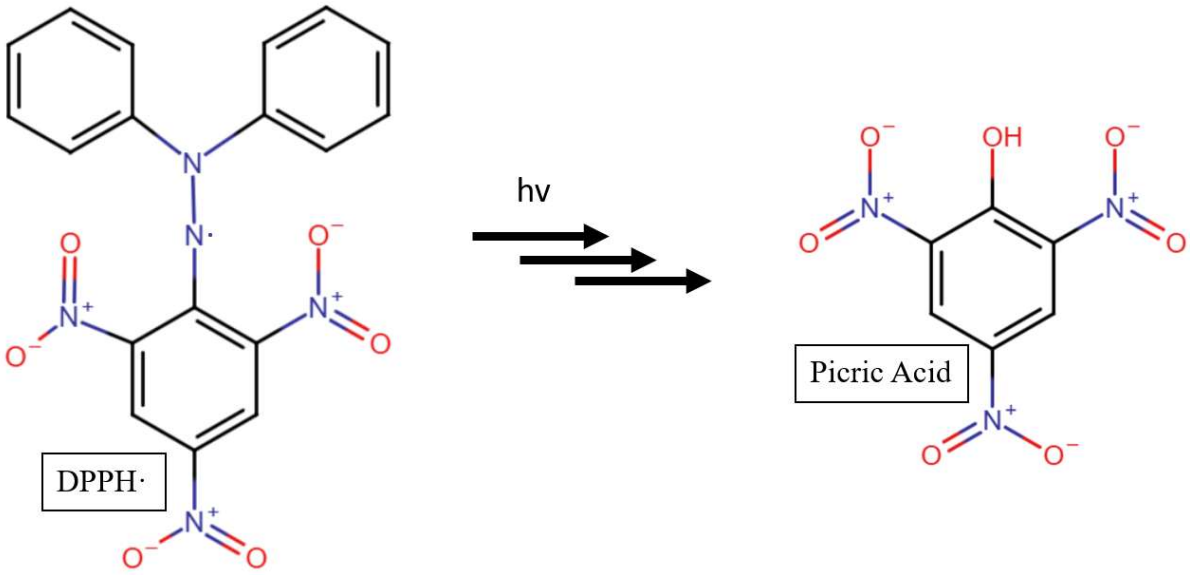

Figure 19: Pictogram of DPPH degradation in methanol during SLOWPOKE-2 irradiation experiments. Images created using the Chemical Sketch Tool from the Research Collaboratory for Structural Bioinformatics and Marvin JS by Chemaxon [41,42].

When exposed to ionizing radiation DPPH· samples degrade to picric acid, as confirmed by both HPLC-MS/MS analysis of samples exposed to solar radiation and UV-Vis analysis of samples exposed to nuclear radiation. Due to this degradation, the concentration of DPPH· reduced to DPPH:H cannot be measured with certainty. Thus, a DPPH assay is not a viable method to quantify the e^-_{solv} yield in RMC SLOWPOKE-2 irradiated samples.

4.4 DPPH· Conclusions

The results of this chapter found a presence of picric acid in SLOWPOKE-2 irradiated DPPH samples that confirms a DPPH assay cannot be reliably applied to measure the e^-_{solv} yield within the SLOWPOKE-2 at nominal half power (10 kW_{th}).

Reaching this conclusion accomplishes *Thesis Goal #2*: namely, to *investigate the viability of quantifying e^-_{solv} yields with DPPH· in the mixed field radiation environments of the RMC SLOWPOKE 2 irradiation sites*.

The quantification of the e^-_{solv} yield in RMC SLOWPOKE-2 irradiated samples required experimental validation, which cannot be done with a DPPH· assay during nominal half power operations. Future research is recommended in the following areas:

i. Investigate if a DPPH· assay is viable at a lower reactor power setting; and
ii. Investigate other e^-_{solv} yield quantification methods in the RMC SLOWPOKE-2 reactor.

Chapter 5. PFOA Irradiation Activities

5.1 Introduction

The mixed radiation fields emanating from the RMC SLOWPOKE-2 reactor core can provide unique redox environments in which to study PFAS degradation. PFAS degradation has been studied previously in the RMC SLOWPOKE-2 reactor by Rook in 2018 [20], but was limited to the inner irradiation sites and did not optimize for e^-_{solv} yield in samples.

This work studies the degradation of PFOA in environments with varying e^-_{solv} production. Specifically, the e^-_{solv} production effect on PFOA degradation is investigated in two experiments. First, minimizing the DO content in the samples (*Section 2.1.1*) during irradiation. Second, comparing the degradation in the different mixed irradiation fields (*i.e.,* degradation caused by e^-_{solv} produced by varying neutron to photon ratios found within the inner, outer, and pool irradiation sites). Finally, degradation mechanisms are discussed.

This chapter achieves *Thesis Goal #3*, namely, to *investigate the effects of varying e^-_{solv} yields from SLOWPOKE-2 irradiation on PFOA degradation.*

5.2 Methodology

5.2.1 Sample Preparation and Irradiation

A 120 ppb stock solution was made by dissolving PFOA (98 % purity; SynQuest Labs, product # 2121-3-18) in ultrapure water (resistance 18.2 MΩ·cm) retrieved from a UV Synergy water purification system (Merck Millipore, Germany) [75].

The PFOA stock solution was degassed with N_2 (UHP, Air Liquide, Canada) for ≥ 4 hours until the DO content was less than 0.4 % (0.3 $mg \cdot L^{-1}$, measured at 25°C) as measured with a ProDSS Optical DO probe, connected to a YSI Pro Digital Sampling System. The solution was then transferred, prepared, and stored in a glovebox cycled with UHP N_2 with O_2 and H_2O each maintained below 0.01 ppm. Irradiation preparation involved placing 1 mL aliquots of the stock solution (C_0 = 120 ppb) in 1.5 mL HDPE vials (LAContainer, USA), which were sealed and subsequently encapsulated within 7 mL HDPE vials (LAContainer, USA).

PFOA samples were irradiated in the RMC SLOWPOKE-2 reactor at nominal half power (*i.e.,* 10 kW_{th}). Samples were irradiated at inner site #4, outer site #10, and at the pool site (~ 7 cm from the exterior of the reactor container). Figure 5 Figure 6 (*Section 2.4.2*) help illustrate the location of these sites within the reactor. Table 10 lists the dose received in each irradiation site as a function of irradiation time. The irradiation times were selected to expose sample to comparable total absorbed dose despite the differing neutron and photon dose rates and ratios (Figure 11 in *Section 3.3.2*) within each site.

Table 10: Experimental matrix for PFOA sample irradiation in the RMC SLOWPOKE-2 inner, outer, and pool irradiation sites. Values for the doses and uncertainties are calculated from MCNP6.3 simulation results in Chapter 3.

Inner Site # 4		Outer Site # 10		Pool site	
Time (minutes)	**Dose Absorbed (kGy)**	**Time (minutes)**	**Dose Absorbed (kGy)**	**Time (minutes)**	**Dose Absorbed (kGy)**
1.00 ± 0.03	0.75 ± 0.02	5.10 ± 0.03	0.836 ± 0.003	31.4 ± 0.5	0.94 ± 0.01
2.00 ± 0.03	1.49 ± 0.02	10.20 ± 0.03	1.672 ± 0.003	62.8 ± 0.5	1.88 ± 0.01
5.00 ± 0.03	3.73 ± 0.02	25.60 ± 0.03	4.196 ± 0.003	157.0 ± 0.5	4.70 ± 0.01
10.00 ± 0.03	7.46 ± 0.02	51.20 ± 0.03	8.392 ± 0.003	314.0 ± 0.5	9.41 ± 0.01
20.00 ± 0.03	14.91 ± 0.02	102.30 ± 0.03	16.768 ± 0.003	471.0 ± 0.5	14.11 ± 0.01
60.00 ± 0.03	44.74 ± 0.02	306.90 ± 0.03	50.309 ± 0.003		
80.00 ± 0.03	59.66 ± 0.02	409.20 ± 0.03	67.072 ± 0.003		
120.00 ± 0.03	89.49 ± 0.02				

N.B., Higher absorbed dose exposures within the outer and pool sites were not possible given reactor availability and the lower dose rates at these sites.

5.2.2 PFOA HPLC-MS/MS Analysis

An Agilent 1260 ultra-high performance liquid chromatograph (UHPLC) coupled to an Agilent 6460 Triple Quadrupole mass spectrometer (MS/MS) [73] was used to analyzed PFOA samples with the following settings/modes, accessories, and procedures:

i. Negative electrospray ionization mode,
ii. A 50 mm x 2.1 mm x 3.0 µm ACME C18 analytical column paired with a guard column,
iii. Mobile phases consisted of 0.1 % acetic acid in deionized water (A) and acetonitrile (B),
iv. The elution profile started at 90 % A / 10% B, transitioning to 10% A/ 90% B, holding for 4 minutes, then equilibrating at starting conditions for 3 minutes, using a flow rate of 0.4 $\mu L \cdot min^{-1}$,
v. PFOA was quantified with an external calibration curve (PFAC-MXH from Wellington Labs, Guelph, ON) ranging from 0.1 to 25 ppb in a MeOH : H_2O solution; and
vi. Detection limits were set to the lowest concentration of each calibration curve, 0.09 ppb.

Additional conditions related to the MS detector are described in Table 11.

Table 11: HPLC-MS/MS conditions applied to PFOA measurements.

Parameter	Value
Gas Temperature (°C)	325 ± 1
Gas Flow ($L \cdot m^{-1}$)	9.0 ± 0.1
Nebulizer (kPa)	276 ± 7
Sheath Gas (Nitrogen) (°C)	250 ± 1
Sheath Gas Flow ($L \cdot m^{-1}$)	8.0 ± 0.1
Nozzle Voltage (V)	3000 ± 10

5.3 Results and Discussion

5.3.1 The Dissolved Oxygen Content Effect

The impact of the DO content in PFOA solutions on the degradation observed is investigated. In Figure 20, where C_f/C_0 represents the Δ [PFOA] between irradiated and control samples, experimental results (0.4% DO) are compared to results from Rook (2018) (50% and 100% DO). All samples compared in Figure 20 are irradiated at inner site # 4 of reactor, operating at nominal half power (10 kW_{th}) for between 1 to 120 minutes. Samples irradiated in this thesis have a significantly lower DO content than samples

presented in Rook (2018) [1], whilst maintaining the same dose rate, the ratio of neutron to photon, and irradiation time.

Samples irradiated for periods less than 5 minutes show limited PFOA degradation, which suggests there is a minimum required absorbed dose (producing a correlated e^-_{solv} concentration) or that there has been insufficient time to initiate PFOA degradation. However, further research is required to confirm this observation and/or to determine causation.

For samples irradiated for 10 minutes or longer, there is a clear trend of greater PFOA degradation in the 0.4 % DO samples than in the samples with higher DO content. After 120 minutes of irradiation, the 0.4 % DO PFOA samples had experienced an average of 13.9 ± 0.4 % degradation; whilst results from the 100 % DO samples experienced only 9.7 ± 0.7 % PFOA degradation, Rook (2018) [20]. Minimizing the DO content in irradiated samples increased PFOA degradation by approximately 40 %; confirming the degradation dependence on DO content.

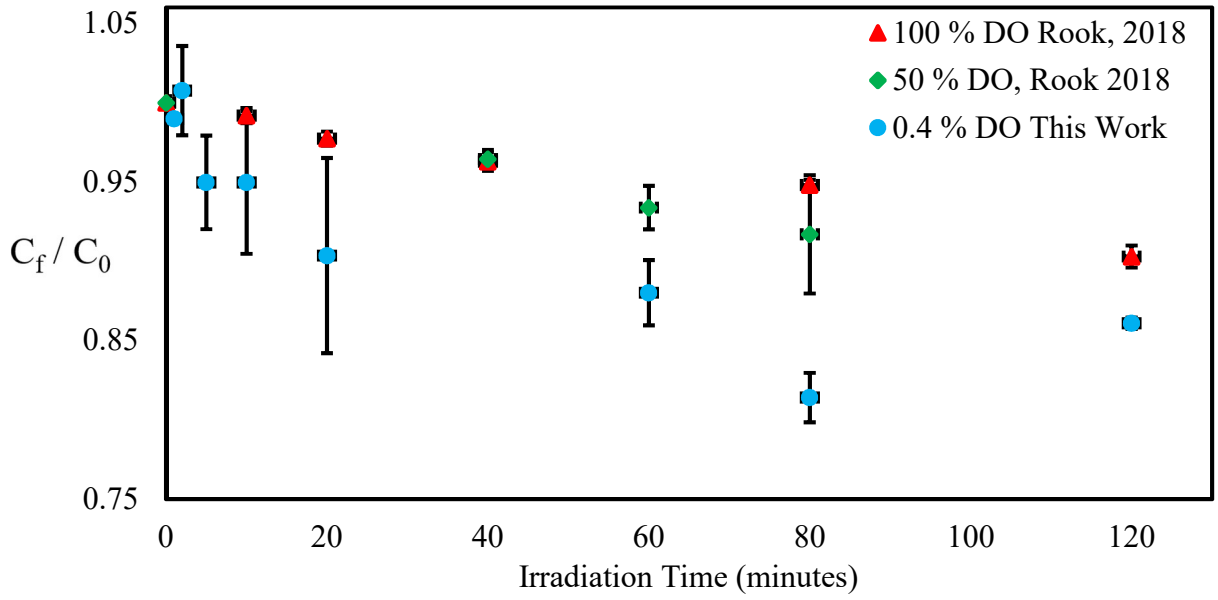

Figure 20: PFOA irradiation results from solutions with 0.4 % DO (This work) and results from Rook (2018) [20] from irradiated PFOA solutions with 100 % DO, 50 % DO. At 5 minutes, only a 0.4 % DO sample exists. At 40 minutes, no 0.4% DO sample exists, at 60 minutes, no 100% DO sample exists, and at 120 minutes, no 50% sample exists.

The increase in PFOA degradation in low DO optimized samples (0.4%) compared to samples with higher DO (50% or 100%) indicates that DO may hinder PFOA degradation during irradiation. DO is an e^-_{solv} scavenger (*Section 2.1.1*), thus its removal from the samples enables more e^-_{solv} interaction with PFOA. This finding aligns with results from Patch *et al.* (2022) [22] and O'Connor *et al.* (2023) [26], confirming e^-_{solv} are key to PFOA degradation.

Additional irradiations in the inner, outer, and pool irradiation sites of the RMC SLOWPOKE-2 reactor investigate the impact of e^-_{solv} production rate on degradation. These sites experience different rates of neutron, photon, and electron radiation, which in turn produce different rates of e^-_{solv} in the samples (*Section 2.3 and 3.3.2*). Thus, the following section will investigate the effects of these differences on PFOA degradation.

5.3.2 Investigating Varying e^-_{solv} Production on PFOA Degradation

During irradiation of the samples in the RMC SLOWPOKE-2, water radiolysis incited by photon radiation is responsible for the majority of the e^-_{solv} production (*Section 3.4.3*) as compared to the e^-_{solv} production from neutron and electron radiation. The contributions of neutrons, photons, and electrons to the total dose are listed by irradiation site in Figure 11 (*Section 3.3.2*) and the theoretical e^-_{solv} concentration, or $[e^-_{solv}]$, production rates for each site are listed in Table 5. These $[e^-_{solv}]$ values, seen along the *x*-axis of the figures in this section, were calculated by combining these dose rates (which are resultant from irradiation durations, sites location, and reactor power) with the *g*-values from Elliot and Bartels (2009) [55][††].

Figure 21 compares PFOA degradation (C_f /C_0 represents Δ [PFOA], referred to as degradation) to the $[e^-_{solv}]$ produced in solution. *N.B.,* all $[e^-_{solv}]$ production values and [PFOA] from each irradiation site are combined into one dataset, as results show minimal variation in PFOA degradation trends across: (i) neutron-to-photon dose ratio, (ii) total dose rate, and (iii) irradiation time. Rather, PFOA degradation generally increases with exposure to higher e^-_{solv} concentrations (as calculated in MCNP6.3). The full dataset can be found in Appendix D Irradiated PFOA Dataset.

The greatest amount of [PFOA] change (-10 ± 5 %) is observed after a 0.010 ± 0.005 mM e^-_{solv} exposure. In samples exposed to higher $[e^-_{solv}]$, the degradation trend begins to plateau (*i.e.* samples exposed to 0.020 ± 0.005 mM of e^-_{solv} experience only degraded by -13 ± 5 %, and by -14.12 ± 0.04 % for 0.040 ± 0.005 mM exposures, shown in Figure 21 as black Δ lines). This degradation plateau suggests the e^-_{solv} necessary for further PFOA degradation may be consumed by some parasitic species.

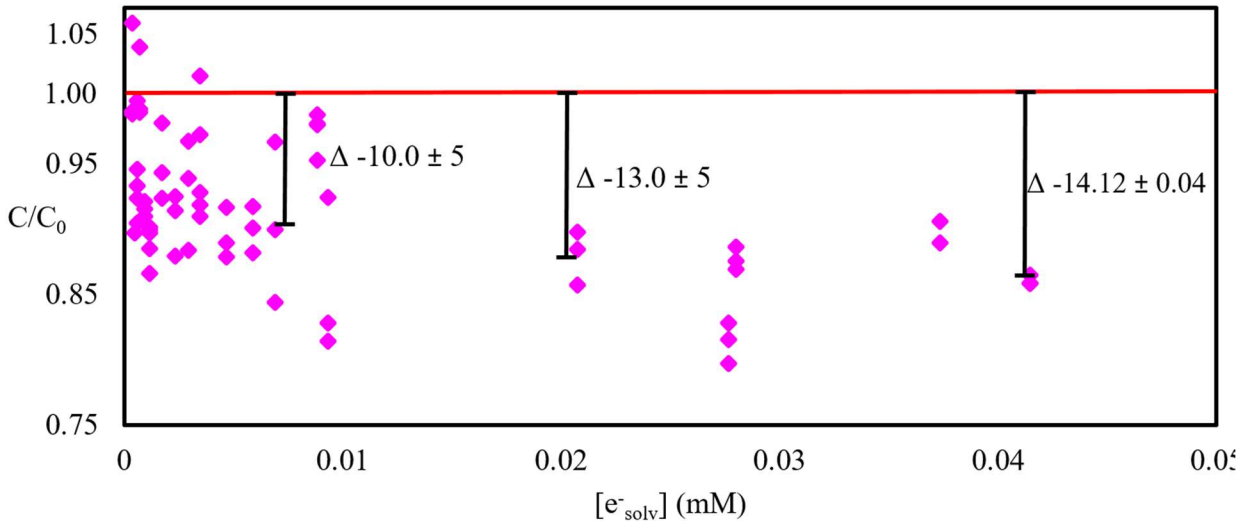

Figure 21: PFOA degradation in samples irradiated in the RMC SLOWPOKE-2 plotted against the theoretical e^-_{solv} yield calculated for each sample.

Patch *et al.* (2022) [22] proposed several degradation mechanisms, identifying possible products that could parasitically reduce the e^-_{solv} population (*Section 2.1.1*). The initial PFOA molecule is an eight-carbon (C8) perfluorocarboxylic acid (PFCA), and during irradiation several mechanisms degrade PFOA concurrently. Of these mechanisms are paths that degrade C8 into a shorter carbon-chain PFCA (*i.e.,* perfluoroheptanoic

[††] A discussion on the application of *g*-values for this work is found at the end of this section.

acid (PFHpA, C7), then to perfluorohexanoic acid (PFHxA, C6)). As shown in Figure 2 (*Section 2.1.1*), multiple pathways exist to shorten the carbon-chains of these PFCA, each consuming e^-_{solv}. Furthermore, previous work by Rook (2018) [20] suggests that the C7 and C6 species consume e^-_{solv} more efficiently than C8 species (see *Section 2.4.3*). The combined effect of these e^-_{solv} sinks decreases the likelihood that the e^-_{solv} population could effectively degrade the original C8 PFOA species as more short-chain products are formed.

To investigate the cause of the degradation plateau seen in Figure 21, the appearance of the C7 and C6 species in irradiated samples was investigated by HPLC-MS/MS analysis, results in Figure 22. These results confirm the appearance and concentration growth of C7 and C6 species as PFOA (C8) degrades. Specifically, [PFOA] (C8) degrades from 120.00 to 102.72 ± 0.05 ppb whereas [PFHpA] (C7) and [PFHxA] (C6) grow. The [PFHpA] increases from 0.16 ± 0.05 ppb to 1.71 ± 0.05 ppb and [PFHxA] increases from the 0.09 ppb detection limit to 0.34 ± 0.05 ppb after exposures to 0.040 ± 0.005 mM e^-_{solv}. The slowing of C8 degradation, along with the presence and growth of C7 and C6 populations, suggests these shorter carbon-chained species may negatively affect the e^-_{solv} population. A reduced e^-_{solv} population likely limits PFOA (C8) degradation, leading to the observed plateau.

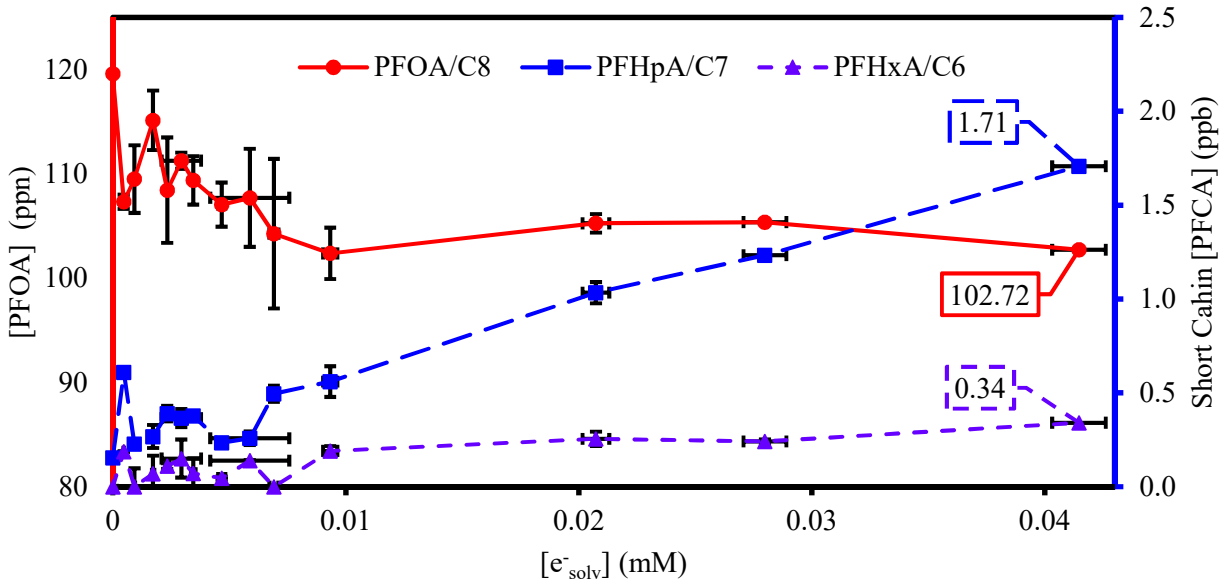

Figure 22: PFOA degradation results compared to the rise of shorter-chain PFCAs, as a function of e^-_{solv} exposure during irradiation. The short-chain PFCAs reported are PFHpA (C7) and PFHxA (C6). The [PFOA] is shown on the left side y-axis, and the [PFHpA] and [PFHxA] are on the right side y-axis, due to the differences in magnitudes.

To investigate the e^-_{solv} scavenging abilities of the C7 and C6 species, results from Rook (2018) [20] are reviewed (*Section 2.4.3*). Rook (2018) [20] reports PFOA saw near zero degradation when irradiated in mixed solutions with shorter PFCAs. In contrast, approximately 8% degradation was measured when PFOA was irradiated in isolation under identical conditions. Because C7 and C6 experience preferential degradation by e^-_{solv} [20], their production scavenges e^-_{solv}, hindering further PFOA (C8) degradation and resulting in the observed the plateau. The stark difference in PFOA degradation between these two experiments from Rook (2018) explains the plateau observed in Figure 21; in solutions of mixed length PFCAs, shorter PFCAs outcompete PFOA for e^-_{solv}, hindering PFOA degradation despite further e^-_{solv} production.

The incomplete mass balance is shown in Equation g. PFCAs of carbon lengths shorter than C5 were below detection limits and thus not measured. The UHPLC-MS/MS analysis was calibrated for the PFCAs, and therefore partially defluorinated degradation products were not measured either. Furthermore, fluorine recovery was not measured due to the low initial concentration of PFOA. Identifying and quantifying these degradation products should be investigated in future work, where larger initial concentrations combined with broader UHPLC-MS/MS analysis can assist in these efforts, as these were outside the scope of this thesis.

$$[C8]_0 = [C8]_f + [C7]_f + [C6]_f + \sum[C \geq 5\ PFCA] + \sum[Partially\ Defluorinated\ PFASs] \quad \textit{Equation g}$$

Importantly, the quantities of e^-_{solv} discussed in this section (the *x*-axis of Figure 21 Figure 22) must be considered with the caveat that the *g*-values are estimations. Applying *g*-values to determine the steady state availability of these radical particles requires an understanding of *g*-values derivation. *Section 2.3* explains in detail how a *g*-value defines the primary radiolysis yields within radiation spurs after approximately 100 ns of irradiation. As a result, quantities of e^-_{solv} derived using *g*-values yields an initial over-estimation and does not account for the complex and e^-_{solv} scavenging reactions in the mixed solution during irradiation.

The plateau in PFOA degradation found in this thesis demonstrates that once sufficient PFOA has degraded to C7 and C6 PFCAs, these products act as e^-_{solv} scavengers, hindering further PFOA degradation (observed as the plateau in Figure 21 Figure 22). While it is possible that the entirety of the PFCAs (including PFOA) in the solution could be degraded completely by SLOWPOKE-2 irradiation, the required e^-_{solv} exposure would be significantly larger, requiring either higher reactor power settings, longer irradiations, or both. Such feats were not feasible in this thesis due to reactor constraints.

5.4 PFOA Conclusions

The results in this chapter demonstrate that increasing the production of e^-_{solv} is key to the degrading PFOA during irradiation. PFOA degradation increases by approximately 40% when the DO content (a large source of e^-_{solv} scavenging) is limited to 0.4 %. However, the degradation plateaus after exposure to 0.02 ± 0.005 mM e^-_{solv} due to the production of shorter-chain PFCAs. These products experience preferential degradation by the limited $[e^-_{solv}]$, acting as e^-_{solv} scavengers and inhibit further PFOA degradation. This source of scavenging limits the amount of PFOA degradation that is observed in the short irradiations (< 12 hours) possible in this thesis. The evidence of PFCA chain shortening adds credence to e^-_{solv} being the key reactive species for PFOA/PFAS degradation.

It is possible that with much longer irradiations (t >> 24 hours), sufficient $[e^-_{solv}]$ could degrade all C7 and C6, allowing for further C8 degradation. In extremely long irradiations, potentially at higher reactor power, a cycle of i) PFOA degradation, ii) short chain PFCA formation, iii) short chain PFCA degradation, followed by iv) further PFOA degradation. Such a cycle could lead to the complete destruction of all PFCAs in the sample. Very long irradiation experiments should investigate this possibility, seeking to enable low-cost PFOA destruction through irradiations concurrent to other research/power generation.

Chapter 6. Conclusions and Recommendations

The overall objective of this work was to investigate the degradation of PFOA in samples irradiated in the RMC SLOWPOKE-2 reactor. This objective lead to the establishment of three research goals in separate areas of study. The conclusions from each area of study and recommendations for future work are listed individually in this chapter.

Thesis Goal #1: Apply MCNP6.3 software to predict the yield of e^-_{solv} in samples *irradiated in the RMC SLOWPOKE-2.*

The electron transport capabilities of MCNP6.3 were applied to directly simulate the e^-_{solv} yield. However, this work concluded that these features were insufficient to predicting the e^-_{solv} yield in irradiated samples, as they were incapable of simulating the following:

i. Simulating e^- from all radiolysis reactions that produce e^-_{solv},
ii. Transporting radiolytically produced e^- through complex solvation mechanisms to e^-_{solv}; or
iii. Simulating e^- across certain geometries in the RMC SLOWPOKE-2 MCNP6.3 model.

The RMC SLOWPOKE-2 MCNP6.3 model was therefore used to simulate dose rates for neutron, photon, and electron radiation at the irradiation sites. The e^-_{solv} yield was then calculated by multiplying these simulated dose rates with published *g*-values from the literature. The MCNP6.3 modelling in this thesis resulted in the novel prediction of neutron and photon radiation dose rates from both fission and secondary nuclear reactions, as well as calculated e^-_{solv} yields in irradiation sites across the RMC SLOWPOKE-2 nuclear research reactor.

Future research is recommended to apply dedicated radiolysis modelling software to simulate the e^-_{solv} yield in the RMC SLOWPOKE-2 irradiation sites, using the dose rate information published herein. Furthermore, experimental techniques to measure the neutron, photon, and electron dose rates present in each irradiation site of the RMC SLOWPOKE-2 reactor could be investigated and applied to validate the simulated dose rates presented in this thesis.

Thesis Goal #2 Investigate the viability of quantifying e^-_{solv} yields *with DPPH· in the mixed field radiation environments of the RMC SLOWPOKE-2 irradiation sites.*

Irradiation of DPPH· samples in the inner and pool irradiation sites of the RMC SLOWPOKE-2 reactor aimed to determine the reliability of a DPPH· assay. However, UV-Vis and HPLC-MS/MS analysis confirmed the presence of picric acid in irradiated samples, suggesting DPPH· degraded to picric. Therefore, this thesis concluded that DPPH· cannot be reliably applied to quantify the e^-_{solv} yield in the irradiation sites of the RMC SLOWPOKE-2 nuclear research reactor whilst operating at nominal half power.

Future research should investigate the viability of a DPPH· assay in the reactor irradiation sites during operation at lower power settings or investigate other methods of e^-_{solv} yield quantification.

Thesis Goal #3 Investigate the effects of varying e^-_{solv} yields from RMC SLOWPOKE-2 irradiation on PFOA degradation.

Experimental results found that limiting the DO content in irradiated solutions from 100% to 0.4% increased PFOA degradation by approximately 40%. This is because DO acts as a e^-_{solv} scavenger, reducing the number of e^-_{solv} available to degrade PFOA.

Further experiments compare PFOA degradation based on the irradiation site used. The inner, outer, and pool sites have different neutron, photon, and electron dose rates that contribute uniquely to the e^-_{solv}

production in the sample. Additionally, the total doses vary greatly between these sites, allowing PFOA degradation to be compared by this metric as well. The results of these experiments concluded that the dependence of PFOA degradation in the RMC SLOWPOKE-2 reactor is attributed to the e^-_{solv} yield rather than any difference in radiation field composition (neutron/photon/electron), total dose rate, or duration of the irradiation.

Also, experimental results determined that PFOA degraded, in part, to shorter-chain PFCAs such as PFHpA and PFHxA. These degradation products were deemed e^-_{solv} scavengers, whose production led to a plateau in PFOA degradation.

Future experiments involving PFAS and the RMC SLOWPOKE-2 should endeavor to expose highly concentrated samples of PFOA to extremely large concentrations of e^-_{solv} through high-powered, long duration irradiations. Such research should prioritize the following:

i. Higher initial concentrations of PFOA should be used to enable the detection of other degradation products; and
ii. Irradiation experiments of several days to months should be tested in a batch process, to identify the required durations for the full destruction of all PFAS molecules and their degradation products.

Such experiments could provide insights into:

i. A thorough list of degradation products, allowing for the completion of a mass balance, and insights into the reaction rate orders and constants of the competing reactions; and
ii. The possibility of using nuclear power technology as a tool for the elimination of harmful chemicals at low costs.

This thesis simulated dose rates at different RMC SLOWPOKE-2 sites to calculate e^-_{solv} concentrations. Although quantifying e^-_{solv} with DPPH was unsuccessful, tandem irradiation of PFOA confirms e^-_{solv} as the main reactive species for degradation. The study clarifies e^-_{solv}'s role in PFOA degradation and offers preliminary observations for large-scale remediation using commercial reactors.

References

1. Moody C, Field J. Perfluorinated surfactants and the environmental implications of their use in fire-fighting foams. Environmental Science & Technology. 2000 Aug 12;34. doi:10.1021/es991359u

2. Herzke D, Olsson E, Posner S. Perfluoroalkyl and polyfluoroalkyl substances (PFASs) in consumer products in Norway – A pilot study. Chemosphere. 2012 Aug 1;88(8):980–7. doi:10.1016/j.chemosphere.2012.03.035

3. Zafeiraki E, Costopoulou D, Vassiliadou I, Bakeas E, Leondiadis L. Determination of perfluorinated compounds (PFCs) in various foodstuff packaging materials used in the Greek market. Chemosphere. 2014 Jan 1;94:169–76. doi:10.1016/j.chemosphere.2013.09.092

4. Liu X, Guo Z, Krebs KA, Pope RH, Roache NF. Concentrations and trends of perfluorinated chemicals in potential indoor sources from 2007 through 2011 in the US. Chemosphere. 2014 Mar 1;98:51–7. doi:10.1016/j.chemosphere.2013.10.001

5. Schultes L, Vestergren R, Volkova K, Westberg E, Jacobson T, Benskin JP. Per- and polyfluoroalkyl substances and fluorine mass balance in cosmetic products from the Swedish market: implications for environmental emissions and human exposure. Environmental Science: Processes & Impacts. 2018 Dec 12;20(12):1680–90. doi:10.1039/C8EM00368H

6. Hu XC, Andrews DQ, Lindstrom AB, Bruton TA, Schaider LA, Grandjean P, Lohmann R, Carignan CC, Blum A, Balan SA, Higgins CP, Sunderland EM. Detection of poly- and perfluoroalkyl substances (PFASs) in U.S. drinking water linked to industrial sites, military fire training areas, and wastewater treatment plants. Environmental Science & Technology Letters. 2016 Oct 11;3(10):344–50. doi:10.1021/acs.estlett.6b00260

7. Jiao X, Shi Q, Gan J. Uptake, accumulation and metabolism of PFASs in plants and health perspectives: A critical review. Critical Reviews in Environmental Science and Technology. 2021 Oct 22;51(23):2745–76. doi:10.1080/10643389.2020.1809219

8. Panieri E, Baralic K, Djukic-Cosic D, Buha Djordjevic A, Saso L. PFAS molecules: a major concern for the human health and the environment. Toxics. 2022 Feb;10(2):2. doi:10.3390/toxics10020044

9. Munoz G, Mercier L, Duy SV, Liu J, Sauvé S, Houde M. Bioaccumulation and trophic magnification of emerging and legacy per- and polyfluoroalkyl substances (PFAS) in a St. Lawrence River food web. Environmental Pollution. 2022 Sep 15;309:119739. doi:10.1016/j.envpol.2022.119739

10. Munoz G, Liu M, Vo Duy S, Liu J, Sauvé S. Target and nontarget screening of PFAS in drinking water for a large-scale survey of urban and rural communities in Québec, Canada. Water Research. 2023 Apr 15;233:119750. doi:10.1016/j.watres.2023.119750

11. Carrizo JC, Munoz G, Vo Duy S, Liu M, Houde M, Amé MV, Liu J, Sauvé S. PFAS in fish from AFFF-impacted environments: Analytical method development and field application at a Canadian international civilian airport. Science of The Total Environment. 2023 Jun 25;879:163103. doi:10.1016/j.scitotenv.2023.163103

12. Canadian Council of Ministers of the Environment. Canadian soil and groundwater quality guidelines for the protection of environmental and human health: perfluorooctane sulfonate (PFOS). Canadian Environmental Quality Guidelines. 2021.

13. Health Canada. Canada.ca [education and awareness] [Internet]. 2023 [cited 2025 Mar 10]. Water talk: Per-and polyfluoroalkyl substances (PFAS) in drinking water. Available from: https://www.canada.ca/en/health-canada/services/environmental-workplace-health/reports-publications/water-quality/water-talk-per-polyfluoroalkyl-substances-drinking-water.html

14. Amen R, Ibrahim A, Shafqat W, Hassan EB. A critical review on PFAS removal from water: removal mechanism and future challenges. Sustainability. 2023 Jan;15(23):23. doi:10.3390/su152316173

15. Trojanowicz M, Bojanowska-Czajka A, Bartosiewicz I, Kulisa K. Advanced oxidation/aeduction processes treatment for aqueous perfluorooctanoate (PFOA) and perfluorooctanesulfonate (PFOS) – A review of recent advances. Chemical Engineering Journal. 2018 Mar 15;336:170–99. doi:10.1016/j.cej.2017.10.153

16. Cui J, Gao P, Deng Y. Destruction of per- and polyfluoroalkyl substances (PFAS) with advanced reduction processes (ARPs): a critical review. Environmental Science & Technology. 2020 Apr 7;54(7):3752–66. doi:10.1021/acs.est.9b05565

17. Gar Alalm M, Boffito DC. Mechanisms and pathways of PFAS degradation by advanced oxidation and reduction processes: a critical review. Chemical Engineering Journal. 2022 Dec 15;450:138352. doi:10.1016/j.cej.2022.138352

18. Kang YG, Birch QT, Nadagouda MN, Dionysiou DD. Advanced destruction technologies for PFAS in soils: Progress and challenges. Current Opinion in Environmental Science & Health. 2023 Jun 1;33:100459. doi:10.1016/j.coesh.2023.100459

19. Blotevogel J, Thagard SM, Mahendra S. Scaling up water treatment technologies for PFAS destruction: current status and potential for fit-for-purpose application. Current Opinion in Chemical Engineering. 2023 Sep 1;41:100944. doi:10.1016/j.coche.2023.100944

20. Rook JC. Degradation of per- and polyfluoroalkyl substances irradiation and MCNP modeling with the SLOWPOKE-2 nuclear reactor [Masters of Applied Science in Chemistry and Chemical Engineering]. [Kingston, Ontario, Canada]: Royal Military College of Canada, Department of Chemistry and Chemical Engineering; 2018.

21. Trojanowicz M, Bartosiewicz I, Bojanowska-Czajka A, Kulisa K, Szreder T, Bobrowski K, Nichipor H, Garcia-Reyes JF, Nałęcz-Jawecki G, Męczyńska-Wielgosz S, Kisała J. Application of ionizing radiation in decomposition of perfluorooctanoate (PFOA) in waters. Chemical Engineering Journal. 2018 Sep 22;357:698–714. doi:10.1016/j.cej.2018.09.065

22. Patch D, O'Connor N, Koch I, Cresswell T, Hughes C, Davies JB, Scott J, O'Carroll D, Weber K. Elucidating degradation mechanisms for a range of per- and polyfluoroalkyl substances (PFAS) via controlled irradiation studies. Science of The Total Environment. 2022 Aug;832:154941. doi:10.1016/j.scitotenv.2022.154941

23. Trojanowicz M, Bartosiewicz I, Bojanowska-Czajka A, Szreder T, Bobrowski K, Nałęcz-Jawecki G, Męczyńska-Wielgosz S, Nichipor H. Application of ionizing radiation in decomposition of perfluorooctane sulfonate (PFOS) in aqueous solutions. Chemical Engineering Journal. 2019 Jul 29;379:122303. doi:10.1016/j.cej.2019.122303

24. Dye JL. Electrons as Anions. Science. 2003 Aug;301(5633):607–8. doi:10.1126/science.1088103

25. Bachman BF, Zhu D, Bandy J, Zhang L, Hamers RJ. Detection of aqueous solvated electrons produced by photoemission from solids using transient absorption measurements. ACS Measurement Science Au. 2022 Feb 16;2(1):46–56. doi:10.1021/acsmeasuresciau.1c00025

26. O'Connor N, Patch D, Noble D, Scott J, Koch I, Mumford KG, Weber K. Forever no more: complete mineralization of per- and polyfluoroalkyl substances (PFAS) using an optimized UV/sulfite/iodide system. Science of The Total Environment. 2023 Aug;888:164137. doi:10.1016/j.scitotenv.2023.164137

27. Samuleev P. SLOWPOKE nuclear reactors in canada [Text] [Internet]. 2016 [cited 2024 Jan 12]. Available from: https://www.rmc-cmr.ca/en/chemistry-and-chemical-engineering/slowpoke-nuclear-reactors-canada

28. Andrews W. Thermal neutron flux mapping around the reactor core of the SLOWPOKE-2 at RMC [Masters of Applied Science in Chemistry and Chemical Engineering]. [Kingston, ON, Canada]: Royal Military College of Canada; 1989.

29. Lamarre GB. Experimental and computational determination of radiation dose rates in the SLOWPOKE-2 research reactor at the Royal Military College of Canada [Masters of Applied Science in Chemistry and Chemical Engineering]. [Canada]: Royal Military College of Canada; 1999.

30. Rook JC, Weber KP, Corcoran EC. Advanced MCNP simulation of the neutron and photon flux and absorbed dose rates for the SLOWPOKE-2 nuclear reactor at the Royal Military College of Canada. Nuclear Technology. 2020 Mar 10;206(12):1861–74. doi:10.1080/00295450.2020.1720557

31. Casper BP. Analysis of decommissioned RMC SLOWPOKE-2 nuclear reactor core and comparison to MCNP simulations [Masters of Applied Science in Chemistry and Chemical Engineering]. [Kingston, Ontario, Canada]: Royal Military College of Canada, Department of Chemistry and Chemical Engineering; 2023.

32. Parent SPJ. Forecast of waste management requirements of uranium dioxide fuelled small modular reactors using a MCNP 6.2 model of the RMC SLOWPOKE-2 reactor [Masters of Applied Science in Chemistry and Chemical Engineering] [Internet]. Royal Military College of Canada; 2023 [cited 2024 Jan 17]. Available from: https://espace.rmc.ca:8443/jspui/handle/11264/1305

33. Huston DA, Samuleev P, Kelly F, Corcoran EC. Characterization of flux distribution in the pool of the RMC SLOWPOKE-2. Applied Radiation and Isotopes. 2024 Feb 27;111262. doi:10.1016/j.apradiso.2024.111262

34. Los Alamos National Laboratory. MCNP® Website and MCNP6.3 user manual [Internet]. [cited 2023 Oct 23]. Available from: https://mcnp.lanl.gov/

35. Blois MS. Antioxidant determinations by the use of a stable free radical. Nature. 1958 Apr;181(4617):1199–200. doi:10.1038/1811199a0

36. Lassalle J, Gao R, Rodi R, Kowald C, Feng M, Sharma VK, Hoelen T, Bireta P, Houtz EF, Staack D, Pillai SD. Degradation of PFOS and PFOA in soil and groundwater samples by high dose electron beam technology. Radiation Physics and Chemistry. 2021 Dec 1;189:109705. doi:10.1016/j.radphyschem.2021.109705

37. Health Canada. Per- and polyfluoroalkyl substances (PFAS) [education and awareness] [Internet]. 2021 [cited 2025 Mar 10]. Available from: https://www.canada.ca/en/health-canada/services/chemical-substances/other-chemical-substances-interest/per-polyfluoroalkyl-substances.html

38. Health Canada. Perfluorooctanoic Acid (PFOA), its salts, and its precursors - information sheet [frequently asked questions] [Internet]. 2017 [cited 2025 Mar 18]. Available from: https://www.canada.ca/en/health-canada/services/chemical-substances/fact-sheets/chemicals-glance/perfluorooctanoic-acid-pfoa-salts-precursors-public-summary.html

39. Buck RC, Franklin J, Berger U, Conder JM, Cousins IT, de Voogt P, Jensen AA, Kannan K, Mabury SA, van Leeuwen SP. Perfluoroalkyl and polyfluoroalkyl substances in the environment: Terminology, classification, and origins. Integrated Environmental Assessment and Management. 2011;7(4):513–41. doi:10.1002/ieam.258

40. Health Canada. Supporting document: ecological state of the science report on short-chain (C4–C7) perfluorocarboxylic acids (SC-PFCAs) short-chain (C4–C7) perfluorosulfonic acids (SC-PFSAs) long-chain (C9–C20) perfluorosulfonic acids (LC-PFSAs) [assessments] [Internet]. 2023 [cited 2026 Mar 9]. Available from: https://www.canada.ca/en/environment-climate-change/services/evaluating-existing-substances/supporting-document-ecological-state-science-report-sc-pfcas-sc-pfsas-lc-pfsas.html

41. RCSB Protein Data Bank. Chemical Sketch Tool [Internet]. [cited 2025 Mar 6]. Available from: https://www.rcsb.org/chemical-sketch

42. Chemaxon. Legacy Marvin Software [Internet]. [cited 2025 Mar 6]. Available from: https://chemaxon.com/marvinsketch_js

43. Bergwerf H. MolView [Internet]. [cited 2024 Mar 7]. MolView. Available from: https://molview.org/?cid=9554

44. Meegoda JN, Bezerra de Souza B, Casarini MM, Kewalramani JA. A review of PFAS destruction technologies. International Journal of Environmental Research and Public Health. 2022 Jan;19(24):24. doi:10.3390/ijerph192416397

45. Turner LP, Kueper BH, Patch DJ, Weber KP. Elucidating the relationship between PFOA and PFOS destruction, particle size and electron generation in amended media commonly found in soils. Science of The Total Environment. 2023 Aug 25;888:164188. doi:10.1016/j.scitotenv.2023.164188

46. Schindewolf U. Formation and properties of solvated electrons. Angewandte Chemie International Edition in English. 1968 Mar;7(3):190–203. doi:10.1002/anie.196801901

47. Yamamoto Y ichi, Suzuki T. Ultrafast dynamics of water radiolysis: hydrated electron formation, solvation, recombination, and scavenging. The Journal of Physical Chemistry Letters. 2020 Jul 16;11(14):5510–6. doi:10.1021/acs.jpclett.0c01468

48. Svoboda V, Michiels R, LaForge AC, Med J, Stienkemeier F, Slavíček P, Wörner HJ. Real-time observation of water radiolysis and hydrated electron formation induced by extreme-ultraviolet pulses. Science Advances. 2020 Jan 17;6(3):eaaz0385. doi:10.1126/sciadv.aaz0385

49. Zhang Z, Chen JJ, Lyu XJ, Yin H, Sheng GP. Complete mineralization of perfluorooctanoic acid (PFOA) by γ-irradiation in aqueous solution. Scientific reports. 2014 Dec 10;4:7418. doi:10.1038/srep07418

50. Jay-Gerin JP. Fundamentals of water radiolysis. Encyclopedia. 2025 Mar;5(1):38. doi:10.3390/encyclopedia5010038

51. Dissolved Oxygen. Environmental Measurement Systems [Internet]. [cited 2026 Apr 15]. Available from: https://www.fondriest.com/environmental-measurements/parameters/water-quality/dissolved-oxygen/

52. McTaggart M, Malardier-Jugroot C. The role of helicity in PFAS resistance to degradation: DFT simulation of electron capture and defluorination. Physical Chemistry Chemical Physics. 2024 Jan 22;26. doi:10.1039/D3CP04973F

53. Dixon RS, Bailey MG. Effects of electron scavengers in the radiolysis of water vapor. Canadian Journal of Chemistry. 1968 Apr 15;46(8):1181–6. doi:10.1139/v68-202

54. A. Paulenova. Physical and chemical properties of actinides in nuclear fuel reprocessing. In: Kenneth L. Nash, Gregg J. Lumetta, editors. Advanced Separation Techniques for Nuclear Fuel Reprocessing and Radioactive Waste Treatment. 1st ed. Woodhead Publishing; 2011. p. 35.

55. A. J. Elliot, D. M. Bartels. The reaction set, rate constants and g-galues for the simulation of the radiolysis of light water over the range 20° to 350°C based on the information available in 2008 [Internet]. 2251 Speakman Drive Mississauga, Ontario Canada L5K 1B2: Atomic Energy of Canada Limited; 2009 Aug [cited 2024 Mar 26]. p. 148. (Nuclear Platform Research and Development). Available from: https://inis.iaea.org/collection/NCLCollectionStore/_Public/41/057/41057263.pdf

56. Seki H, Imamura M. Radiolysis yields from γ-irradiated liquid methanol containing nitrous oxide and the effect of acid. The Institute of Physical and chemical Research, Tokyo, Japan. 1966 May 1. Located at: world. doi:10.1021/j100863a014

57. Baxendale JH, Wardman P. The radiolysis of methanol : product yields, rate constants, and spectroscopic parameters of intermediates [Internet]. 1st ed. Gaithersburg, MD: National Bureau of Standards; 1975 [cited 2024 Apr 9]. p. NBS NSRDS 54. Report NBS NSRDS 54. Available from: https://nvlpubs.nist.gov/nistpubs/Legacy/NSRDS/nbsnsrds54.pdf doi:10.6028/NBS.NSRDS.54

58. Lamarsh JR, Baratta AJ. Introduction to nuclear engineering. 3rd ed. Upper Saddle River, NJ: Prentice Hall; 2001. 783 p. (Addison-Wesley series in nuclear science and engineering).

59. Canadian Nuclear Association. How a nuclear reactor works. Nuclear Explained [Internet]. [cited 2024 Mar 12]. Available from: https://cna.ca/reactors-and-smrs/how-a-nuclear-reactorworks/

60. KAERI. Nuclear Data Center at KAERI [Internet]. [cited 2024 Feb 12]. Table of Nuclides. Available from: https://atom.kaeri.re.kr/nuchart/#

61. Azizul Khakim. A concept on calculating radiolysis rate with MCNP code. In. Indonesia: Center for Nuclear Energy Systems, National Nuclear Energy Agency; 2019. p. 547. (Konsep perhitungan laju radiolisis dengan code MCNP).

62. Pavel Samuleev. Reactor water temperature (Private communication). 2025.

63. Peter Gehringer. Radiation processing of aqueous systems [Seibersdorf Report]. 37: Seibersdorf; 1997 Sep.

64. Muroya Y, Lin M, Han Z, Kumagai Y, Sakumi A, Ueda T, Katsumura Y. Ultra-fast pulse radiolysis: a review of the recent system progress and its application to study on initial yields and solvation processes of solvated electrons in various kinds of alcohols. Radiation Physics and Chemistry. 2008 Oct 1;The International Symposium on Charged Particle and Photon Interaction with Matter - ASR 200777(10):1176–82. doi:10.1016/j.radphyschem.2008.05.035

65. Brand-Williams W, Cuvelier ME, Berset C. Use of a free radical method to evaluate antioxidant activity. LWT - Food Science and Technology. 1995 Jan 1;28(1):25–30. doi:10.1016/S0023-6438(95)80008-5

66. Yeo J, Shahidi F. Revisiting DPPH (2,2-diphenyl-1-picrylhydrazyl) assay as a useful tool in antioxidant evaluation: A new IC100 concept to address its limitations. Journal of Food Bioactives. 2019 Sep 30;7. doi:10.31665/JFB.2019.7196

67. de Menezes BB, Frescura LM, Duarte R, Villetti MA, da Rosa MB. A critical examination of the DPPH method: mistakes and inconsistencies in stoichiometry and IC_{50} determination by UV–Vis spectroscopy. Analytica Chimica Acta. 2021 May 1;1157:338398. doi:10.1016/j.aca.2021.338398

68. Rivaton A, Lao L, Arnold J. Fast neutron irradiation effects on organic polymers: suitability for dosimetry purposes? Radiation Physics and Chemistry. 2011 Jan 1;80(1):89–93. doi:10.1016/j.radphyschem.2010.08.007

69. Marfak A, Trouillas P, Allais DP, Champavier Y, Calliste CA, Duroux JL. Radiolysis of kaempferol in water/methanol mixtures. Evaluation of antioxidant activity of kaempferol and products formed. Journal of Agricultural and Food Chemistry. 2003 Feb 1;51(5):1270–7. doi:10.1021/jf020836g

70. Marfak A, Trouillas P, Allais DP, Calliste CA, Cook-Moreau J, Duroux JL. Mechanisms of transformation of the antioxidant kaempferol into depsides. gamma-radiolysis study in methanol and ethanol. Radiation Research. 2003 Sep 1;160(3):355–65. doi:10.1667/RR3024

71. Adrian Pang. HPLC-MSMS Methodology for DPPH and PFOA Analysis by ESG (Private communication). 2025.

72. Kannan UR, Narayanasamy G, Subramanian S, Selvarajan P. Spectroscopic, NLO and thermal studies of single crystals of picric acid. International Journal of Research and Analytical Reviews. 2018 Jun 26;5(3):685–93.

73. Versatile, Routine UV-Vis Instrument, Cary 60 | Agilent [Internet]. [cited 2025 Feb 28]. Available from: https://www.agilent.com/en/product/molecular-spectroscopy/uv-vis-uv-vis-nir-spectroscopy/uv-vis-uv-vis-nir-systems/cary-60-uv-vis-spectrophotometer?gad_source=1&gclid=Cj0KCQiA2oW-BhC2ARIsADSIAWooZsrdzJPUkyp7EDxRe_ebxYrQSOmO3JTp3arRMKqkcQuYqS7dHscaAtMREALw_wcB&gclsrc=aw.ds#relatedproducts

74. Romand J, Vodar B. Spectres d'absorption du benzene a l'etat vapeur et a l'etat condense dans l'ultraviolet lointain. Compt Rend. 1951;233:930–2.

75. Milli-Q Lab Water Solutions. Synergy water purification systems user manual. Millipore Sigma; 2019.

Appendix A Samples MCNP6.3 Input Code

This appendix includes only major changes to the input codes found in [31–33]. The full code can be found in the nuclear research group files at the RMC. This sample code is from the input deck chosen to investigate the neutron and photon fluxes and dose rates at all ten irradiation sites for water samples.

The input code samples a separated between the cell card and data card.

The code refers to the reactor container as the reactor vessel.

Input code sample: current version intro and cell card changes.

```
  MCNP Model of RMC's SLOWPOKE-2 LEU, New Aligned Core
C Unshielded Sample in Inner Site no 2
C Control Rod at 9.105 cm (8.8 kW)
C Shims at 0 cm
C
C 9 Jan 25 changes
C - act fission to include delayed gammas
C - nonfiss to include delayed gammas and neutrons
C - bin-wise emission of delayed gammas
C
C 25 Nov 24
C - added an additional flux tally to separate neutrons into energy bins as per lamarsh definitions
C - Changed material in sample vials to water
C - 5 mil neutron histories, 115 cycles, 15 removed
C
C 07 Oct 24
C - tallies for n and p doses and flux, flux binned as per Danny's work
C
C 14 Aug 24 - changed material 410 in cell 5 to 400, which is also water at the same temp, but a
diff color.
C - made all waters that same color, 410 and 500 became material 400.
C
C 12 August 24, changes made by Capt Tristan Gauthier
C - Removed cell 114, as it was drawing a structure not actually found in the SP-2 in reality
C - the decision was made after discussion with Dr. Samuleev and investigating the fuel cage
assembly duplicate -
C - held by the SP-2 director.
C - added a tally tag to count electrons produced, and what action is producing them.
C - added a tally tag to bin electrons produced based on the energy they have
C
C 13 June 24, Changes made by Capt Tristan Gauthier
C - Added Vials of MeOH to all four outer sites
C - Commented out the scaling factor from flux tallies as it was incorrect. It is available to
insert in the future
```

```
C - redid the energy bins for neutron and photon flux, matching Danny's
C - removed comments left by Simon on vial materials, as they have been confirmed
C - Added a universe 152 for outside the reactor vessel, and put in a MeOH vial in the pool site
within 152
C
C 27 May 24, Changes made by Capt Tristan Gauthier
C - Blanking the shielding, paper, inner tube and wire from the sample vial
C - filled vial with MeOH
C - running to determining the neutron flux and dose inside the vial
C - Adding vials of MeOH to every inner site
C - Corrected the heavy water to have deuterium instead of H
C - Changed rod height to 9.105 cm as per half power (9.105 z term)
C - Increased amount of Keff runs to 130, and discarded 30
C
C October 2022, Alterations made by LCdr Simon P.J. Parent
C - General code maintenance (layout, titles, etc)
C - Updated fuel density (10.70 g/cm3 vice 10.60g/cm3) to correspond to
C   information received from AECL during refuelling
C - Updated the core layout to reflect the new core's element positioning
C    (195 elements vice 198)
C - Aligned the core 10 degrees clockwise to align with RMC Core's actual
C   position
C - Removal of legacy code with no purpose (surfaces and cells)
C - Removed 7cc cells created by Rook and inserted samples (cells, surfaces,
C   materials) used in NAA experimentation conducted in August 2022
C - Defined Site 8 as the flooded site, filled with reactor container light
C   water
C - Updated the whole model to ENDF\B-VIII
C - Modified self-powered neutron detector to be more representative of the
C    actual installed detector
C - Altered the reactor pool to conform to the dimensions of the pool (2.46m diameter)
C - Raised reactor container and radiation tube to the upper limit of the pool
C
C April 2018 alterations made by JADEN ROOK
C - Berylliyium MAT Impurities added
C - Defined 7cc cells in the inner and outer irradiation sites
C - Cadmium Lining on outesite #9
C - All Fuelpins use same mcard (fresh fuel)
C
C    The followiing modifications were made by Dr. C. Jewett in February 2017:
C 1. Changes to the control rod geometry to make it conform to drawings A15292 a
```

```
C 2. Addition of the conical control rod sheath tip to the control rod geometry
C The followint modifications were made by Dr. C. Jewett in March 2017:
C 1. Shifted the control rod so that it touches the bottom of the water cell hol
C 2. The following temperature changes were made:
C    a. Irradiation Tubes were tmp = 2.87087E-08, everything else was tmp = 2.58
C    b. Irradiation tubes are now tmp = 2.52607355E-08, everything else is now t
C 3. The following temperature change was made on 24 March 2017
C    a. Irradiation Tubes were tmp = 2.87087E-08
C    b. Irradiation tubes are now tmp = 2.52607355E-08
C _____________________________________________________________________________
C ****************************** CELL CARDS*******************************
C _____________________________________________________________________________
C
1 0 600 imp:n=0 $Void outside of the pool
C
C Lower Container Section
2    0          (-701 -703 -710):(710 -701)     imp:n=1  fill=151 $ inside cont
3    800 -2.70 ((-700 -702 -711):(711 -700)) #2 imp:n=1 $ container wall
4    0           -600 (700:(702 -711))          imp:n=1 fill=152 $ Pool water
     tmp=2.52607355E-08
5    400 -0.9966 #420 u=152 imp:n=1 $ Exclude anything you put in the pool
C
```

This line delineates a jump in code.

```
C -------1---------2---------3---------4---------5---------6---------7---------8
C
C ***************************** CONTROL ROD *********************************
C _____________________________________________________________________________
C NB: The control rod is fully inserted if z = -0.750158865031 cm
C Rod height controlled by changing third term (Z) into trcl=(X Y Z) of cell 350
C Model Rod height= 9.105 cm
350  0             -350 trcl=(0 0 9.105) fill=350  u=151 imp:n=1 $ control rod
c
3410 700 -1.854  -340 +341 -342 (-343:+344)  u=340 imp:n=1 $ be
     tmp=2.52607355E-08
3420 400 -.9966  #3410                     u=340 imp:n=1 $ h2o
     tmp=2.52607355E-08
C
3510 800 -2.7    +3501 +3503 +3507             u=350 imp:n=1 $ outer Al-tube (Co
3511 800 -2.7    -3502 -3503 3504 :(-3502 -3505 -3504 ):-3506 u=350 imp:n=1 $ ou
3520 800 -2.7    -351 +3511 #3531 #3532        u=350 imp:n=1 $ Al-enclosure and
```

```
3525 800 -2.7    -3512 +352 u=350 imp:n=1 $ Inner Al-enclosere (Control Rod Inse
3530 900 -8.65   110 -111          u=350 imp:n=1 $ cd-tube
3531 800 -2.7    +1101 -35111 u=350 imp:n=1 $ lower weld
3532 800 -2.7    +1102 -35112 u=350 imp:n=1 $ uppwer weld
3540 330 -0.0014 +3503 #3510 #3511 #3530 #3531 #3532 #3525 #3520 u=350 imp:n=1 $
3545 400 -0.9966 -3503 #3511  u=350 imp:n=1 $ water below the control rod sheath
C
380  800 -2.70  -380 +381 +382 -300 u=151 imp:n=1 $ Thrust Ring
C
C
C -------1---------2---------3---------4---------5---------6---------7---------8
C
C ***************************** INNER SITES **********************************
C ______________________________________________________________________________
C Altered by LCdr Simon P.J. Parent, September 2022
C
C Altered by Capt Gauthier T.M. May 2024
C -------------------------
C IRRADIATION TUBE NO 1
C -------------------------
321  0 -322 trcl=(14.4941   4.7094 0)  fill=321   u=151 imp:n=1
         tmp=2.52607355E-08
3210  800 -2.7     3220                 u=321 imp:n=1 $ wall
3211  800 -2.70   -3221  3222                   u=321 imp:n=1 $ sample tube
3212  330 -0.0014 -3220 #3211 #812 #813 #815    u=321 imp:n=1 $ air
812   813 -0.92   -900   901                    u=321 imp:n=1 $ 7cc vial
813   812 -0.905  -902   903   904              u=321 imp:n=1 $ 2cc vial
815  400 -0.7866 -904                          u=321 imp:n=1 $ Sample filled with water
C
C
C -------------------------
C IRRADIATION TUBE NO 2
C -------------------------
322  0 -322 trcl=(8.9578 -12.3294 0)  fill=322   u=151 imp:n=1
              tmp=2.52607355E-08
3220 800 -2.7          3220         u=322 imp:n=1 $ wall
3221 800 -2.70   -3221 3222         u=322 imp:n=1 $ sample tube
3222 330 -0.0014 -3220 #3221 #822 #823 #825     u=322 imp:n=1 $ air
822  813  -0.92   -900 901                     u=322 imp:n=1 $ 7cc vial
823  812  -0.905  -902 903 904                u=322 imp:n=1 $ 2cc vial
```

```
C 704  815  -0.92   -905 906                  u=322 imp:n=1 $ Inner tube, commented out
825  400 -0.7866 -904                          u=322 imp:n=1 $ Sample wire turned to now this is
filled with water soln
C 706  330  -8.65   -909 908                  u=322 imp:n=1 $ Cadmium Shielding (0.5mm) now this
is air and commented out
C 707  400 -0.7866 -904 910                  u=322 imp:n=1 $ Filter paper holder now this is air,
also its gone now
C
C
C ------------------------
C IRRADIATION TUBE NO 3
C ------------------------
323  0 -322 trcl=(-8.9578 -12.3294 0)  fill=323   u=151 imp:n=1
            tmp=2.52607355E-08
3230  800 -2.7          3220         u=323 imp:n=1 $ wall
3231  800 -2.70   -3221 3222         u=323 imp:n=1 $ sample tube
3232  330 -0.0014 -3220 #3231 #832 #833 #835       u=323 imp:n=1 $ air
832   813 -0.92   -900   901                       u=323 imp:n=1 $ 7cc vial
833   812 -0.905  -902   903  904                  u=323 imp:n=1 $ 2cc vial
835  400 -0.7866 -904                            u=323 imp:n=1 $ Sample filled with water
C
C
C ------------------------
C IRRADIATION TUBE NO 4
C ------------------------
324  0 -322 trcl=(-14.4941   4.7094 0)  fill=324   u=151 imp:n=1
            tmp=2.52607355E-08
3240  800 -2.7           3220         u=324 imp:n=1 $ wall
3241  800 -2.70   -3221  3222         u=324 imp:n=1 $ sample tube
3242  330 -0.0014 -3220 #3241 #842 #843 #845    u=324 imp:n=1 $ air
842   813 -0.92    -900   901                   u=324 imp:n=1 $ 7cc vial
843   812 -0.905   -902   903  904              u=324 imp:n=1 $ 2cc vial
845  400 -0.7866  -904                         u=324 imp:n=1 $ water
C
C
C ------------------------
C IRRADIATION TUBE NO 5
C ------------------------
325  0 -322 trcl=(0 15.24 0)  fill=325   u=151 imp:n=1
        tmp=2.52607355E-08
3250 800 -2.7           3220         u=325 imp:n=1 $ wall
3251 800 -2.70   -3221  3222         u=325 imp:n=1 $ sample tube
```

```
3252 330 -0.0014 -3220 #3251 #852 #853 #855 u=325 imp:n=1 $ air
852   813 -0.92   -900   901                u=325 imp:n=1 $ 7cc vial
853   812 -0.905  -902   903  904           u=325 imp:n=1 $ 2cc vial
855  400 -0.7866 -904                      u=325 imp:n=1 $ water
C
C
C -------1---------2---------3---------4---------5---------6---------7---------8
C
C ****************************** OUTER SITES **********************************
C ________________________________________________________________________________
C Altered by LCdr Simon P.J. Parent, September 2022
C
C - Altered by Capt Tristan M. Gauthier, June 2024
C
C ------------------------
C IRRADIATION TUBE NO 6
C ------------------------
726  0 -722 trcl=(22.82536 -7.41641 0) fill=726 u=151 imp:n=1 tmp=2.52607355E-08
7261 800 -2.7 723                      u=726 imp:n=1 $ wall
7262 330 -0.0014 -723 #862 #863 #865           u=726 imp:n=1 $ air
862   813 -0.92   -900   901                   u=726 imp:n=1 $ 7cc vial
863   812 -0.905  -902   903   904             u=726 imp:n=1 $ 2cc vial
865  400 -0.7866 -904                         u=726 imp:n=1 $ Sample filled with water
C
C
C ------------------------
C IRRADIATION TUBE NO 8 Flooded Site
C ------------------------
728 0 -722 trcl=(-22.82536 -7.41641 0) fill=728 u=151 imp:n=1 tmp=2.52607355E-08
7281 800 -2.7          723             u=728 imp:n=1 $ wall
7282 400 -0.0014 -723 #882 #7283 #883 #885      u=728 imp:n=1 $ Container light water
7283 330 -0.0014 -901 #883 #885                 u=728 imp:n=1 $ air between 7cc vial and 2cc vial
882   813 -0.92   -900   901                   u=728 imp:n=1 $ 7cc vial
883   812 -0.905  -902   903   904             u=728 imp:n=1 $ 2cc vial
885  400 -0.7866 -904                         u=728 imp:n=1 $ Sample filled with water
C
C
C ------------------------
C IRRADIATION TUBE NO 9 Cadmium lined
C ------------------------
```

```
729 0 -724 trcl=(-14.10685 19.41641 0) fill=729 u=151 imp:n=1 tmp=2.52607355E-08
7291 800 -2.7     723 -722              u=729 imp:n=1 $wall, still needs a bottom
7292 330 -0.0014 -723 #892 #893 #895    u=729 imp:n=1 $air
7293 900 -8.65    722                   u=729 imp:n=1 $cadmium lining
892   813 -0.92   -900   901            u=729 imp:n=1 $ 7cc vial
893   812 -0.905  -902   903   904      u=729 imp:n=1 $ 2cc vial
895  400 -0.7866 -904                  u=729 imp:n=1 $ Sample filled with water
C
C
C ------------------------
C IRRADIATION TUBE NO 10
C ------------------------
720  0 -722 trcl=(14.10685 19.41641 0) fill=720 u=151 imp:n=1 tmp=2.52607355E-08
7201 800 -2.7          723                 u=720 imp:n=1 $ wall
7202 330 -0.0014 -723 #802 #803 #805       u=720 imp:n=1 $ air
802   813 -0.92   -900 901                     u=720 imp:n=1 $ 7cc vial
803   812 -0.905  -902   903   904         u=720 imp:n=1 $ 2cc vial
805  400 -0.7866 -904                    u=720 imp:n=1 $ Sample filled with water
C
C
C ------------------------
C Pool Site
C ------------------------
C
420 0 -900 trcl=(-38.8636 0 0) fill=420 u=152 imp:n=1 tmp=2.52607355E-08
421   330 -0.0014 -901 #403 #405         u=420 imp:n=1 $ air between 7cc vial and 2cc vial 7.58231
402   813 -0.92    901                    u=420 imp:n=1 $ 7cc vial
403   812 -0.905  -902  903  904          u=420 imp:n=1 $ 2cc vial
405  400 -0.7866 -904                    u=420 imp:n=1 $ Sample filled with water
C
```

Input code sample: data card changes.

```
C ------------------------
C Methanol Liquid at 25.5 degrees C (density 0.7866 g/cm3)
C ------------------------
C - Added by Capt Gauthier T.M. May 2024
m4800 6012.00c 1 $ natural carbon
      8016.00c 1 $ natural oxygen
      1001.00c 4 $ natural hydrogen
C
C _________________________________________________________________________
```

```
C
C ********************************* TALLIES ***********************************
C ______________________________________________________________________________
C
FC104 Neutron Flux at the Sample my bins
F104:N 815 825 835 845 855 865 885 895 805 405
E104 5e-7 1e-3 1e2
C
FC114 Neutron Flux at the Sample old bins
F114:N 815 825 835 845 855 865 885 895 805 405
E114 6.25e-7 4e-6 1e2
C
FC206 Neutron Dose Rate at the Sample
F206:N 815 825 835 845 855 865 885 895 805 405
C
FC124 Photon Flux at the Sample one bin
F124:P 815 825 835 845 855 865 885 895 805 405
C
FC134 Photon Flux at the Sample Binned
F134:P 815 825 835 845 855 865 885 895 805 405
E134 0.1 0.15 0.2 0.3 0.4 0.5 0.6 0.8 1.0 1.25 1.50 2 3 4 5 6 8 10
C
FC216 Photon Dose Rate at the Sample
F216:P 815 825 835 845 855 865 885 895 805 405
C
C -------1---------2---------3---------4---------5---------6---------7---------8
C ______________________________________________________________________________
C
C ********************************* RUN PARAMETERS*******************************
C ______________________________________________________________________________
C
mode p n
totnu
kcode 500000 1.0 15 115
C
rand gen=1 seed=100009
ksrc  1.1 -1.9 12 $ [0 -2 0]
     -1.1  1.9 12 $ [0  2 0]
C
ACT FISSION=N, P  nonfiss=n, p   dg=mg
```

```
print
C
C _____________________________________________________________________
C ******************************** END ***********************************
C _____________________________________________________________________
C -------1---------2---------3---------4---------5---------6---------7---------8
```

Appendix B Sample MCNP6.3 Output Code

This appendix includes an example of only major results from simulations used in this thesis. The full code can be found in the nuclear research group files at the RMC. This sample code is from the input deck chosen to investigate the neutron and photon fluxes and dose rates at all ten irradiation sites for water samples.

The output code samples are separated between physics results and the tally results.

Output code sample: Physics results.

```
------------------------------------------------------------------------------------------------------------
---------------------------------

 |
|

 | the final estimated combined collision/absorption/track-length keff = 0.996889 with an estimated
standard deviation of 0.000163 |

 |
|

 | the estimated 68, 95, & 99 percent keff confidence intervals are 0.99673 to 0.99705, 0.99656 to
0.99721, and 0.99646 to 0.99732 |

 |
|

 | the final combined (col/abs/tl) prompt removal lifetime = 1.6226E-04 seconds with an estimated
standard deviation of 7.9515E-07 |

 |
|

 |     the     average     neutron     energy     causing     fission     =     4.2916E-02     mev
|

 | the energy corresponding to the average neutron lethargy causing fission = 9.5660E-08 mev
|

 |
|

 | the percentages of fissions caused by neutrons in the thermal, intermediate, and fast neutron
ranges are:                          |

 |         (<0.625 ev):  90.60%         (0.625 ev - 100 kev):   7.57%          (>100 kev):   1.83%
|

 |
|

 | the average fission neutrons produced per neutron absorbed (capture + fission) in all cells with
fission = 1.9258E+00           |

 | the average fission neutrons produced per neutron absorbed (capture + fission) in all the
geometry cells = 9.6394E-01           |

 |
|

 |     the     average     number     of     neutrons     produced     per     fission     =     2.434
|

 |
|

 ------------------------------------------------------------------------------------------------------------
---------------------------------
```

Output code sample: Tally results.

```
1tally      104        nps =    57520329
+                                  Neutron Flux at the Sample my bins
          tally type 4    track length estimate of particle flux.      units   1/cm**2
          particle(s): neutrons
 number of histories used for normalizing tallies =     50000000.00

          volumes
                  cell:      815          825          835          845          855          865
885
                         2.81921E+00    2.81921E+00    2.81921E+00    2.81921E+00    2.81921E+00
2.81921E+00  2.81921E+00
                  cell:      895          805          405
                         2.81921E+00  2.81921E+00  2.81921E+00

 cell  815
      energy
    5.0000E-07   6.13697E-04 0.0044
    1.0000E-03   2.46282E-04 0.0061
    1.0000E+02   4.47605E-04 0.0044
      total      1.30758E-03 0.0029

 cell  825
      energy
    5.0000E-07   5.92543E-04 0.0045
    1.0000E-03   2.50699E-04 0.0061
    1.0000E+02   4.47081E-04 0.0045
      total      1.29032E-03 0.0030

 cell  835
      energy
    5.0000E-07   6.02543E-04 0.0045
    1.0000E-03   2.47953E-04 0.0061
    1.0000E+02   4.41859E-04 0.0045
      total      1.29235E-03 0.0030

 cell  845
      energy
    5.0000E-07   6.16051E-04 0.0044
    1.0000E-03   2.46198E-04 0.0062
```

```
   1.0000E+02   4.41454E-04 0.0045
     total      1.30370E-03 0.0029

cell  855
     energy
   5.0000E-07   6.05035E-04 0.0045
   1.0000E-03   2.46141E-04 0.0061
   1.0000E+02   4.43235E-04 0.0045
     total      1.29441E-03 0.0030

cell  865
     energy
   5.0000E-07   2.90683E-04 0.0060
   1.0000E-03   3.35406E-05 0.0163
   1.0000E+02   4.23133E-05 0.0140
     total      3.66537E-04 0.0053

cell  885
     energy
   5.0000E-07   2.88609E-04 0.0060
   1.0000E-03   3.21989E-05 0.0161
   1.0000E+02   4.20964E-05 0.0137
     total      3.62904E-04 0.0053

cell  895
     energy
   5.0000E-07   1.65148E-05 0.0251
   1.0000E-03   3.19466E-05 0.0163
   1.0000E+02   4.17403E-05 0.0140
     total      9.02018E-05 0.0103

cell  805
     energy
   5.0000E-07   2.92172E-04 0.0059
   1.0000E-03   3.30945E-05 0.0162
   1.0000E+02   4.13288E-05 0.0139
     total      3.66595E-04 0.0053

cell  405
     energy
```

```
    5.0000E-07   7.89065E-06 0.0361
    1.0000E-03   5.20712E-07 0.1387
    1.0000E+02   8.62435E-07 0.0922
      total      9.27380E-06 0.0340


 ***** the nps-dependent tfc bin check results are suspect because there are only  1 nps tally
values to analyze *****


================================================================================================
==================================


           results of 10 statistical checks for the estimated answer for the tally fluctuation
chart (tfc) bin of tally      104


 tfc bin     --mean--       ---------relative error---------      ----variance of the variance----
--figure of merit--     -pdf-
 behavior    behavior      value   decrease   decrease rate      value   decrease   decrease rate
value     behavior     slope


 desired       random        <0.10       yes       1/sqrt(nps)        <0.10       yes         1/nps
constant    random      >3.00
 observed      random         0.00       yes           yes             0.00       yes          yes
constant    random       8.09
 passed?         yes           yes       yes           yes              yes       yes          yes
yes         yes          yes


================================================================================================
==================================
```

This line delineates a jump in code.

```
1tally      114        nps =    57520329
+                                  Neutron Flux at the Sample old bins
           tally type 4    track length estimate of particle flux.      units   1/cm**2
           particle(s): neutrons
 number of histories used for normalizing tallies =     50000000.00


           volumes
                   cell:      815          825          835          845          855
865          885
                           2.81921E+00  2.81921E+00  2.81921E+00  2.81921E+00  2.81921E+00
2.81921E+00  2.81921E+00
```

```
                cell:      895          805          405
                       2.81921E+00  2.81921E+00  2.81921E+00

cell  815
     energy
   6.2500E-07   6.21043E-04 0.0044
   4.0000E-06   5.63155E-05 0.0111
   1.0000E+02   6.30225E-04 0.0038
     total      1.30758E-03 0.0029

cell  825
     energy
   6.2500E-07   5.99990E-04 0.0045
   4.0000E-06   5.74258E-05 0.0113
   1.0000E+02   6.32907E-04 0.0039
     total      1.29032E-03 0.0030

cell  835
     energy
   6.2500E-07   6.09874E-04 0.0044
   4.0000E-06   5.72006E-05 0.0114
   1.0000E+02   6.25280E-04 0.0039
     total      1.29235E-03 0.0030

cell  845
     energy
   6.2500E-07   6.23001E-04 0.0044
   4.0000E-06   5.63727E-05 0.0111
   1.0000E+02   6.24329E-04 0.0039
     total      1.30370E-03 0.0029

cell  855
     energy
   6.2500E-07   6.12362E-04 0.0044
   4.0000E-06   5.63320E-05 0.0113
   1.0000E+02   6.25717E-04 0.0039
```

```
     total      1.29441E-03 0.0030

cell  865
     energy
   6.2500E-07   2.91778E-04 0.0059
   4.0000E-06   8.96557E-06 0.0298
   1.0000E+02   6.57926E-05 0.0115
     total      3.66537E-04 0.0053

cell  885
     energy
   6.2500E-07   2.89840E-04 0.0060
   4.0000E-06   9.05564E-06 0.0276
   1.0000E+02   6.40078E-05 0.0115
     total      3.62904E-04 0.0053

cell  895
     energy
   6.2500E-07   1.76070E-05 0.0244
   4.0000E-06   8.46622E-06 0.0289
   1.0000E+02   6.41286E-05 0.0116
     total      9.02018E-05 0.0103

cell  805
     energy
   6.2500E-07   2.93336E-04 0.0059
   4.0000E-06   8.90788E-06 0.0285
   1.0000E+02   6.43507E-05 0.0115
     total      3.66595E-04 0.0053

cell  405
     energy
   6.2500E-07   7.90020E-06 0.0361
   4.0000E-06   1.30726E-07 0.2118
   1.0000E+02   1.24287E-06 0.0846
     total      9.27380E-06 0.0340
```

***** the nps-dependent tfc bin check results are suspect because there are only 1 nps tally values to analyze *****

==========

results of 10 statistical checks for the estimated answer for the tally fluctuation chart (tfc) bin of tally 114

tfc bin	--mean--	---------relative error---------			----variance of the variance----			--figure of merit--	-pdf-
behavior	behavior	value	decrease	decrease rate	value	decrease	decrease rate	value	behavior	slope
desired	random	<0.10	yes	1/sqrt(nps)	<0.10	yes	1/nps	constant	random	>3.00
observed	random	0.00	yes	yes	0.00	yes	yes	constant	random	8.09
passed?	yes	yes	yes	yes	yes	yes	yes	yes	yes	yes

==========

This line delineates a jump in code.

1tally 206 nps = 57520329

\+ Neutron Dose Rate at the Sample

tally type 6 track length estimate of heating. units mev/gram

particle(s): neutrons

number of histories used for normalizing tallies = 50000000.00

masses

cell:	815	825	835	845	855	865	885	
	2.21759E+00	2.21759E+00	2.21759E+00	2.21759E+00	2.21759E+00	2.21759E+00	2.21759E+00	
cell:	895	805	405					
	2.21759E+00	2.21759E+00	2.21759E+00					

```
 cell  815
                3.97124E-05 0.0057

 cell  825
                3.93485E-05 0.0058

 cell  835
                3.89837E-05 0.0058

 cell  845
                3.89126E-05 0.0058

 cell  855
                3.94631E-05 0.0058

 cell  865
                4.04166E-06 0.0186

 cell  885
                4.10716E-06 0.0180

 cell  895
                4.02502E-06 0.0181

 cell  805
                3.94956E-06 0.0182

 cell  405
                1.18607E-07 0.1170


  ***** the nps-dependent tfc bin check results are suspect because there are only  1 nps tally
values to analyze *****
```

```
================================================================================================================================
==================================

          results of 10 statistical checks for the estimated answer for the tally fluctuation
chart (tfc) bin of tally      206


 tfc bin     --mean--      ---------relative error---------      ----variance of the variance----
--figure of merit--     -pdf-

 behavior    behavior      value   decrease   decrease rate      value   decrease   decrease rate
value     behavior     slope


 desired      random       <0.10      yes      1/sqrt(nps)       <0.10      yes        1/nps
constant    random      >3.00

 observed     random        0.01      yes          yes            0.00      yes         yes
constant    random       4.43

 passed?        yes          yes      yes          yes             yes      yes         yes
yes        yes         yes


================================================================================================================================
==================================
```

This line delineates a jump in code.

```
1tally      124        nps =    57520329

+                                  Photon Flux at the Sample one bin

           tally type 4    track length estimate of particle flux.      units   1/cm**2

           particle(s): photons

 number of histories used for normalizing tallies =     50000000.00


           volumes

                   cell:      815          825          835          845          855
865          885

                          2.81921E+00  2.81921E+00  2.81921E+00  2.81921E+00  2.81921E+00
2.81921E+00  2.81921E+00

                   cell:      895          805          405

                          2.81921E+00  2.81921E+00  2.81921E+00


 cell  815

                 3.12931E-03 0.0023


 cell  825
```

```
                3.11471E-03 0.0023


 cell  835

                3.11029E-03 0.0023


 cell  845

                3.15316E-03 0.0023


 cell  855

                3.08033E-03 0.0023


 cell  865

                1.12354E-03 0.0037


 cell  885

                1.13045E-03 0.0037


 cell  895

                7.75527E-04 0.0044


 cell  805

                1.14054E-03 0.0037


 cell  405

                3.00972E-04 0.0071



 ***** the nps-dependent tfc bin check results are suspect because there are only  1 nps tally
values to analyze *****



================================================================================================
==================================


          results of 10 statistical checks for the estimated answer for the tally fluctuation
chart (tfc) bin of tally      124
```

```
 tfc bin     --mean--      ---------relative error---------      ----variance of the variance----
--figure of merit--     -pdf-

 behavior    behavior      value   decrease   decrease rate      value   decrease   decrease rate
value     behavior     slope


 desired      random       <0.10      yes      1/sqrt(nps)       <0.10      yes        1/nps
constant    random      >3.00

 observed     random        0.00      yes          yes            0.00      yes         yes
constant    random       3.70

 passed?        yes          yes      yes          yes             yes      yes         yes
yes         yes          yes


================================================================================================
==================================
```

This line delineates a jump in code.

```
1tally      134        nps =    57520329

+                                  Photon Flux at the Sample Binned

           tally type 4    track length estimate of particle flux.      units   1/cm**2

           particle(s): photons

 number of histories used for normalizing tallies =     50000000.00


           volumes

                   cell:      815          825          835          845          855
865          885

                           2.81921E+00  2.81921E+00  2.81921E+00  2.81921E+00  2.81921E+00
2.81921E+00  2.81921E+00

                   cell:      895          805          405

                           2.81921E+00  2.81921E+00  2.81921E+00


 cell  815

      energy

    1.0000E-01   7.38211E-04 0.0048

    1.5000E-01   3.46619E-04 0.0068

    2.0000E-01   2.45062E-04 0.0080

    3.0000E-01   3.20057E-04 0.0069

    4.0000E-01   2.01023E-04 0.0090

    5.0000E-01   1.58453E-04 0.0093

    6.0000E-01   1.45358E-04 0.0097

    8.0000E-01   2.14216E-04 0.0078
```

```
   1.0000E+00   1.56173E-04 0.0090
   1.2500E+00   1.32623E-04 0.0103
   1.5000E+00   1.09941E-04 0.0113
   2.0000E+00   1.26961E-04 0.0103
   3.0000E+00   1.64696E-04 0.0089
   4.0000E+00   4.43940E-05 0.0177
   5.0000E+00   1.50961E-05 0.0309
   6.0000E+00   4.57018E-06 0.0537
   8.0000E+00   5.81005E-06 0.0434
   1.0000E+01   4.57614E-08 0.5542
     total      3.12931E-03 0.0023

cell  825
     energy
   1.0000E-01   7.33406E-04 0.0049
   1.5000E-01   3.48124E-04 0.0066
   2.0000E-01   2.44857E-04 0.0079
   3.0000E-01   3.28639E-04 0.0069
   4.0000E-01   1.97000E-04 0.0086
   5.0000E-01   1.58248E-04 0.0095
   6.0000E-01   1.42405E-04 0.0098
   8.0000E-01   2.13647E-04 0.0079
   1.0000E+00   1.54093E-04 0.0091
   1.2500E+00   1.28404E-04 0.0103
   1.5000E+00   1.06573E-04 0.0112
   2.0000E+00   1.27283E-04 0.0105
   3.0000E+00   1.61174E-04 0.0090
   4.0000E+00   4.44053E-05 0.0181
   5.0000E+00   1.59873E-05 0.0325
   6.0000E+00   4.76546E-06 0.0548
   8.0000E+00   5.66571E-06 0.0438
   1.0000E+01   2.95833E-08 0.5997
     total      3.11471E-03 0.0023

cell  835
     energy
```

```
   1.0000E-01   7.34731E-04 0.0048
   1.5000E-01   3.43140E-04 0.0066
   2.0000E-01   2.41362E-04 0.0082
   3.0000E-01   3.26473E-04 0.0067
   4.0000E-01   2.00459E-04 0.0087
   5.0000E-01   1.55595E-04 0.0095
   6.0000E-01   1.42833E-04 0.0098
   8.0000E-01   2.15529E-04 0.0081
   1.0000E+00   1.56864E-04 0.0092
   1.2500E+00   1.29262E-04 0.0105
   1.5000E+00   1.05278E-04 0.0112
   2.0000E+00   1.27791E-04 0.0104
   3.0000E+00   1.61576E-04 0.0091
   4.0000E+00   4.38412E-05 0.0184
   5.0000E+00   1.49506E-05 0.0299
   6.0000E+00   4.55641E-06 0.0575
   8.0000E+00   5.98378E-06 0.0423
   1.0000E+01   5.66751E-08 0.4690
     total      3.11028E-03 0.0023

cell  845
     energy
   1.0000E-01   7.46196E-04 0.0048
   1.5000E-01   3.54448E-04 0.0067
   2.0000E-01   2.41995E-04 0.0079
   3.0000E-01   3.22728E-04 0.0068
   4.0000E-01   2.05965E-04 0.0086
   5.0000E-01   1.57924E-04 0.0094
   6.0000E-01   1.44468E-04 0.0095
   8.0000E-01   2.15878E-04 0.0079
   1.0000E+00   1.57154E-04 0.0091
   1.2500E+00   1.32795E-04 0.0103
   1.5000E+00   1.11260E-04 0.0108
   2.0000E+00   1.27759E-04 0.0103
   3.0000E+00   1.65654E-04 0.0090
   4.0000E+00   4.31381E-05 0.0178
```

```
   5.0000E+00   1.57852E-05 0.0316
   6.0000E+00   4.43473E-06 0.0541
   8.0000E+00   5.54669E-06 0.0433
   1.0000E+01   3.67068E-08 0.4658
     total      3.15316E-03 0.0023

cell  855
     energy
   1.0000E-01   7.23815E-04 0.0048
   1.5000E-01   3.42900E-04 0.0067
   2.0000E-01   2.46515E-04 0.0082
   3.0000E-01   3.24701E-04 0.0069
   4.0000E-01   1.98191E-04 0.0087
   5.0000E-01   1.52593E-04 0.0095
   6.0000E-01   1.43463E-04 0.0097
   8.0000E-01   2.09757E-04 0.0078
   1.0000E+00   1.50049E-04 0.0092
   1.2500E+00   1.26526E-04 0.0104
   1.5000E+00   1.06668E-04 0.0112
   2.0000E+00   1.26293E-04 0.0105
   3.0000E+00   1.61719E-04 0.0090
   4.0000E+00   4.35113E-05 0.0184
   5.0000E+00   1.37880E-05 0.0307
   6.0000E+00   4.44021E-06 0.0533
   8.0000E+00   5.33414E-06 0.0427
   1.0000E+01   4.99678E-08 0.4424
     total      3.08031E-03 0.0023

cell  865
     energy
   1.0000E-01   3.64645E-04 0.0068
   1.5000E-01   1.47101E-04 0.0100
   2.0000E-01   8.63901E-05 0.0125
   3.0000E-01   1.07042E-04 0.0116
   4.0000E-01   6.29025E-05 0.0148
   5.0000E-01   4.51647E-05 0.0169
```

```
   6.0000E-01   3.84477E-05 0.0186
   8.0000E-01   5.24464E-05 0.0156
   1.0000E+00   3.68157E-05 0.0185
   1.2500E+00   3.12834E-05 0.0200
   1.5000E+00   2.67938E-05 0.0219
   2.0000E+00   3.47701E-05 0.0188
   3.0000E+00   6.99231E-05 0.0124
   4.0000E+00   1.16663E-05 0.0325
   5.0000E+00   4.41744E-06 0.0522
   6.0000E+00   1.29493E-06 0.0903
   8.0000E+00   2.42501E-06 0.0563
   1.0000E+01   1.17792E-08 1.0000
     total      1.12354E-03 0.0037

cell  885
     energy
   1.0000E-01   3.66183E-04 0.0067
   1.5000E-01   1.50098E-04 0.0100
   2.0000E-01   8.81349E-05 0.0129
   3.0000E-01   1.06382E-04 0.0117
   4.0000E-01   6.18894E-05 0.0150
   5.0000E-01   4.42717E-05 0.0188
   6.0000E-01   3.80988E-05 0.0186
   8.0000E-01   5.19353E-05 0.0148
   1.0000E+00   3.78046E-05 0.0176
   1.2500E+00   3.26194E-05 0.0202
   1.5000E+00   2.66408E-05 0.0218
   2.0000E+00   3.47115E-05 0.0187
   3.0000E+00   7.09890E-05 0.0125
   4.0000E+00   1.19568E-05 0.0336
   5.0000E+00   4.59968E-06 0.0535
   6.0000E+00   1.54670E-06 0.0913
   8.0000E+00   2.56974E-06 0.0644
   1.0000E+01   1.59495E-08 0.5821
     total      1.13045E-03 0.0037
```

cell 895

energy		
1.0000E-01	9.24127E-05	0.0137
1.5000E-01	1.04850E-04	0.0117
2.0000E-01	7.99206E-05	0.0141
3.0000E-01	1.03425E-04	0.0121
4.0000E-01	6.11940E-05	0.0148
5.0000E-01	4.29367E-05	0.0172
6.0000E-01	3.58842E-05	0.0184
8.0000E-01	5.29074E-05	0.0158
1.0000E+00	3.69057E-05	0.0184
1.2500E+00	3.09884E-05	0.0199
1.5000E+00	2.59946E-05	0.0225
2.0000E+00	3.19759E-05	0.0194
3.0000E+00	5.83072E-05	0.0141
4.0000E+00	1.11616E-05	0.0349
5.0000E+00	3.52889E-06	0.0587
6.0000E+00	1.20110E-06	0.1085
8.0000E+00	1.89977E-06	0.0671
1.0000E+01	2.74687E-08	0.7205
total	7.75521E-04	0.0044

cell 805

energy		
1.0000E-01	3.71820E-04	0.0066
1.5000E-01	1.52112E-04	0.0101
2.0000E-01	8.78259E-05	0.0128
3.0000E-01	1.09278E-04	0.0116
4.0000E-01	6.34265E-05	0.0145
5.0000E-01	4.66002E-05	0.0174
6.0000E-01	3.73578E-05	0.0183
8.0000E-01	5.19516E-05	0.0153
1.0000E+00	3.79032E-05	0.0184
1.2500E+00	3.26472E-05	0.0200
1.5000E+00	2.58842E-05	0.0215
2.0000E+00	3.47157E-05	0.0191

```
    3.0000E+00   6.88960E-05 0.0125
    4.0000E+00   1.17734E-05 0.0337
    5.0000E+00   4.30683E-06 0.0510
    6.0000E+00   1.52603E-06 0.0869
    8.0000E+00   2.45052E-06 0.0621
    1.0000E+01   6.88657E-08 0.4743
      total      1.14054E-03 0.0037

 cell  405
      energy
    1.0000E-01   1.24188E-04 0.0115
    1.5000E-01   4.08255E-05 0.0189
    2.0000E-01   2.24112E-05 0.0259
    3.0000E-01   2.53287E-05 0.0230
    4.0000E-01   1.39788E-05 0.0309
    5.0000E-01   9.46058E-06 0.0351
    6.0000E-01   8.00776E-06 0.0395
    8.0000E-01   1.12850E-05 0.0327
    1.0000E+00   7.47768E-06 0.0451
    1.2500E+00   6.65331E-06 0.0450
    1.5000E+00   5.54487E-06 0.0486
    2.0000E+00   7.47350E-06 0.0430
    3.0000E+00   1.38903E-05 0.0266
    4.0000E+00   2.60040E-06 0.0689
    5.0000E+00   9.36688E-07 0.1067
    6.0000E+00   3.69674E-07 0.2411
    8.0000E+00   5.39372E-07 0.1347
    1.0000E+01   3.31351E-10 1.0000
      total      3.00972E-04 0.0071


 ***** the nps-dependent tfc bin check results are suspect because there are only  1 nps tally
values to analyze *****
```

```
================================================================================================================
==================================

          results of 10 statistical checks for the estimated answer for the tally fluctuation
chart (tfc) bin of tally      134


 tfc bin     --mean--      ---------relative error---------      ----variance of the variance----
--figure of merit--     -pdf-

 behavior    behavior      value   decrease   decrease rate      value   decrease   decrease rate
value     behavior     slope


 desired      random       <0.10      yes      1/sqrt(nps)       <0.10      yes        1/nps
constant    random      >3.00

 observed     random        0.00      yes          yes            0.00      yes         yes
constant    random       3.70

 passed?        yes          yes      yes          yes             yes      yes         yes
yes        yes         yes


================================================================================================================
==================================
```

<u>This line delineates a jump in code.</u>

```
1tally      216        nps =    57520329

+                                  Photon Dose Rate at the Sample

          tally type 6    track length estimate of heating.           units   mev/gram

          particle(s): photons

 number of histories used for normalizing tallies =     50000000.00


          masses

                   cell:      815          825          835          845          855
865          885

                          2.21759E+00  2.21759E+00  2.21759E+00  2.21759E+00  2.21759E+00
2.21759E+00  2.21759E+00

                   cell:      895          805          405

                          2.21759E+00  2.21759E+00  2.21759E+00


 cell  815

                5.29919E-05 0.0032


 cell  825
```

```
                5.24831E-05 0.0032


 cell  835

                5.24678E-05 0.0032


 cell  845

                5.31842E-05 0.0032


 cell  855

                5.17608E-05 0.0032


 cell  865

                1.62309E-05 0.0054


 cell  885

                1.63989E-05 0.0055


 cell  895

                1.43498E-05 0.0059


 cell  805

                1.62937E-05 0.0054


 cell  405

                3.58121E-06 0.0113



 ***** the nps-dependent tfc bin check results are suspect because there are only  1 nps tally
values to analyze *****



================================================================================================
==================================


           results of 10 statistical checks for the estimated answer for the tally fluctuation
chart (tfc) bin of tally      216
```

tfc bin	--mean--	---------relative error---------			----variance of the variance----			--figure of merit--	-pdf-
behavior	behavior	value	decrease	decrease rate	value	decrease	decrease rate	value	behavior	slope
desired	random	<0.10	yes	1/sqrt(nps)	<0.10	yes	1/nps	constant	random	>3.00
observed	random	0.00	yes	yes	0.00	yes	yes	constant	random	10.00
passed?	yes	yes	yes	yes	yes	yes	yes	yes	yes	yes

Appendix C Additional Fission and Secondary Particle Flux and Dose Rate Comparison Data

This appendix includes all results comparing simulations tallying neutron and photon fluxes and dose rates. The aim is to confirm the influence of simulating fission particles alone vs with particles from secondary nuclear reactions. This section refers to all neutrons, photons, and electrons produced in nuclear reactions other than fission that are simulated in MCNP6.3.

Table 12 compares the neutron flux (separated into thermal, epithermal, and fast) and dose rate in the irradiation sites of interest between MCNP6.3 models that simulated fission particles and models that included fission and secondary particles in water samples. Results of the two simulations overlap. *N.B.* that simulations with fission and secondary particles included less neutron histories because of the burden of simulating secondary particles. As a result, the uncertainties are larger in the rightmost column of Table 12.

Table 12: MCNP6.3 neutron flux and dose rate results in water samples from simulations that consider secondary particles and models that do not.

Neutron Radiation Characteristic	Irradiation Site	Results Considering Fission Particles	Results Considering Fission and Secondary Particles
Thermal Flux (10^{11}·n·cm^{-2}·s^{-1})	**Inner Site # 4**	5.23 ± 0.01	5.25 ± 0.02
	Outer Site # 10	2.47 ± 0.01	2.47 ± 0.01
	Pool Site	0.0646 ± 0.0008	0.067 ± 0.002
Epithermal Flux (10^{11}·n·cm^{-2}·s^{-1})	**Inner Site # 4**	0.475 ± 0.002	0.475 ± 0.005
	Outer Site # 10	0.0753 ± 0.0007	0.075 ± 0.002
	Pool Site	0.00123 ± 0.00009	0.0011 ± 0.0002
Fast Flux (10^{11}·n·cm^{-2}·s^{-1})	**Inner Site # 4**	5.24 ± 0.01	5.26 ± 0.02
	Outer Site # 10	0.540 ± 0.002	0.540 ± 0.006
	Pool Site	0.0114 ± 0.0003	0.0105 ± 0.0009
Dose Rate (kGy·h^{-1})	**Inner Site # 4**	18.94 ± 0.03	18.90 ± 0.11
	Outer Site # 10	1.95 ± 0.01	1.92 ± 0.03
	Pool Site	0.065 ± 0.002	0.058 ± 0.007

The results in Table 12 conclude that secondary neutrons do not contribute significantly to the simulated neutron flux or dose rate in water samples.

Table 13 includes results of simulations similar to Table 12, but in methanol samples. The results and conclusion is the same; no effect of secondary particles on neutron tallies.

Table 13: MCNP6.3 neutron flux and dose rate results in methanol samples from simulations that consider secondary particles and models that do not.

Neutron Radiation Characteristic	Irradiation Site	Results Considering Fission Particles	Results Considering Fission and Secondary Particles
Thermal Flux ($\cdot 10^{11} \cdot n \cdot cm^{-2} \cdot s^{-1}$)	**Inner Site # 4**	5.26 ± 0.01	5.25 ± 0.02
	Outer Site # 10	2.47 ± 0.01	2.45 ± 0.01
	Pool Site	0.066 ± 0.001	0.065 ± 0.002
Epithermal Flux ($\cdot 10^{11} \cdot n \cdot cm^{-2} \cdot s^{-1}$)	**Inner Site # 4**	0.469 ± 0.002	0.471 ± 0.005
	Outer Site # 10	0.0727 ± 0.0006	0.075 ± 0.002
	Pool Site	0.00097 ± 0.00008	0.0010 ± 0.0002
Fast Flux ($\cdot 10^{11} \cdot n \cdot cm^{-2} \cdot s^{-1}$)	**Inner Site # 4**	5.22 ± 0.01	5.21 ± 0.02
	Outer Site # 10	0.537 ± 0.002	0.541 ± 0.006
	Pool Site	0.0104± 0.0003	0.0102 ± 0.0008
Dose Rate ($kGy \cdot h^{-1}$)	**Inner Site # 4**	21.22 ± 0.04	21.2 ± 0.01
	Outer Site # 10	2.16 ± 0.01	2.17 ± 0.04
	Pool Site	0.071 ± 0.002	0.067 ± 0.007

Simulations also investigated the effect of secondary particles on photon tallies for flux and dose rates. The results found in Figure 23 confirm that there is a large influence of secondary particles on both the gamma flux and dose rate. Simulating radiation from secondary particles increases the reported photon flux and dose rate at inner site # 4 by > 250 %, and at outer site # 10 and the pool site by > 200 %. Thus, MCNP6.3 simulations must consider secondary particles in water samples, regardless of the lack of neutron impact.

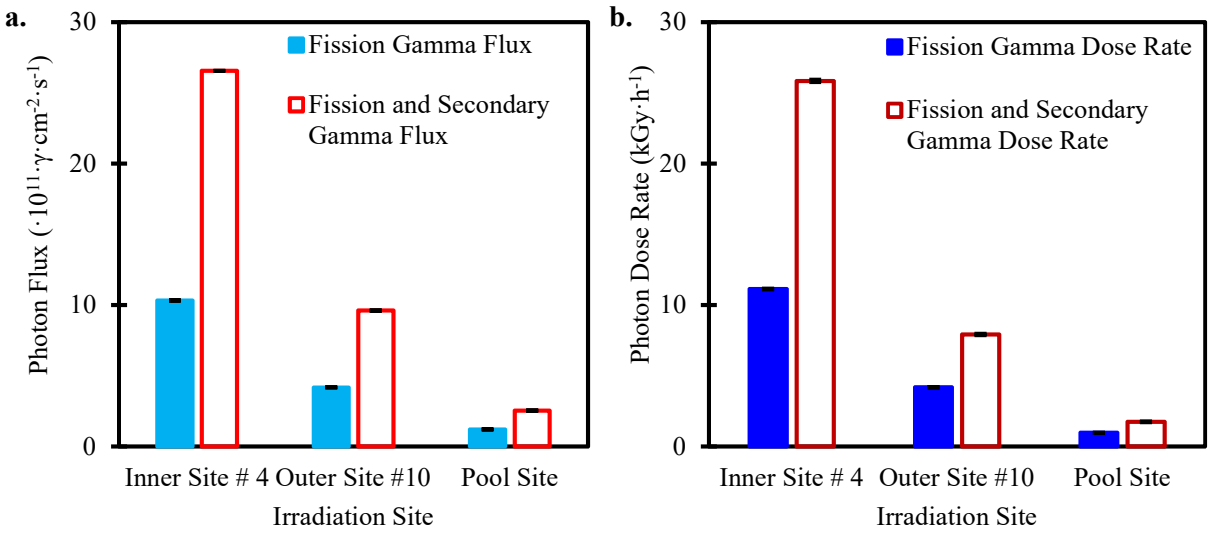

Figure 23: MCNP6.3 simulated photon fluxes (a.) and dose rates (b). Simulation results from models only considering fission photons (blue), and models simulating fission and secondary photons (red). Flux errors are between ± $1.68 \cdot 10^{8}$ and ± $13.28 \cdot 10^{8}$ $\gamma \cdot cm^{-2} \cdot s^{-1}$, while dose rate errors are between ± 0.003 and ± 0.013 $kGy \cdot h^{-1}$.

Figure 24 includes the results of simulations similar to those from Figure 23, but in methanol samples. The conclusion is the same: when simulating photons, secondary particles must be considered.

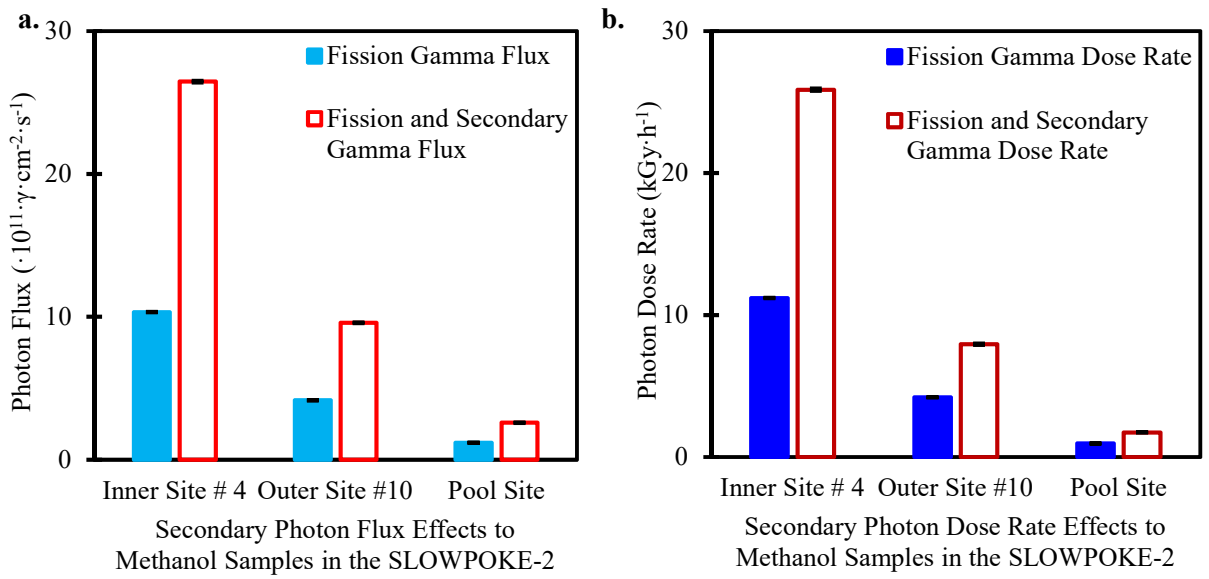

Figure 24: The effects of simulating fission and secondary photons in methanol on photon fluxes (a.) and dose rate (b) results. Models only simulating fission photons are in blue, and models simulating fission and secondary photons are in red. Flux errors are between ± 4.76·10^8 and ± 60.86·10^8 γ·cm^-2·s^-1, while dose rate errors are between ± 0.005 and ± 0.083 kGy·h^-1.

Table 14 lists the dose rates from neutrons and photons from simulations considering fission and secondary particles, which are applied throughout this thesis. Simulated dose rates for electrons are also applied, but are from simulations that do not consider secondary particles as it was not computationally reasonable to simulated electrons and secondary particles in the same models.

Table 14: MCNP6.3 simulated dose rates from models considering fission particles and those considering fission and secondary particles compiled for g-value calculations.

Sample Solvent	Radiation Dose	SLOWPOKE-2 Irradiation Site	Simulated Dose Rate ($kGy \cdot h^{-1}$) (This Work)
Water	Photon	Site # 4	25.84 ± 0.08
		Site # 10	7.92 ± 0.04
		Pool Site	1.74 ± 0.02
	Neutrons	Site # 4	18.9 ± 0.1
		Site # 10	1.92 ± 0.03
		Pool Site	0.058 ± 0.007
	Electrons	Site # 4	11.09 ± 0.09*
		Site # 10	4.23 ± 0.06*
		Pool Site	0.95 ± 0.02*
	Total	Site # 4	55.8 ± 0.3
		Site # 10	14.1 ± 0.1
		Pool Site	2.75 ± 0.05
Methanol	Photon	Site # 4	25.87 ± 0.08
		Site # 10	7.95 ± 0.04
		Pool Site	1.74 ± 0.02
	Neutrons	Site # 4	21.2 ± 0.1
		Site # 10	2.17 ± 0.04
		Pool Site	0.067 ± 0.007
	Electrons	Site # 4	10.8 ± 0.6*
		Site # 10	4.3 ± 0.4*
		Pool Site	1.2 ± 0.2*
	Total	Site # 4	57.9 ± 0.3
		Site # 10	14.4 ± 0.5
		Pool Site	3.0 ± 0.2

* Values simulated only considering fission particles. It was not feasible in this thesis to simulate secondary particles in NPE mode due to the computational power required.

Appendix D Irradiated PFOA Dataset

Table 15 shows the concentration of PFCAs in control samples. Table 16, Table 17, andTable 18 detail the UHPLC-MS/MS results of all irradiated PFOA samples. The detection limits are as follows:

- PFOA – 0.096 μg · kg
- PFHpA – 0.13 μg · kg
- PFHxA – 0.13 μg · kg

Table 15: Control Sample PFCA Measurements

Control Name	[PFHxA]	[PFHpA]	[PFOA]
C1	*	*	95.10
C2	0.00	0.14	116.39
C3	0.00	0.16	121.13
C4	0.00	0.15	119.34
C5	0.00	0.16	121.49
C21	0.00	0.13	117.96
C22	0.00	0.13	113.11
C23	0.00	0.11	116.71
C24	0.00	0.13	114.05
C25	0.00	0.12	112.28
C31	0.00	0.12	109.81
C32	0.00	0.12	113.22
C33	0.00	0.14	108.89
C34	0.00	0.14	108.35
C35	0.00	0.12	109.09
C41	0.00	0.14	109.82
C42	0.00	0.10	112.22
C43	0.00	0.13	110.53

* These samples were only investigated for PFOA, not shorter chain PFCAs.

Table 16: PFCA irradiation results of samples irradiated at site #4

Sample Name	Site of Irradiation	Irradiation Duration (minutes)	[PFHxA]	[PFHpA]	[PFOA]
4-1-1	Inner Site #4	1	*	*	100.63
4-1-2		1	0.00	0.14	109.83
4-1-3		1	0.00	0.12	109.62
4-2-1		2	*	*	98.91
4-2-2		2	0.00	0.17	109.76
4-2-3		2	0.00	0.15	110.03
4-5-1		5	*	*	87.85
4-5-2		5	0.00	0.28	112.84
4-5-3		5	0.14	0.26	117.42
4-10-1		10	*	*	88.32
4-10-2		10	0.00	0.34	108.83
4-10-3		10	0.14	0.41	109.93
4-10-4		10	0.09	0.34	107.81
4-10-5		10	0.00	0.37	112.82
4-20-1		20	*	*	91.97
4-20-2		20	0.00	0.52	107.59
4-20-3		20	0.00	0.47	100.94
4-60-1		60	0.23	0.99	102.58
4-60-2		60	0.26	1.13	105.78
4-60-3		60	0.28	0.99	107.42
4-80-1		80	0.18	1.14	93.70
4-80-2		80	0.15	1.16	95.15
4-80-3		80	0.26	1.11	91.59
4-120-1		120	*	*	82.28
4-120-2		120	0.35	1.72	102.72
4-120-3		120	0.33	1.69	102.71

* These samples were only investigated for PFOA, not shorter chain PFCAs.

Table 17: PFCA irradiation results of samples irradiated at site #10

Sample Name	Site of Irradiation	Irradiation Duration (minutes)	[PFHxA]	[PFHpA]	[PFOA]
10-5.1-1	Outer Irradiation Site #10	5.1	0.17	0.47	98.97
10-5.1-2		5.1	0.19	0.61	107.31
10-5.1-3		5.1	0.20	0.67	97.34
10-10.2-1		10.2	0.00	0.20	109.51
10-10.2-2		10.2	0.00	0.24	110.18
10-10.2-3		10.2	0.00	0.24	108.81
10-25-1		25	0.00	0.32	105.23
10-25-2		25	0.15	0.44	109.40
10-25-3		25	0.18	0.41	110.69
10-51-1		51	0.00	0.21	109.63
10-51-2		51	0.00	0.25	106.41
10-51-3		51	0.14	0.24	105.12
10-102-1		102	0.19	0.53	99.10
10-102-2		102	0.20	0.54	110.60
10-102-3		102	0.18	0.61	97.42
10-5:7-1		307	0.13	0.20	83.61
10-5:7-2		307	0.13	0.21	113.87
10-5:7-3		307	0.18	1.13	95.57
10-409-1		409	0.00	0.69	100.48
10-409-2		409	0.00	0.53	98.63

Table 18: PFCA irradiation results of samples irradiated at the pool site

Sample Name	Site of Irradiation	Irradiation Duration (minutes)	[PFHxA]	[PFHpA]	[PFOA]
P-31-1	Pool Irradiation Site	31	0.00	0.19	102.55
P-31-2		31	0.00	0.18	99.46
P-31-3		31	0.00	0.18	101.55
P-31-4		31	0.00	0.19	103.99
P-31-5		31	0.00	0.20	109.73
P-62.8-1		62.8	0.00	0.23	103.07
P-62.8-2		62.8	0.00	0.21	99.51
P-62.8-3		62.8	0.00	0.24	101.68
P-62.8-4		62.8	0.00	0.22	103.34
P-62.8-5		62.8	0.00	0.20	103.55
P-2.6-1		157	0.15	0.34	112.32
P-2.6-2		157	0.17	0.41	115.70
P-2.6-3		157	0.14	0.35	105.77
P-5.2-1		314	0.14	0.23	107.81
P-5.2-2		314	0.15	0.28	109.77
P-5.2-3		314	0.13	0.27	105.53
P-471-1		471	0.00	0.49	105.64
P-471-2		471	0.00	0.56	108.78
P-471-3		471	0.09	0.58	108.68
P-471-4		471	0.00	0.60	109.49